Tampere University

JANNE SOLANPÄÄ

Optimization of Ultrafast Strong-Field Phenomena

Tampere University Dissertations 82

Tampere University Dissertations 82

JANNE SOLANPÄÄ

Optimization of Ultrafast Strong-Field Phenomena

ACADEMIC DISSERTATION
To be presented, with the permission of
the Faculty of Engineering and Natural Sciences
of Tampere University,
for public discussion in the auditorium S2 of the Sähkötalo building,
Korkeakoulunkatu 3, 33720, Tampere,
on June 25th 2019, at 12 o'clock.

ACADEMIC DISSERTATION
Tampere University, Faculty of Engineering and Natural Sciences
Finland

Responsible supervisor and Custos
Professor
Esa Räsänen
Tampere University
Finland

Pre-examiners
Professor
Jan Marcus Dahlström
Lund University
Sweden

Academy Research Fellow
Matti Silveri
University of Oulu
Finland

Opponent
Professor
Niels Engholm Henriksen
Technical University of Denmark
Denmark

The originality of this thesis has been checked using the Turnitin OriginalityCheck service.

Cover design: Roihu Inc.

ISBN 978-952-03-1140-7 (print)
ISBN 978-952-03-1141-4 (pdf)
ISSN 2489-9860 (print)
ISSN 2490-0028 (pdf)
http://urn.fi/URN:ISBN:978-952-03-1141-4

PunaMusta Oy – Yliopistopaino
Tampere 2019

Abstract

Attosecond science deals with monitoring and control of electron dynamics in their native, attosecond time scale. Ultrafast electron dynamics is the driving force behind chemical reactions, it determines the optical response of matter, and it is the cornerstone of multiple ultrafast nanoscale imaging techniques.

Attosecond phenomena are often driven by strong-field light-matter interaction. Femtosecond laser pulses with electric fields rivaling those of atomic binding forces drive complex nonlinear phenomena in atoms, molecules, and solid state. They include electron excitations, nonlinear frequency up-conversion known as high-order harmonic generation (HHG), and emission of ultra-energetic electrons via above-threshold ionization (ATI). These processes have important roles in ultrafast technologies. For example, HHG is used as a source for coherent X-ray pulses with durations down to attoseconds, ATI is used for building electron wave packets for self-interrogation spectroscopy of matter, and excited Rydberg-states of atoms are prime candidates for multi-qubit quantum computing.

Control of strong-field attosecond phenomena can be achieved by shaping the temporal profile of the driving femtosecond pulse in modern light-field synthesizers. This dissertation is a computational expedition to shaping the driving laser pulses for *optimizing* strong-field light-matter interaction in HHG, ATI, and Rydberg-state preparation in atoms.

We begin this dissertation with a brief review of relevant strong-field attosecond phenomena with an emphasis on their theoretical modeling. We continue with an overview of control and optimization of these phenomena both from an experimental and a computational point of view. Later, we describe in detail the computational models we have used. The corresponding software is provided in the online supplementary material.

Our optimization studies deliver experimentally feasible optimization/control schemes for shaping the driving femtosecond laser pulses to increase the maximum energy and signal strength of HHG and ATI in atomic gases.

We also demonstrate how the optimized processes behind the optimized HHG and ATI can be understood with a semiclassical three-step model. The excitation of alkali metals to their Rydberg states is shown to be feasible with multicolor femtosecond fields, decreasing the excitation time by several orders of magnitude compared to traditional methods. On the downside, in its current form the proposed scheme lacks the finesse to populate only a single final state.

We also develop a new finite element simulation suite for studying attosecond phenomena in nanostructures. Nanostructures shape the spatial profile of the driving laser field, something existing simulation software cannot easily model. Our software suite is designed for simulating these systems efficiently, and it can incorporate the spatial inhomogeneity of the driving field with ease.

We close this dissertation with a summary of our optimization studies and obtained results. They are discussed in the context of other recent work in the field, and we also reflect on possible improvements and directions for future work.

Tiivistelmä

Elektronien liikkeen havainnointi ja ohjaaminen on attosekuntitieteen keskiössä. Attosekuntiluokan elektroniprosessit ovat esimerkiksi kemiallisten reaktioiden takana, selittävät aineen optiset ominaisuudet sekä ovat pohjana useille ultranopeille nanomittaluokan kuvantamismenetelmille.

Useat mielenkiintoiset attosekuntiluokan ilmiöt aiheutuvat vahvasta ulkoisesta sähkömagneettisesta kentästä. Tällaisia kenttiä saadaan femtosekuntilasersykäyksillä, joiden kenttien vahvuus on samaa suuruusluokkaa kuin atomin elektroniinsa kohdistama sähkökenttä. Voimakas sähkömagneettinen vuorovaikutus aiheuttaa atomien, molekyylien ja kiinteän aineen epälineaarisia ilmiöitä kuten korkeaenergisten fotonien tuottoa (HHG), nopeiden elektronien emissiota sekä esimerkiksi atomielektronin virittymistä korkeille sidotuille tiloille.

Edellämainitut ilmiöt ovat myös pohjana useille teknisille edistyksille: HHG:lla tuotetaan koherentteja röntgensykäyksiä, joiden kesto on vain muutamien attosekuntien suuruusluokkaa; nopeita fotoemittoituneita elektroniaaltopaketteja käytetään aineen kuvantamiseen; ja Rydberg-tiloille viritettyjä atomeita käytetään kvanttilaskennassa kubitteina.

Attosekuntiluokan ilmiöitä voidaan ohjata haluttuun suuntaan käyttämällä femtosekuntilasersykäyksiä, joiden sähkökentän aikariippuvuutta voidaan säätää. Tämä väitöskirja on laskennallinen tutkimusretki, jolla pyritään löytämään menetelmiä ennustamaan sellaisten femtosekuntilasersykäysten aikaprofiileja, joilla aiemmin mainittuja ilmiöitä – HHG:ta, elektroniemissiota sekä Rydbergtilojen virityksiä – voidaan tehostaa, *optimoida*.

Väitöskirjan alussa esitellään työn kannalta oleelliset vahvojen kenttien attosekuntiluokan ilmiöt keskittyen etenkin niiden teoreettisiin ja laskennallisiin malleihin. Tutkielmassa annetaan myös yleiskatsaus femtosekuntisykäysten käytöstä atomifysiikan ilmiöiden ohjaamisessa ja optimoinnissa avaten sekä alan kokeellista että laskennallista puolta. Tutkimuksessamme käytetyt laskennalliset mallit käydään yksityiskohtaisesti läpi, ja väitöskirjan oheismateriaali

(saatavilla internetistä) sisältää oleellisimmat työssä käytetyt ohjelmistot ja analyysityökalut.

Tutkimusten tuloksina on löydetty menetelmiä femtosekuntilasersykäysten suunnittelua varten. Näillä menetelmillä saadaan kasvatettua sekä HHG:n että korkeaenergisen elektroniemission hyötysuhdetta ja maksimienergiaa. Työssä tutkittiin myös femtosekuntilasersykäysten käyttöä alkalimetalliatomien virittämiseksi kvanttilaskentaa varten. Optimointimenetelmämme ja femtosekuntilasersykäysten käyttö vähentää viritykseen käytettävää aikaa huomattavasti perinteisiin tekniikoihin verrattuina, mutta nykyisessä muodossaan menetelmä ei ole tarpeeksi tarkka, jotta sillä voitaisiin miehittää vain yksi tietty tila.

Väitöskirjassa kehitetään myös uusi elementtimenetelmään pohjautuva laskentaohjelmisto, joka on suunniteltu nanorakenteiden attosekunti-ilmiöiden mallinnukseen. Nanorakenteet muuttavat niihin kohdistetun femtosekuntilasersykäyksen paikkariippuvuutta, mitä useimmat aiemmat mallinnusohjelmistot eivät kykene huomioimaan. Kehittämämme ohjelmisto mallintaa näitä tilanteita tehokkaasti ja ottaa huomioon femtosekuntilasersykäysten epähomogeenisen paikkariippuvuuden.

Väitöskirjan lopussa on yhteenveto löydöksistämme, joita käsitellään suhteessa muihin alan tuoreisiin tutkimuksiin. Pohdimme myös mahdollisia kehityskohteita sekä suuntaa tuleville tutkimuksille.

Preface

I am grateful to Esa for his support, insights, and discussions during my training. He is a tremendous mentor who has supplied me with an educating environment, and the freedom to select my projects and hone the skill set of my choosing. Esa keeps providing me opportunities to develop both myself and things around me, and for that I am eternally grateful.

Likewise, I have had the joy of working with some other amazing researchers in our field. Special thanks go to my friends and colleagues P. J. J. Luukko, I. Kylänpää, J. Keski-Rahkonen, M. Molkkari, A. Odriazola-Diaz, N. I. Shvetsov-Shilovski, and J. Tiihonen. In addition, I would like to extend my gratitude to my friends N. Solanpää, P. Elonen, and L. Elonen for their unwavering interest in what I do.

I gracefully acknowledge the financial support from multiple organizations including the Academy of Finland, Alfred Kordelin foundation, Condenced Matter and Material Physics network, Cost Action CM1204 XLIC, Cronos EU-FP7 network, CSC – IT Center for Science Ltd., Norden Nanocontrol network, and NordForsk.

Finally, I would like to thank Siiri for her love, support, and patience.

Janne

Contents

List of Publications

This dissertation is based on the following publications

I J. Solanpää, J. A. Budagosky, N. I. Shvetsov-Shilovski, A. Castro, A. Rubio, and E. Räsänen, *Optimal control of high-harmonic generation by intense few-cycle pulses*, Phys. Rev. A **90**, 053402 (2014).

II J. Solanpää, M. F. Ciappina, and E. Räsänen, *Optimal control of photoelectron emission by realistic waveforms*, J. Mod. Opt. **64**, 1784 (2017).

III J. Solanpää and E. Räsänen, *Control of Rydberg-state population with realistic femtosecond laser pulses*, Phys. Rev. A **98**, 053422 (2018).

IV J. Solanpää and E. Räsänen, `Fiend` – *Finite Element Quantum Dynamics*, arXiv, 1812.05943 (2019).

Summary of J. Solanpää's contributions in these publications:

Paper I J. Solanpää, together with J. A. Budagosky and N. I. Shvetsov-Shilovski, performed the numerical experiments, analyzed the data, and wrote the first draft of the paper. The numerical experiments were interpreted by all authors, and all authors contributed to writing of the final manuscript.

Paper II J. Solanpää wrote the simulation software, performed the numerical experiments, analyzed the data, and wrote majority of the first draft of the article. All authors contributed to interpretation of the numerical experiments and writing of the final manuscript.

Paper III J. Solanpää developed the optimization setup, performed the numerical experiments, analyzed the data, and wrote the first draft of the paper. Both authors contributed to interpretation of the numerical experiments and writing of the final manuscript.

Paper IV J. Solanpää derived the numerical methods, developed the simulation software, and wrote the first draft of the paper. Both authors contributed to writing of the final manuscript.

List of Abbreviations

1D	one-dimensional
2D	two-dimensional
3D	three-dimensional
a.u.	Hartree atomic units
ADK	Ammosov-Delone-Krainov
AFC	adaptive feedback control
ATI	above-threshold ionization
BC	boundary condition
BFGS	Broyden-Fletcher-Goldfarb-Shannon
BOBYQA	Bound Optimization BY Quadratic Approximation
CEP	carrier-envelope phase
CN	Crank-Nicolson
COBYLA	Constrained Optimization BY Linear Approximation
CW	continuous wave
EM	electromagnetic
FD	finite difference
FE	finite element
FEM	finite element method
FWHM	full width at half maximum
HH	high-order harmonic

HHG	high-order harmonic generation
IR	infrared
KFR	Keldysh-Faisal-Reiss
LG	length gauge
LIED	laser-induced electron diffraction
MCMC	Markov chain Monte Carlo
MLSL	Multi-Level Single Linkage
NEWUOA	NEW Unconstrained Optimization with quadratic Approximation
NIR	near-infrared
ODE	ordinary differential equation
OPCPA	optical parametric chirped-pulse amplification
PDE	partial differential equation
PES	photo-electron spectrum
PPT	Perelomov-Popov-Terent'ev
QM	quantum mechanical
QOCT	quantum optimal control theory
RK	Runge-Kutta
SAE	single active electron
SFA	strong-field approximation
TD	time-dependent
TDDFT	time-dependent density functional theory
TDSE	time-dependent Schrödinger equation
TISE	time-independent Schrödinger equation
tSurff	time-dependent surface flux -method
UV	ultraviolet

VG	velocity gauge
VIS	visible
XFEL	X-ray free electron laser
XUV	extreme ultraviolet
ZDBC	zero Dirichlet boundary condition

1 Introduction

1.1 Attosecond science and control of electron dynamics

Femtochemistry, i.e., photography and control of matter in the femtosecond time scale [1], has enabled us to track *nuclear* trajectories in multiple processes including, e.g., chemical reactions [1–3] – especially with biomolecules [1, 3] – and structural transitions in solid-state physics [1, 3, 4]. Since the early 21st century, we have progressed further into the era of *attosecond science* enabling us to monitor and control the *electron* dynamics in the attosecond time scale [5]. The emergence of attosecond science is providing us not only deeper insight into fundamental questions in quantum mechanics [6–11] but also technological advances with applications in, e.g., condensed matter physics [12, 13], chemistry [13–21], and molecular biology [16–21].

Attosecond science is founded on ultrashort intense laser pulses with durations of a few femtoseconds [22]. Such electromagnetic (EM) fields induce highly nonlinear phenomena in matter, and the consequent dynamics occur in the attosecond time scale. Notable examples include the ejection of ultraenergetic electrons via above-threshold ionization (ATI) in atoms [23–26], the generation of coherent X-ray pulses with durations down to a few dozen attoseconds via high-order harmonic generation (HHG) [27–42], and atomic/molecular self-interrogation with their own electron(s) in high-order harmonic (HH) spectroscopy [14, 43–54], laser-induced electron diffraction (LIED) [55–63], and ultrafast photoelectron holography [64–71]. In addition, access to electron dynamics in the attosecond time scale allows us to *control* electron dynamics during chemical reactions, paving the way for attochemistry [67, 72–80].

The control of electron dynamics relies on bespoke femtosecond laser pulses [81–84]. Sub-femtosecond tailoring of laser electric fields is available with modern waveform synthesizers [83–85], allowing the steering of the electron motion by shaping the driving laser field. This allows us to control and *optimize*, e.g.,

chemical reactions such as bond-breaking [86–89] and bond-formation [89–91], table-top HH attosecond pulse generators [92–120], and ultrafast nanoscale electron microscopes [121–125].

Ultrafast control of quantum phenomena is also in the core of quantum computing technologies [126]. Multi-qubit setups can already be realized in numerous systems including, e.g., atomic lattices [127–129]. There the atoms are localized in a regular array using laser tweezers [129, 130], and the inter-atom interactions can be switched on by exciting the atoms to their high-energy *Rydberg states* [128]. Recently, Rydberg-atom arrays have been demonstrated with more than 50 qubits [131, 132].

1.2 Research objectives and scope of the thesis

While attosecond science has come a long way from its infancy, there are still challenges relating to, e.g., the generation of attosecond laser pulses [74], photoelectron yields and energies relating to applications in attosecond spectroscopy [59], and precise and ultrafast initialization of atomic qubits in their Rydberg states for quantum computing [133]. In addition, while laser-matter interaction in atoms, molecules, and solid state can be numerically simulated with numerous publicly available software packages [134–142], they are not well suited for modeling attosecond science in nanodevices.

We address the above issues in this thesis. Specifically, the objectives are

1. to provide schemes for finding *experimentally feasible* control mechanisms of laser-matter interaction in HHG, ATI, and ultrafast Rydberg-excitations, and

2. to develop an efficient and versatile toolset for modeling and analysis of strong-field phenomena not only in atoms but also in nanodevices.

Objective 1 is addressed in **Paper I** for HHG, **Paper II** for ATI, and **Paper III** for the ultrafast Rydberg-excitation. In these works we report our quantum control simulations to *optimize* these processes with driving fields compatible with modern waveform synthesis. Objective 2 is addressed especially in **Paper IV**, where we describe a software suite developed for the simulation of ultrafast

strong-field phenomena in nanodevices. Objective 2 is also addressed by collecting polished versions of the software and analysis tools developed for the control studies in **Papers I** – **III** to the online supplementary of this thesis in Ref. [143].

1.3 Organization of the thesis

The thesis is organized as follows. In Ch. 2 we discuss the laser-induced strong-field phenomena relevant to this thesis and introduce the theoretical framework used for modeling them. Next, in Ch. 3, we review the field of quantum control with our focus on (i) the control of laser-induced strong-field phenomena in atomic gases and on (ii) the experimental generation of laser pulses for control. Numerical methods for solving the semiclassical and quantum mechanical (QM) models are reviewed in Ch. 4, complemented by a concise description of the optimization algorithms used in this work. Our most important findings are discussed in Ch. 5, and we conclude this compendium in Ch. 6 with a brief summary and an outlook on future directions. Note that detailed descriptions of the findings of this thesis can be found in the research papers **I** – **IV** appended at the end of this thesis.

2 Ultrafast strong-field physics

2.1 Atoms in ultrafast laser fields

This thesis revolves around modeling electrons in a gas of atoms interacting with strong and coherent electromagnetic (EM) pulses, *laser pulses*, which have durations less than a few dozen femtoseconds. In a typical experiment, a gas jet flows through the focus area of the EM pulse [144], and the atomic electrons interact with the laser field producing a multitude of different phenomena depending on the atomic species and characteristics of the driving field. With high-repetition femtosecond pulse sources [85], the gas jet is repeatedly exposed to an ultrashort laser field, and even rare events can be measured. Typical measurements capture, e.g., the terminal kinetic energy of ionized electrons, total ejected electron count, and the EM radiation emitted by the gas [22].

While there is a large number of atoms simultaneously interacting with the driving laser field, they are practically independent of each other due to low gas density of a typical experiment [23]. This is especially true for photoionized electrons, but also for the emitted EM fields – provided that the experimental setup is carefully designed [145].

Our numerical experiments in this compendium follow this well-traveled road: we pick a single representative atom from the gas jet and investigate the response of its electron(s) to the driving laser pulse. In the following, we will briefly go through the elementary quantum mechanics needed for a typical single-atom treatment, discuss some of the most notable phenomena in ultrafast strong-field physics, and finally, introduce a standard semiclassical model used in strong-field physics.

Unless otherwise specified, we use Hartree atomic units (a.u.) throughout this thesis, i.e., the electron rest mass, elementary charge, reduced Planck's constant, and the Coulomb constant are set to unity: $m_e = q_e = \hbar = (4\pi\epsilon_0)^{-1} = 1$ [146].

2.2 Quantum description of light-matter interaction

Electron dynamics of an atomic electron in an external EM field is described by the time-dependent Schrödinger equation (TDSE) [27]

$$\mathrm{i}\partial_t \left|\psi(t)\right\rangle = \hat{H}(t)\left|\psi(t)\right\rangle, \tag{2.1}$$

where $\left|\psi(t)\right\rangle$ is the time-dependent state of the electron and $\hat{H}(t)$ the time-dependent Hamiltonian operator.

The light-matter interaction is incorporated by the minimal coupling Hamiltonian

$$\hat{H}(t) = \frac{[\hat{\mathbf{p}} + \mathbf{A}(\hat{\mathbf{r}}, t)]^2}{2} + V_{\text{atom}}(\hat{\mathbf{r}}), \tag{2.2}$$

where $\hat{\mathbf{p}}$ is the momentum operator, $\mathbf{A}(\hat{\mathbf{r}},\ t)$ is the time- and position-dependent vector potential of the external EM field[1], $\hat{\mathbf{r}}$ is the position operator, and $V_{\text{atom}}(\hat{\mathbf{r}})$ is the atomic potential (operator) [147].

While the above presentation of TDSE is indeed the full description of an atomic electron interacting with, e.g., laser pulses, it turns out to be quite tedious for numerical and theoretical treatments due to the uncoupled position- and time-dependence of the vector potential. In the following subsection, we will introduce the *dipole approximation* where we can get rid of this complexity yielding a more suitable approximation for strong-field physics.

With this in mind, we first write out Eq. (2.2) as

$$\hat{H}(t) = \frac{\hat{\mathbf{p}}^2}{2} + \frac{1}{2}\hat{\mathbf{p}} \cdot \mathbf{A}(\hat{\mathbf{r}}, t) + \frac{1}{2}\mathbf{A}(\hat{\mathbf{r}}, t) \cdot \hat{\mathbf{p}} + \frac{\mathbf{A}(\hat{\mathbf{r}}, t)^2}{2} + V_{\text{atom}}(\hat{\mathbf{r}}),$$

and simplify it even further by working in the Coulomb gauge [27], where

[1] Note that we absorb the prefactor $1/c$, i.e., inverse of the speed of light, into $\mathbf{A}$.

$\hat{\mathbf{p}} \cdot \mathbf{A}(\hat{\mathbf{r}}, t) \equiv \mathbf{A}(\hat{\mathbf{r}}, t) \cdot \hat{\mathbf{p}}$.[2] This yields the Hamiltonian operator

$$\hat{H}(t) = \frac{\hat{\mathbf{p}}^2}{2} + V_{\text{atom}}(\hat{\mathbf{r}}) + \mathbf{A}(\hat{\mathbf{r}}, t) \cdot \hat{\mathbf{p}} + \frac{\mathbf{A}(\hat{\mathbf{r}}, t)^2}{2}. \tag{2.3}$$

2.2.1 Dipole approximation

When the wavelength of the external EM field is much larger than the typical excursion length of the atomic electron during the interaction (up to a few dozen nanometers in our studies, see, e.g., Ch. 5.2) we can neglect the spatial variations of the EM field around the atom: $\mathbf{A}(\mathbf{r}, t) \approx \mathbf{A}(\mathbf{r}_{\text{atom}}, t) \doteq \mathbf{A}(t)$. It is worth noting the this also sets the magnetic field to zero according to the Maxwell's equations [148], thus preventing the applicability of the approximation for extremely intense fields [149] for which a non-dipole [149–159] or even a relativistic formulation [160–164] is required.

The *dipole approximation* gives us the Hamiltonian operator [27]

$$\hat{H}(t) = \frac{\hat{\mathbf{p}}^2}{2} + V_{\text{atom}}(\hat{\mathbf{r}}) + \mathbf{A}(t) \cdot \hat{\mathbf{p}} + \frac{\mathbf{A}(t)^2}{2},$$

where the last term vanishes with the gauge transformation [27]:

$$\begin{aligned}
\mathbf{A}(t) &\to \mathbf{A}_{\text{VG}}(t) &&= \mathbf{A}(t); \\
\left|\psi(t)\right\rangle &\to \left|\psi_{\text{VG}}(t)\right\rangle &&= e^{\frac{\mathrm{i}}{2}\int_{-\infty}^{t} A(\tau)^2 \,\mathrm{d}\tau} \left|\psi(t)\right\rangle; \\
V(\hat{\mathbf{r}}, t) &\to V_{\text{VG}}(\hat{\mathbf{r}}, t) &&= V_{\text{atom}}(\hat{\mathbf{r}}) - \frac{1}{2}\mathbf{A}(t)^2,
\end{aligned}$$

leaving us with the Hamiltonian operator

$$\hat{H}_{\text{VG}}(t) = \frac{\hat{\mathbf{p}}^2}{2} + V_{\text{atom}}(\hat{\mathbf{r}}) + \mathbf{A}(t) \cdot \hat{\mathbf{p}}. \tag{2.4}$$

[2] $$\begin{aligned}
\langle \mathbf{r}| \hat{\mathbf{p}} \cdot \mathbf{A}(\hat{\mathbf{r}}, t) \left|\psi\right\rangle &= \int \mathrm{d}\mathbf{r}' \, \langle \mathbf{r}|\hat{\mathbf{p}}|\mathbf{r}'\rangle \cdot \langle \mathbf{r}'|\mathbf{A}(\hat{\mathbf{r}}, t)|\psi\rangle = -\mathrm{i}\nabla \cdot \left[\mathbf{A}(\mathbf{r}, t) \langle \mathbf{r}|\psi\rangle\right] \\
&= -\mathrm{i}\{\underbrace{[\nabla \cdot \mathbf{A}(\mathbf{r}, t)]}_{=0} \langle \mathbf{r}|\psi\rangle + \mathbf{A}(\mathbf{r}, t) \cdot [\nabla \langle \mathbf{r}|\psi\rangle]\} \\
&= -\mathrm{i} \int \mathrm{d}\mathbf{r}' \, \mathbf{A}(\mathbf{r}, t) \cdot \delta'(\mathbf{r} - \mathbf{r}') \langle \mathbf{r}'|\psi\rangle = \int \mathrm{d}\mathbf{r}' \, \mathbf{A}(\mathbf{r}, t) \cdot \langle \mathbf{r}|\hat{\mathbf{p}}|\mathbf{r}'\rangle \langle \mathbf{r}'|\psi\rangle \\
&= \int \mathrm{d}\mathbf{r}' \, \langle \mathbf{r}|\mathbf{A}(\hat{\mathbf{r}}, t) \cdot \hat{\mathbf{p}}|\mathbf{r}'\rangle \langle \mathbf{r}'|\psi\rangle = \langle \mathbf{r}|\mathbf{A}(\hat{\mathbf{r}}, t) \cdot \hat{\mathbf{p}}|\psi\rangle
\end{aligned}$$

This is called the velocity gauge (VG) Hamiltonian [27].

An equivalent formulation of the dipole approximation can be obtained from the VG by a gauge transformation with the scalar field $\mathbf{r} \cdot \mathbf{A}_{\mathrm{LG}}(t)$ [165]:

$$\begin{aligned}
\mathbf{A}_{\mathrm{VG}}(t) \rightarrow \quad \mathbf{A}_{\mathrm{LG}}(t) \quad &= \mathbf{A}_{\mathrm{VG}}(t) - \nabla \left[\mathbf{r} \cdot \mathbf{A}_{\mathrm{VG}}(t)\right] = 0; \\
\left|\psi_{\mathrm{VG}}(t)\right\rangle \rightarrow \quad \left|\psi_{\mathrm{LG}}(t)\right\rangle \quad &= e^{\mathrm{i}\mathbf{r}\cdot\mathbf{A}_{\mathrm{VG}}(t)} \left|\psi_{\mathrm{VG}}(t)\right\rangle; \\
V_{\mathrm{VG}}(\hat{\mathbf{r}}, t) \rightarrow \quad V_{\mathrm{LG}}(\hat{\mathbf{r}}, t) \quad &= V_{\mathrm{atom}}(\hat{\mathbf{r}}) - \partial_t \hat{\mathbf{r}} \cdot \mathbf{A}_{\mathrm{VG}}(t) \\
&= V_{\mathrm{atom}}(\hat{\mathbf{r}}) + \hat{\mathbf{r}} \cdot \mathbf{E}(t),
\end{aligned}$$

where $\mathbf{E}(t)$ is the external electric field. Consequently, the Hamiltonian operator in the length gauge (LG) is

$$\hat{H}_{\mathrm{LG}}(t) = \frac{\hat{\mathbf{p}}^2}{2} + V_{\mathrm{atom}}(\hat{\mathbf{r}}) + \hat{\mathbf{r}} \cdot \mathbf{E}(t). \tag{2.5}$$

Both VG and LG are used in numerical and theoretical studies of atoms and molecules in ultrafast laser fields. There has been some discussion on which gauge is numerically more favorable for simulating strong-field phenomena [166, 167], but this choice should not matter for calculated observables as long as the numerical methods are accurate enough and the theoretical approximations preserve the gauge invariance.

2.3 On the use of one-dimensional models

A full three-dimensional (3D) quantum mechanical (QM) description of strong-field processes is computationally challenging as an ionized electron wave packet can travel far from the parent ion. Especially when re-entry of the ionized electron to the vicinity of the ion core is important, we must model the entire travel path of the electron – often requiring large simulation domains.

This issue of a high computational cost is particularly problematic when optimizing strong-field processes – as in this dissertation. In optimization studies, we must solve the quantum dynamics in an iterative optimization process for hundreds if not thousands of times, and the high computational cost of a single simulation accumulates.

However, in linearly polarized laser fields with intensities well below the non-dipole and relativistic regimes, the driving force of the laser field affects the atomic electron only in the polarization direction. Hence, it is often useful to treat the electron dynamics in ultrafast strong fields within a one-dimensional (1D) model.

A traditional choice for the 1D model potential is the *soft Coulomb* potential [168],

$$V(x) = -\frac{1}{\sqrt{x^2 + \alpha^2}}, \tag{2.6}$$

where α is the softening parameter. The soft Coulomb potential supports bound states [169], and – most usefully – there is no singularity at the origin [169]. In addition to the soft Coulomb potential, there are multiple alternative 1D model potentials that offer improved quantitative agreement with 3D simulations (see, e.g., Refs. [170, 171]).

We note that in recent years there have been several developments both in computational power and modeling techniques for strong-field phenomena in atoms. These techniques include, e.g., various approximations for the 3D atomic potential [172], multiresolution schemes [173, 174], improved basis sets [175], domain decomposition [141, 176], and even analytical treatment of some parts of the electron dynamics [141]. These tools can alleviate the computational demand required for the full solution of the 3D TDSE.

2.4 Ionization in strong-fields

When an atom is influenced by a *strong* driving laser field it might be ionized, i.e., emit one or multiple *photoelectrons*. The traditional description of the ionization process provides (essentially) two ionization mechanisms/pictures [177]: multiphoton and tunneling ionization.

In multiphoton ionization [see Fig. 2.1(a)], the atomic electron – initially in its ground state – absorbs multiple photons from the driving laser field [178]. With the absorption of enough photons, the electron is excited to the continuum, and it is free to travel away from the ion core. Multiphoton ionization is typically attributed to relatively weak fields [178].

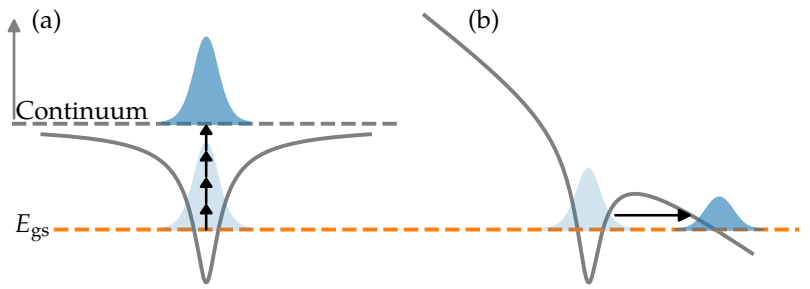

Figure 2.1: Schematic picture of (a) multiphoton and (b) tunneling ionization.

Tunneling ionization provides a completely different picture: The driving laser field bends the total scalar potential (in LG), $V_{\text{atom}}(\mathbf{r}) + \mathbf{r} \cdot \mathbf{E}(t)$ as demonstrated in Fig. 2.1(b). If the field oscillates slowly enough, it is static from the electron's perspective, and the ionization can take place by tunneling through the combined potential barrier of the ion and the driving field [178].

These two mechanisms are often characterized by a single parameter [178], the *Keldysh parameter* [179], which can be written as [178]

$$\gamma = \sqrt{\frac{I_p}{2U_p}}, \tag{2.7}$$

where I_p is the ionization potential of the atom, i.e., the binding energy of the electron, $U_p = I_{\text{max}}/(4\omega^2)$ the ponderomotive energy with I_{max} the peak intensity and ω the carrier frequency of the driving laser.

An intuitive description of the role of γ is provided, e.g., in Ref. [180]: For high-frequency (and/or low intensity) fields, i.e., when $\gamma \gg 1$, the photon energy is large and the absorption of a few photons excites the electron to the continuum; $\gamma \gg 1$ is called the *multiphoton regime*. In contrast, in a low-frequency and/or high-intensity field where $\gamma \ll 1$, multiphoton absorption is a relatively rare event whereas the tunneling probability increases exponentially with the field strength. $\gamma \ll 1$ is called the *tunneling regime*.

Finally, we note that this division of the ionization mechanisms to two separate regimes has attracted some debate (see, e.g., Refs. [177, 181–183]). For example, the tunneling ionization is fundamentally flawed in that the concept of tunneling is only applicable in the LG [183]. In addition, reaching the deep tunneling

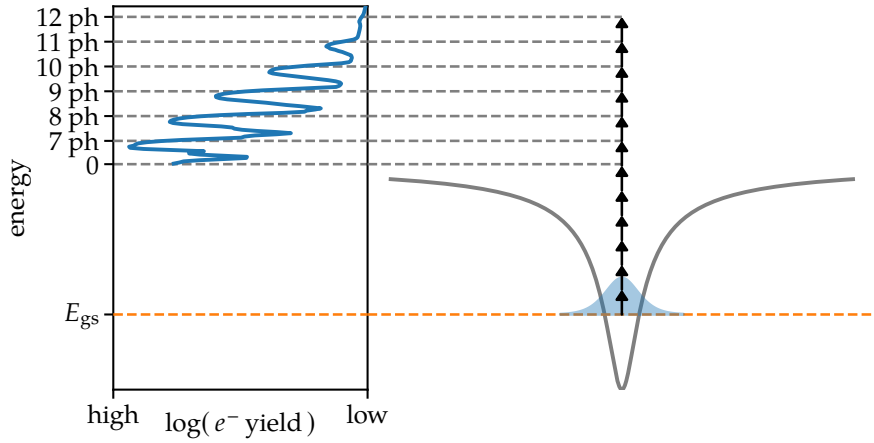

Figure 2.2: Schematic picture of above-threshold ionization explained in terms of multiphoton absorption. The peaks in the photo-electron spectrum (left panel) correspond to the absorption of energy from the driving laser field in discrete quanta. Adapted from Ref. [186].

regime $\gamma \to 0$ by increasing the field intensity either (i) suppresses the tunneling barrier completely thus breaking the tunneling picture [183] or (ii) brings the system to the relativistic domain [182]. In addition, at the interface between the tunneling and multiphoton regimes at $\gamma \sim 1$ combinations of these two ionization mechanisms have been reported [184, 185]. However, while the separation of ionization to *tunneling* and *multiphoton* mechanisms may face problems in certain cases, they provide easy-to-understand intuition behind non-linear strong-field phenomena, and we use them in the following.

2.5 Above threshold ionization

In the multiphoton ionization picture, the atomic electron is excited to the continuum by the absorption of multiple photons. However, the electron can absorb *more* photons than required for reaching the continuum threshold. In such a case, the excess energy is seen as the electron's terminal kinetic energy. Especially when the laser field is nearly monochromatic, the electron can absorb energy only in discrete steps. This process is called above-threshold ionization (ATI), and it results in a peaked photo-electron spectrum (PES) with the ATI

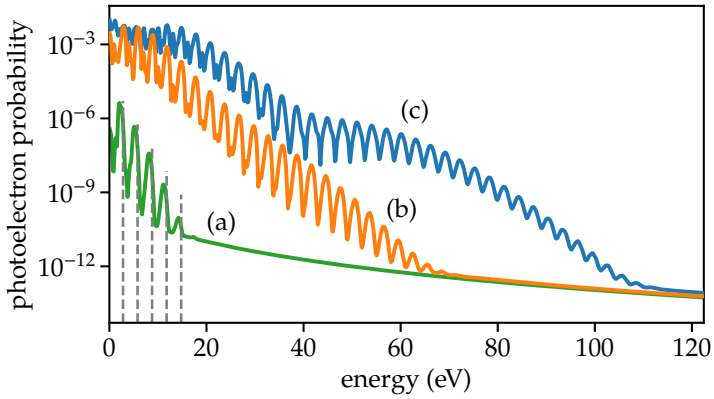

Figure 2.3: Photoelectron spectra for a one-dimensional hydrogen model driven by a 5 fs (intensity full width at half maximum) laser pulse with a 400 nm carrier wave at peak intensities (a) 3.2×10^{13} W/cm^2, (b) 1.7×10^{14} W/cm^2, and (c) 3.5×10^{14} W/cm^2. The dashed lines at the bottom left of the figure show the final energies with $n = 7 \ldots 11$ photon absorption from the ground state.

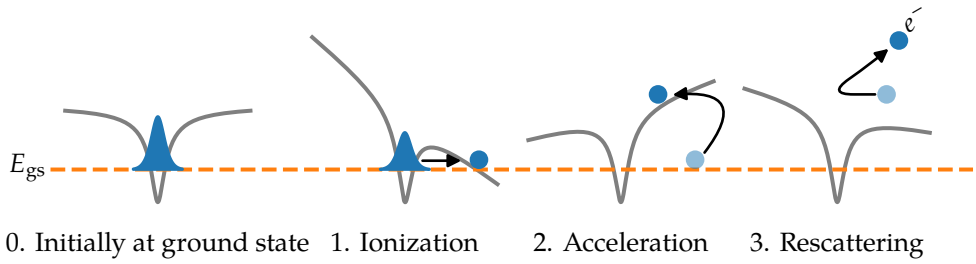

Figure 2.4: Schematic picture of the rescattering mechanism in above-threshold ionization according to the three-step model.

peaks separated by the photon energy of the driving field as demonstrated in Fig. 2.2.

With low intensities, the PES of the ATI process is mostly a rapidly decreasing peaked spectrum as shown in Fig. 2.3(a-b) [187]. With increasing field strengths, the ATI spectrum acquires a *plateau*-like structure as in Fig. 2.3(c). This plateau is the result of a *rescattering* mechanism for which the conventional *three-step model* paints an intuitive picture [25, 26, 187–189].

The *three-step model* is illustrated in Fig 2.4. First, the atomic electron tunnels

out of the atom. It then accelerates in the laser field gaining kinetic energy. If the electron travels away from the parent ion without returning to its vicinity, it contributes to the initial, rapidly decreasing *direct* part of the PES [187].

However, the electron may return to the vicinity of the parent ion and rescatter from it. In *backscattering*, the electron scatters from the ion core elastically [187]. If the electron backscatters from the parent ion just as the force of the laser field flips its direction, it gains kinetic energy from two half-cycles of the laser pulse. Such an electron can reach energies up to $10U_p$ [187]. This *rescattering* part of the spectrum is the one that creates the plateau in the photoelectron spectrum in Fig. 2.3(c).

Recently, the rescattering mechanism has been shown to produce also an additional increase of the yield at low energies [26] (not visible in the example spectra shown here). This low-energy structure is the result of forward-scattering upon return to the vicinity of the parent ion [26] instead of backscattering that results in the high-energy plateau.

As a final note, the photoelectron emission is not typically encumbered with effects from propagating through the gaseous medium. An emitted photoelectron has a negligible cross-section with the rest of the atoms in the gas jet [186], and the experimental spectrum the is often close to the single-atom response. However, differences between the experimental and the single-atom response may arise if the laser focus is not tight enough [186]. In such a case, electron emission at different atomic positions inside the gas medium occurs at different peak laser intensities, and the total measured PES is essentially a weighted sum of the single-atom spectra for different intensities [186].

2.6 Calculating photoelectron spectrum

Semiclassically the photoelectron spectrum is easy to understand as the probability density for the terminal kinetic energy $v^2/2$ of an ionized electron, but the calculation of its QM counterpart is slightly more involved. In quantum mechanics PES corresponds to the probability of finding an electron at a positive-energy E eigenstate $\phi(E)$ of the system Hamiltonian [190], i.e.,

$$P(E) = \sum\!\!\!\!\!\!\int_{\text{degeneracies}} \left|\left\langle \phi(E) \middle| \psi(t \to \infty) \right\rangle\right|^2, \tag{2.8}$$

where we sum and integrate over all degenerate states with energy E.

There are multiple ways to compute or approximate Eq. (2.8). First, we could compute the continuum eigenstates of the system Hamiltonian in the investigated energy range and project the final electronic state to these eigenstates [190]. While this is conceptually easy, it would require an accurate computation of a large set of continuum eigenstates which is computationally an expensive task.

Alternatively, we could approximate the continuum eigenstates $\phi(E)$ as plane waves, i.e., $\left\langle \mathbf{r} \middle| \phi(\mathbf{k}) \right\rangle \propto \exp\left(\mathrm{i}\mathbf{k} \cdot \mathbf{r}\right)$. In this case the angle-resolved PES would be computed simply as a Fourier transformation of the final state.

We can also approximate the projection to eigenstates with a *window function* [191], yielding the approximation

$$P(E) \approx \lim_{t \to \infty} \left\langle \psi(t) \middle| \hat{W} \middle| \psi(t) \right\rangle , \tag{2.9}$$

where the window operator can be written as [191]

$$\hat{W} = \frac{\gamma^4}{(\hat{H}_0 - E)^4 + \gamma^4}. \tag{2.10}$$

These projection methods require us to simulate the system in a large simulation domain so that all of the electron wave function is still inside it at the end of the simulation (i.e., not absorbed by the boundaries). Recent developments have brought also alternative methods such as the time-dependent surface flux -method (tSurff) [141] or the mask method [176]. They allow more efficient simulations by decomposing the simulation domain into an interior region, where the interaction of the electron with its parent ion is non-negligible, and an exterior region, where the electron interacts only with the laser field.

In the mask method, the interior region is typically simulated in the coordinate space and the exterior region in the momentum space [176]. These regions are coupled using a mask function, allowing electron density to pass from the interior region to the exterior region (and vice versa) [176].

In tSurff, we must know the general solution to the TDSE in the exterior region [141]. This general solution is used to transfer the computation of the overlap integral (2.8) in the exterior region to a two-dimensional (2D) surface within the interior region [141]. Since the PES can now be computed by

an integral over a hypersurface in the interior region, one can truncate the simulation domain to only the interior region. This results in a significantly lower computational cost when computing PES.

2.7 Emitted electromagnetic fields

When an atom is influenced by an oscillating field such as a laser field, its dipole moment starts to oscillate. This oscillating dipole moment emits EM radiation, which is measured far away from the interaction region of the gas and the laser field. Formally, one measures the spectrum [192]

$$S_z(\omega) = |E_z(\omega)|^2 = \frac{1}{2\pi}\left|\int_{-\infty}^{\infty} \mathrm{d}t\, E_z(\mathbf{r}, t) e^{\mathrm{i}\omega t}\right|^2, \tag{2.11}$$

where ω is the frequency of the emitted radiation, E_z the z-component of the emitted radiation, and $\mathbf{r}$ the (directed) distance from the dipole emitter.

In the following we clarify how the dipole spectrum $S(\omega)$ measured far away from the interaction region is related to the simulated dipole moment $\langle\psi|\hat{\mathbf{r}}|\psi\rangle$ of a single representative atom at the interaction region. The following derivation follows that of Baggesen and Madsen in Ref. [192], but extends it to a 3D setup. This treatment is similar to the comment on Baggesen's and Madsen's article in Ref. [193], but here we focus on the field emitted by a *single* atom.

The relevant macroscopic Maxwell's equations in their differential form can be written as [194]

$$\mathbf{D}(\mathbf{r}, t) = \mathbf{E}(\mathbf{r}, t) + 4\pi\mathbf{P}(\mathbf{r}, t) \tag{2.12}$$

$$\mathbf{H}(\mathbf{r}, t) = \mathbf{B}(\mathbf{r}, t) - 4\pi\mathbf{M}(\mathbf{r}, t) \tag{2.13}$$

$$\nabla \cdot \mathbf{D}(\mathbf{r}, t) = 4\pi\rho_f \tag{2.14}$$

$$\nabla \times \mathbf{E}(\mathbf{r}, t) = -\frac{1}{c^2}\partial_t \mathbf{B}(\mathbf{r}, t) \tag{2.15}$$

$$\nabla \times \mathbf{H}(\mathbf{r}, t) = 4\pi\mathbf{J}_f(\mathbf{r}, t) + \partial_t \mathbf{D}(\mathbf{r}, t), \tag{2.16}$$

where $\mathbf{D}$ is the dielectric displacement, $\mathbf{E}$ the electric field, $\mathbf{P}$ the polarization, $\mathbf{M}$ the magnetization, $\mathbf{H}$ the magnetic intensity vector, $\mathbf{B}$ the magnetic field,

ρ_f the density of free charges, and $\mathbf{J}_f$ the current density of free charges [195]. Note that we have already previously in Sec. 2.2 absorbed the term $\frac{1}{c}$ into the vector potential $\mathbf{A}$ and here we use this convention also for $\mathbf{B}$, $\mathbf{H}$, and $\mathbf{M}$.

Since we have no free charges and magnetization of a gaseous medium is negligible, the Maxwell's equations simplify to

$$\mathbf{D}(\mathbf{r}, t) = \mathbf{E}(\mathbf{r}, t) + 4\pi\mathbf{P}(\mathbf{r}, t) \tag{2.17}$$

$$\mathbf{H}(\mathbf{r}, t) = \mathbf{B}(\mathbf{r}, t) \tag{2.18}$$

$$\nabla \cdot \mathbf{D}(\mathbf{r}, t) = 0 \tag{2.19}$$

$$\nabla \times \mathbf{E}(\mathbf{r}, t) = -\frac{1}{c^2}\partial_t \mathbf{B}(\mathbf{r}, t) \tag{2.20}$$

$$\nabla \times \mathbf{H}(\mathbf{r}, t) = \partial_t \mathbf{D}(\mathbf{r}, t), \tag{2.21}$$

The EM radiation emitted by the atom will be included later in the polarization term.

By differentiating Eq. (2.21) with respect to time and using Eqs. (2.17) – (2.20), we get the governing equation for the propagation of EM waves emanating from the atom [196],

$$\left(\nabla^2 - \frac{1}{c^2}\partial_t^2\right)\mathbf{E} = \frac{4\pi}{c^2}\partial_t^2\mathbf{P}. \tag{2.22}$$

Note that in this simple model, the atom interacting with the external EM pulse emits radiation which propagates in free space to the detector. This gross approximation is valid only when the gas jet in the experimental setup is extremely thin so that the interaction of the emitted radiation with the gaseous medium is negligible. Often this is not the case and propagation effects should be included rigorously.

The polarization of the atom is given by the atom's dipole moment as

$$\mathbf{P}(\mathbf{r}, t) = \left\langle \psi(t) \middle| \hat{\mathbf{r}} \middle| \psi(t) \right\rangle \delta^3(\mathbf{r}), \tag{2.23}$$

where we have approximated the atom as a point-like source. The governing equation for the propagating radiated field becomes

$$(\nabla^2 - \frac{1}{c^2}\partial_t^2)\mathbf{E} = \frac{4\pi}{c^2}\partial_t^2 \left\langle \psi(t) \middle| \hat{\mathbf{r}} \middle| \psi(t) \right\rangle \delta^3(\mathbf{r}), \tag{2.24}$$

which is the same as Eq. (5) in Ref. [192]. Denoting the dipole moment as $\mathbf{d}(t) \doteq \left\langle \psi(t) \middle| \hat{\mathbf{r}} \middle| \psi(t) \right\rangle$ we can write the wave equation (2.24) in the frequency domain as[3]

$$(\nabla^2 + \frac{\omega^2}{c^2})\mathbf{E}(\mathbf{r}, \omega) = -\frac{4\pi\omega^2}{c^2}\mathbf{d}(\omega)\delta^3(\mathbf{r}). \tag{2.25}$$

Equation (2.25) is the defining equation for the Green's function of the three dimensional Helmholtz equation for each component of $\mathbf{E}$. The physical solution is given by [197]

$$E_\alpha(\mathbf{r}, \omega) = \frac{\omega^2}{c^2} d_\alpha(\omega) \frac{e^{\mathrm{i}\omega\frac{\|\mathbf{r}\|}{c}}}{\|\mathbf{r}\|}, \ \alpha = x, y, z \tag{2.26}$$

or equivalently

$$\mathbf{E}(\mathbf{r}, \omega) = -\frac{1}{c^2}\ddot{\mathbf{d}}(\omega) \frac{e^{\mathrm{i}\omega\frac{\|\mathbf{r}\|}{c}}}{\|\mathbf{r}\|}, \tag{2.27}$$

where $\ddot{\mathbf{d}}(\omega) = \frac{1}{2\pi}\int_{-\infty}^{\infty} \mathrm{d}t \partial_t^2 \left\langle \psi(t) \middle| \hat{\mathbf{r}} \middle| \psi(t) \right\rangle e^{-\mathrm{i}\omega t}$ is the dipole acceleration of a single atom.

Were we now to measure the z-component of the emitted EM signal, it is related to the single-atom response by

$$S_z(\omega) = |E_z(\omega)|^2 = \frac{1}{c^4\|\mathbf{r}\|^2}|\ddot{d}_z(\omega)|^2 \propto |\ddot{d}_z(\omega)|^2. \tag{2.28}$$

This result for 3D wave propagation is slightly different from that of a 1D setup, where the measured spectrum is proportional to the dipole velocity [192],

$$S_{1\mathrm{D}}(\omega) \propto |\dot{d}(\omega)|^2. \tag{2.29}$$

However, the difference is only a factor of ω^2 since $\ddot{d}(\omega) = -\mathrm{i}\omega\dot{d}(\omega)$.

Finally, we point out that the standard way of computing $\ddot{d}_z(\omega)$ from a QM simulation is to compute the dipole acceleration $\ddot{d}_z(t)$ via Ehrenfest's theorem [198],

$$\ddot{\mathbf{d}}(t) = \left\langle \psi(t) \middle| (-\nabla V_{\mathrm{atom}})(\mathbf{r}) \middle| \psi(t) \right\rangle, \tag{2.30}$$

where we have dropped the term with the laser-matter interaction operator as it typically contributes only to the low-frequency part of the spectrum.

[3] Assuming $\mathbf{d}(t = -\infty) = \mathbf{d}(t = \infty) = 0$.

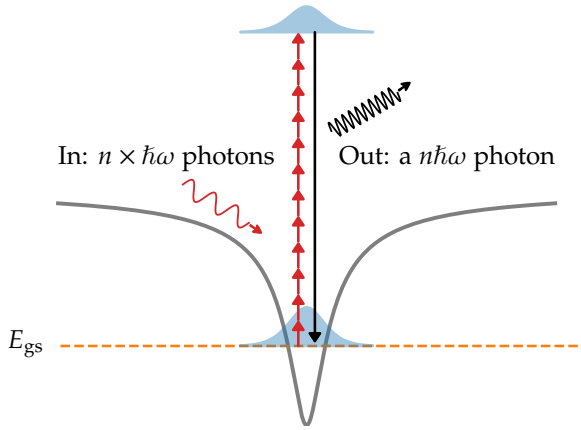

Figure 2.5: Schematic picture of the frequency up-conversion process known as high-order harmonic generation.

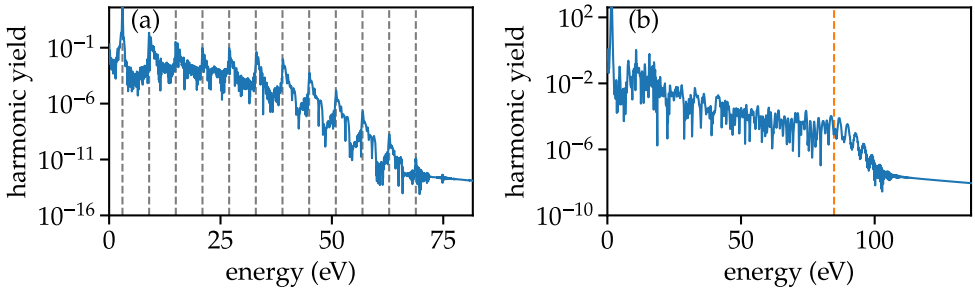

Figure 2.6: Dipole spectra for a one-dimensional hydrogen model using (a) a 400 nm carrier pulse with 60 fs duration (envelope full width at half maximum) and (b) a 800 nm carrier pulse with 12 fs duration (envelope full width at half maximum). Dashed gray lines in (a) show odd harmonics of the driving field, and the orange dashed line in (b) shows the semiclassical cutoff energy.

2.8 High-order harmonic generation

In ATI (Sec. 2.5) the electron might rescatter upon its return to the parent ion leading to the detection of high-energy photoelectrons. However, instead of rescattering the electron might *recombine* back to the ground state and emit all the excess energy it has gathered as a single high energy photon. This phenomenon is called high-order harmonic generation (HHG), and it can be

utilized as a frequency up-converter: the atomic electron absorbs a number of low-energy photons and emits a single high-energy photon (see Fig. 2.5 for an illustration). The spectrum of the emitted radiation can be computed from the oscillating dipole moment of the atom as described in Sec. 2.7.

The high-order harmonic (HH) spectrum for longer (dozens of femtoseconds) driving pulses – demonstrated as the blue line in Fig. 2.6(a) – consists of multiple peaks at odd multiples of the driving frequency [odd harmonics, shown as vertical dashed lines in Fig. 2.6(a)]. The spectrum decreases rapidly for the first few harmonics but reaches a wide *plateau* of a nearly constant yield [27]. The plateau ends abruptly near the cutoff energy $E_c \sim 3.17U_p + I_p$ [199–201]. The cutoff law is demonstrated as the dashed vertical line in Fig. 2.6(b) for a 12 fs pulse with a 800 nm carrier wave.

For near-monochromatic driving pulses we only observe the emission of odd harmonics as demonstrated in Fig. 2.6(a). This can be understood in terms of the single-atom multiphoton picture in Fig. 2.5 [178]: Dipole interaction is allowed only between states of opposite parity [202]. With the absorption of n photons from the driving field, the parity of the state changes by $(-1)^n$. Recombination to the initial state is allowed by the dipole selection rules only if n is odd, i.e., when a high-energy photon with the energy $E = n\omega$ is emitted upon the recombination. For short pulses as in Fig. 2.6(b) most of the harmonic peaks are smoothened out. This can be attributed to the broader bandwidth of the driving pulse [203].

After emission, the harmonics must propagate through the gaseous medium to reach a detector or to be used in applications. In contrast to ATI, the propagation of harmonics is affected by the medium [204, 205]. For example, in order for the intensity of the propagating harmonic radiation to accumulate coherently while propagating through the gas, the phase of the radiation at a certain position must match the phase of the radiation emitted by an atom at the same position [205]. Fortunately, there are methods for addressing the issues arising from macroscopic propagation. For more details, we refer to Ref. [204].

As the final note, HHG driven by few-cycle pulses can be used to generate *isolated attosecond pulses* with energies in the extreme ultraviolet (XUV) [206] and even soft X-ray range [20]. However, even a few-cycle driving pulse generates multiple successive attosecond pulses, one for each recombination window as shown in Fig. 2.7. Here the cutoff harmonics of the spectrum in Fig. 2.6(b) are

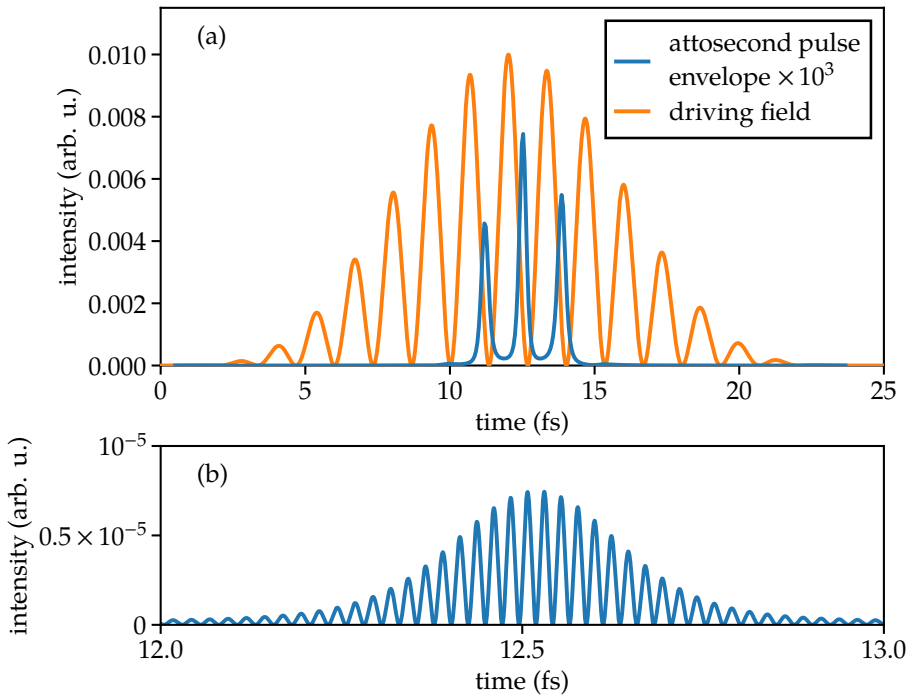

Figure 2.7: (a) Intensity envelopes for the driving laser field and the envelope of the intensity of the attosecond pulse train generated by spectral filtering from the cutoff harmonics of Fig. 2.6(b). (b) Zoom-in to the centermost attosecond pulse in the upper panel, but showing also the carrier oscillation of the intensity profile.

generated in three recombination windows producing three attosecond pulses. An *isolated* attosecond pulse can be generated with multiple techniques (see, e.g., the reviews [13, 204, 207, 208]). These techniques include, e.g., (a) spectral filtering of the HH radiation to include only those cutoff-region harmonics that are generated in the same recombination window [209], (b) allowing HHG only in a short time-window either by controlling the ionization time by tailoring the temporal profile [210] or the time-dependent polarization of the driving field [211, 212], or (c) altering the emission direction for harmonics emitted at different recombination times [213, 214]. Depending on the generation scheme, the resulting attosecond pulse either utilizes the full HH spectrum or just the harmonics in the cutoff region [207].

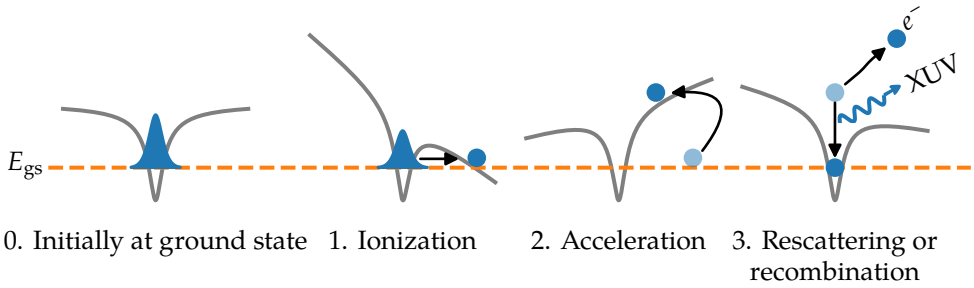

Figure 2.8: Schematic picture of the three-step model. Here the dashed line shows the ground state energy, the gray curves the combined potential of the ion core and laser field, and blue objects the electron in each of the steps.

2.9 Semiclassical model

Let us briefly summarize a unified semiclassical description of ATI and HHG. This *three-step model* is illustrated in Fig. 2.8 [199, 200, 215]. Initially, the electron is in its ground state, from which a wave packet is ionized either by multiphoton or tunneling ionization. After ionization, the electron is accelerated by the laser field. Finally, some electron trajectories may return to the vicinity of the parent ion and either rescatter from it or recombine back to the ground state.

Modeling of the first step, ionization, depends on the ionization regime and mechanism as described in Sec. 2.4. Often the ionization step is modeled as an instantaneous ejection of the electron from the parent ion [199]. There are multiple distributions for the instantaneous emission rate W including, e.g., the Ammosov-Delone-Krainov (ADK) rate [216, 217], the Perelomov-Popov-Terent'ev (PPT) rate [218, 219], and the strong-field approximation (SFA) or the Keldysh-Faisal-Reiss (KFR) transition rate [220, 221]. In the often used ADK and PPT transition rates, the dominant contribution has the form

$$W \sim \exp\left[-\frac{2(2I_p)^{3/2}}{3|\mathbf{E}|}\right], \tag{2.31}$$

where I_p is the ionization potential of the atom and $\mathbf{E}$ the instantaneous electric field [216–219].

Ionization at different times produces an ensemble of classical electron trajectories in the Monte Carlo spirit [199]. The initial conditions of these trajectories

vary between different flavors of semiclassical models. Simplest models initialize the trajectories at the origin [199], which is common when considering multiphoton ionization. In the tunneling regime, non-zero tunnel exit has already been confirmed experimentally [222], and correspondingly theoretical models can use the classical turning-point on the far-side of the tunneling barrier as the initial electron position. Furthermore, the initial velocity can be set to zero [199]. In 3D models, however, the trajectory should have non-zero velocity perpendicular to the direction of the initial ejection [223].

The dynamics of the trajectories of the ensemble follow Newton's equations of motion [26, 199],

$$\ddot{\mathbf{r}} = -\nabla V_{\text{atom}}(\mathbf{r}) - \mathbf{E}(t), \tag{2.32}$$

where V_{atom} is the atomic/molecular potential and $\mathbf{E}(t)$ is the laser electric field. In some models such as the *Simple man's model* [199] the influence of the atomic potential is neglected in the acceleration step.

Those trajectories that propagate away from the parent ion without returning to its vicinity are a part of *direct ionization* in the ATI spectrum (see Sec. 2.5). The Simple man's model provides the maximum kinetic energy of $2U_p$ for direct ionization [26] with $U_p = \left\langle \mathbf{A}^2(t) \right\rangle_T / 2$ being the cycle-averaged kinetic energy of an electron oscillating in a continuous wave (CW) laser field [26].

In addition to direct ionization, some of the trajectories can travel back near the parent ion. There the electron might *rescatter* from the parent ion as discussed in Sec. 2.5 and contribute to the *rescattering* part of the photoelectron spectrum. The rescattering part can reach up to energies $10U_p$ according to the Simple man's model [26].

If, instead of rescattering, the electron *recombines* with the parent ion, it emits the excess energy as a photon. This process results in the generation of HH radiation discussed in Sec. 2.8. The maximum kinetic energy the electron gains in a CW field before returning to the parent ion is $3.17U_p$ according to the Simple man's model. Consequently, the maximum photon energy will be $3.17U_p + I_p$ [199–201, 215], where I_p is the ionization potential of the system.

Finally, note that the energy cutoffs provided by the semiclassical model(s), that is, $2U_p$ for the direct electrons, $10U_p$ for the rescattered electrons, and $3.17U_p + I_p$ for the cutoff energy of the HHG have all been verified in numerous experimental and theoretical studies (see, e.g., Refs. [24, 25, 200, 224–229]).

2.10 Rydberg states

As a slight detour from strong-field physics, let us discuss one peculiar feature of atomic and molecular systems: *Rydberg states*. Rydberg states are high-lying hydrogen-like excited states of atoms [230]. While in hydrogen the energy levels are given by [230]

$$E_n = -\frac{1}{2n^2}, \tag{2.33}$$

with n the principal quantum number, with Rydberg states of other species we have to take into account, e.g., the effective core electron contribution, which yields a slightly modified expression [230]

$$E_{n,l} = -\frac{1}{2(n-\delta_l)^2}, \tag{2.34}$$

where δ_l is the *quantum defect* that depends on the angular quantum number l.

Atoms with a single electron excited to a Rydberg state are called Rydberg atoms [230]. There are numerous atomic species supporting high-lying Rydberg states including, e.g., all neutral atoms [230–232], rare gas dimers [233], and even larger molecules such as water [234] and benzene [235].

Rydberg atoms are characterized by long lifetimes [231, 236] even at finite temperatures [230, 237], large extent of the electron wave function [230], and large dipole moments [230]. Large dipole moments couple nearby Rydberg atoms together [237]. In addition, by controlling the quantum state of the Rydberg atoms, their interatomic interaction strength can be varied within 12 orders of magnitude [237]. Nowadays, Rydberg atoms can be arranged in 2D [238] and even 3D [239] lattices by the use of optical tweezers [130, 240, 241]. These structures are prime candidates for multi-qubit platforms in quantum computing applications [237, 239].

3 Control of ultrafast strong-field phenomena

3.1 On finding recipes for quantum control

In *quantum control* the aim is to tune parameters of a quantum mechanical (QM) system to steer its temporal evolution to achieve a pre-defined goal. The goal is quantified by the *target*, which can be formulated in terms of any observable quantity such as the photo-electron spectrum (PES) or the local electron density. In laser-driven phenomena, the variable parameters, i.e., the *control parameters*, come in the form of the temporal or the spectral shape of the driving laser. In atomic and molecular systems, successful control has been demonstrated in, e.g., selective molecular bond breaking [86–89] and bond formation [89–91], enhancement of atomic strong-field phenomena such as above-threshold ionization (ATI) [23, 242–246] and high-order harmonic generation (HHG) [92–120], and selective electron excitation [247–250].

There are various methods for finding suitable mechanisms and recipes for quantum control. Most importantly, human invention and detailed studies of the phenomenon of interest play a major role. Studies provide insights into possible physical processes and mechanisms, which can be used to formulate precise control recipes. For example, a necessary prerequisite for the invention of polarization gating in the generation of isolated attosecond pulses [211, 212] was to understand the recombination mechanism of HHG: by tailoring the polarization of the driving field, we can steer electron trajectories so that only those corresponding to a single recombination window pass near the parent ion, consequently limiting HHG to a sub-cycle window and producing an isolated attosecond pulse.

Alternatively to direct human invention of control mechanisms, algorithmic search has proven to be a valuable method. It is implemented in a closed-loop system where a laser pulse is used to drive the QM process of interest. The

outcome of the process, the *feedback*, is provided to a computer which further adjusts the driving laser for steering the system to better achieve the target [251–254]. The adjustment of the laser parameters is an *optimization* problem: find a laser pulse that *maximizes* or *minimizes* the target. Setups where the *feedback* is provided by an experimental measurement are called adaptive feedback control (AFC) experiments. Alternatively, the system response can also be computed from a theoretical model.

There are two categories of algorithms for designing the driving laser pulses: gradient-free and gradient-based algorithms. In AFC experiments, evolutionary algorithms, which are gradient-free, are almost exclusively used [252, 253]. In contrast, the gradient-free algorithms in theoretical searches for control methods are often various trust-region and coordinate descent -type algorithms [97, 255–259]. Recently, also machine learning methods have shown success in quantum control [260].

In addition to gradient-free methods, theoretical search for control pulses can utilize the *gradient* of the target. The gradient is computed within the framework of quantum optimal control theory (QOCT), which provides a straightforward way of computing the gradient of the target with respect to the laser parameters [251, 252, 261]. When the laser pulse, switched on at $t = t_0$ and switched off at $t = T$, is defined by a finite number of parameters $\mathbf{u}$, the gradient of the target $G[\mathbf{u}] = \left\langle \psi[\mathbf{u}](T) \middle| \hat{O} \middle| \psi[\mathbf{u}](T) \right\rangle$ can be calculated from [262]

$$\nabla_{\mathbf{u}} G = 2 \operatorname{Im} \int_{t_0}^{T} \mathrm{d}t \left\langle \chi[\mathbf{u}](t) \middle| \left\{ \nabla_{\mathbf{u}} \hat{H}[\mathbf{u}](t) \right\} \middle| \psi[\mathbf{u}](t) \right\rangle , \tag{3.1}$$

where $\left|\psi[\mathbf{u}](t)\right\rangle$ is the wave function of the system and $|\chi[\mathbf{u}](t)\rangle$ a Lagrange multiplier that can be computed by propagating the time-dependent Schrödinger equation (TDSE) backwards in time from the final state $|\chi[\mathbf{u}](T)\rangle = \hat{O} \left|\psi[\mathbf{u}](T)\right\rangle$ [262]. There are also alternative formulations where the laser pulse is represented directly in the time domain, allowing more freedom in the optimization [252].

When designing laser pulses based on numerical simulations, a number of issues can hinder their applicability and success in experimental realizations. First, the numerical simulations may not reproduce the experimental dynamics to a required degree of accuracy [252]. This may be due to using only approximate

models in the simulations or the experimental setup may not be able to produce the designed laser pulse accurately enough [252]. However, with careful numerical simulations, the designed pulses can be successfully applied in experimental setups (see, e.g., Ref. [99]).

Additional challenges in the numerical search for control mechanisms are posed by the compatibility with experimental setups. Experimental constraints on the driving laser field include, e.g., maximum achievable peak intensity, fixed set of available wavelengths, minimum duration of generated pulses, and other possible spectral and temporal restrictions on the waveform of the laser field. In numerical optimization simulations these constraints can be included as *penalty* terms in the target functional [252, 263], as Lagrange multipliers [252] or slack variables [264], by spectral filtering of the laser field during optimization [252], as a mapping of the constrained parameter space to an unconstrained one, or directly in the optimization algorithm [265]. While without constraints on the laser field, the *optimization landscape*, i.e., the graph of the target function(al) $G[\mathbf{u}]$ is known to have few difficult features such as local extrema or singularities [266], enforcement of constraints populates the optimization landscape with problematic areas which hinder efficient optimization [267, 268].

Finally, recent techniques in gamification [269] and citizen science [270] have opened up the possibility for crowd-sourcing quantum optimization problems to human individuals [271–273]. The core idea is to convert the optimization problem, such as speeding up transfer of atoms with optical tweezers [271, 272], to a *game*. The game is distributed to a large audience who, by playing the game, find and optimize control methods for the QM process [271, 272]. Crowd-sourced optimization has proven to quickly find promising subspaces in the search space which can be further optimized with conventional strategies [272]. However, the jury is still out whether crowd-sourced search for quantum control can outperform modern algorithms [274].

3.2 Tailoring femtosecond laser pulses

Control and optimization of atomic and molecular processes driven by laser pulses requires laser pulses whose spectral or temporal profile can be shaped. The idea is to take multiple different laser pulses, *channels*, $E_i(t)$ whose prop-

erties such as intensity, carrier-envelope phase (CEP), and duration can be adjusted. The total laser field is constructed as a coherent superposition of these pulses, $E(t) = \sum_i E_i(t)$.

A schematic illustration of the first modern pulse synthesizer is shown in Fig. 3.1(a) [84]. The device is seeded with a broadband laser pulse which is subsequently split into three *spectral channels*: near-infrared (NIR) (red), visible (VIS) (yellow), and VIS/ultraviolet (UV) (blue) frequencies. The spectra of each of the three channels is shown in Fig. 3.1(b) together with the spectrum of the seed pulse [84]. The pulse in each spectral channel is compressed to a few femtosecond duration [Fig. 3.1(c)], and by adjusting intensities, CEP, chirp, and time-delays between these channels, the temporal profile of the output pulse can be modified [84].

In the first demonstration of sub-cycle tailoring of the laser pulse, the peak intensity and the spectral range were limited by the seed pulse [83, 84]. More recently, the emergence of optical parametric chirped-pulse amplification (OPCPA) [85] has allowed the generation and, more importantly, the amplification of each channel separately [275–277] yielding extreme peak intensities – even deep in the relativistic regime [277]. Finally, the emergence of attosecond nanophotonics [278] suggests the possibility of generating tailored femtosecond pulses even in nanoscale devices [279].

3.3 Algorithmic search for control of laser-driven atomic processes

Algorithmic learning of controls and optimization of laser-driven atomic and molecular processes such as HHG, ATI, ionization, and excitation paths has been studied intensively. In the following we will review some of these previous works to give an idea on the state of the field.

Optimization and control of HHG has been reviewed, e.g., in Refs. [92, 280]. Both the high-order harmonic (HH) cutoff energy and the yield of the high-energy plateau have been increased in numerical experiments by optimizing the spectral properties of the driving laser [107, 109] or by optimizing few-channel synthesized pulses [97, 98, 281]. Note also that the optimization of

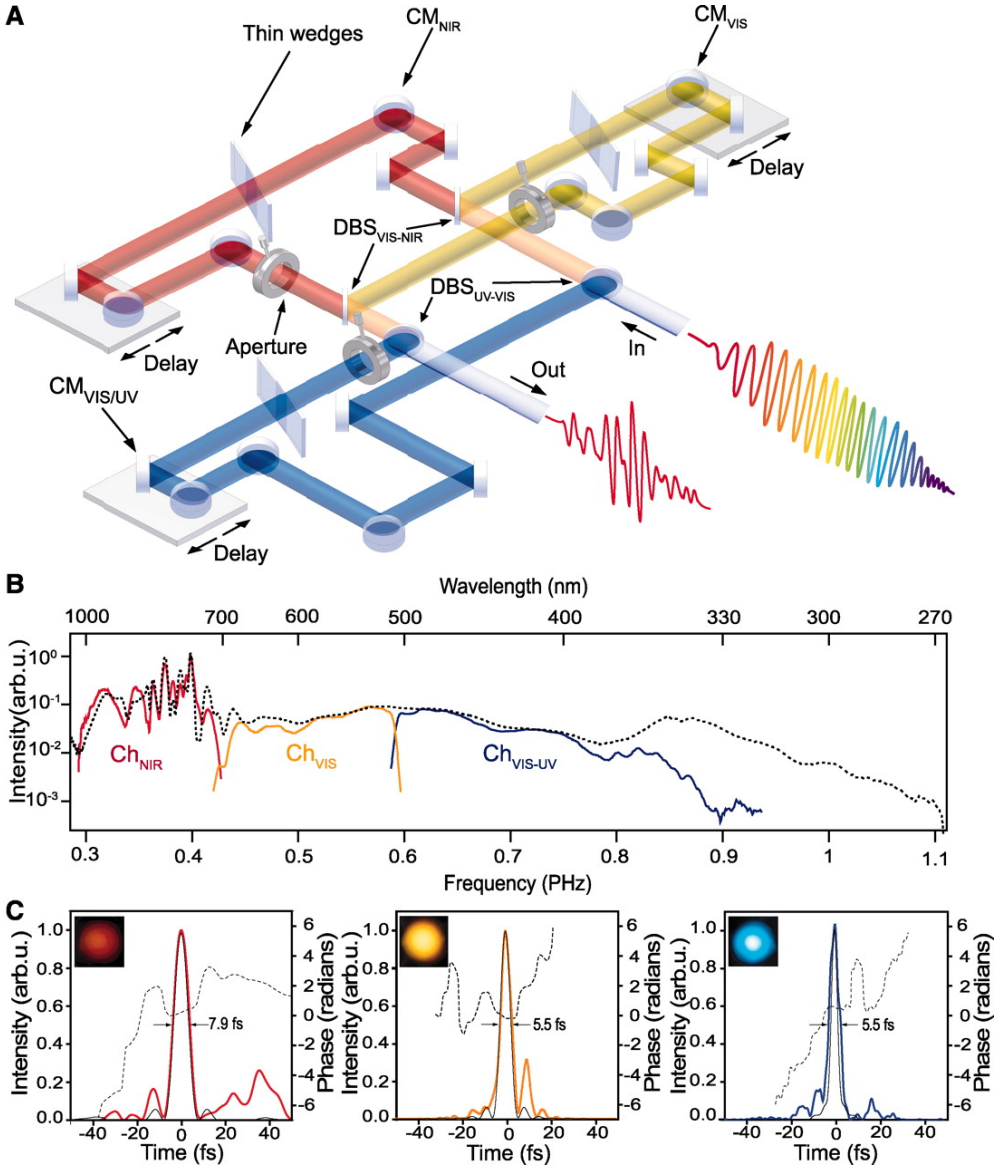

Figure 3.1: (a) Schematic illustration of a three-channel laser pulse synthesizer. (b) Power spectral density of each of the three channels of the device. (c) Visualization of the intensity profiles of the individual channels. Reprinted from Ref. [84] with permission from The American Association for the Advancement of Science.

the single-atom response has been shown to be effective also in optimizing the HH radiation that has propagated through the gaseous medium [120], and some of the pulses from numerical/theoretical computations have also been verified in experimental realizations [99]. In addition to plateau and cutoff optimization, control of the emission of *single* harmonics has attracted attention. On the numerical side, optimization of the dipole response from strong-field approximation (SFA) [282], TDSE [283], and even including many-body effects via time-dependent density functional theory (TDDFT) [284] have demonstrated enhancement of single harmonics. Also, optimization for single-harmonic enhancement has been successful in AFC experiments [285, 286].

Pulse shaping techniques also provide ways for optimizing the ionization processes in atoms. Numerical studies within QOCT have demonstrated optimal control of, e.g., instantaneous ionization rate [287, 288], total ionization probability [289, 290], and suppression of ionization [107, 291]. Also experimental control has been demonstrated [292]. As a step forward, also optimal control of the kinetic energy spectrum of the ionized electrons has been demonstrated [246]. Note that numerical and experimental optimization experiments of ionization compare favorably [293], validating again the use of single-atom response in the theoretical search for control mechanisms.

Finally, precise control of the excitation of atoms to their (meta)stable states, and a-priori selection of the target state or even the excitation pathway would be the ultimate control of laser-driven processes in atoms. These are important steps in using atoms as a basis for multi-qubit quantum computing [237, 239]. There has been some progress in this direction: For example, AFC experiments have demonstrated optimization of pulses for the excitation of rubidium dimers [294], the $|3s\rangle \rightarrow |4s\rangle$ and $|3s\rangle \rightarrow \left|7p\right\rangle$ transitions in sodium [295–297], time-dependent control of Rydberg-state ionization [298], and the generation of localized Rydberg wave-packets [299].

4 Numerical methods

4.1 Overview

In Ch. 2 we reviewed the semiclassical and quantum models for the time-evolution of an atomic electron. The equations of motion of these models are rarely analytically solvable, and therefore, we commonly use numerical methods to compute their solutions. Numerical methods for solving ordinary differential equations (ODEs) and partial differential equations (PDEs) have become standard tool in the scientific community since the early 20th century [300, 301]. "Computers" used to refer to the laborers manually computing the numerical solutions [300, 301], but since the 1940s the scientific community has switched to digital computers [301]. In this chapter we introduce some (semi) modern numerical methods we have used in our studies.

4.2 Simulations with the semiclassical model

4.2.1 Overview

The semiclassical model of laser-atom interaction, introduced already in Sec. 2.9, consists of three steps:

1. generation of an ensemble of electron trajectories via laser-induced ionization
2. propagation of the ensemble per Newton's equations, and
3. rescattering and/or recombination effects.

Numerical simulation of the semiclassical model proceeds as follows. First, a large ensemble of ionization times is sampled using one of the techniques

introduced in Sec. 4.2.2. Next, the corresponding tunnel exits are computed with a root-finding method with the recipe given in Sec. 4.2.3, and finally the ensemble of trajectories is propagated in the combined field of the parent ion and the laser electric field as described in Sec. 4.2.4.

4.2.2 Generating the initial ensemble

The unnormalized ionization rate at time t is given (in the first approximation) by [216–219]

$$W(t) \sim \exp\left[-\frac{2(2I_p)^{3/2}}{3\|\mathbf{E}(t)\|}\right], \tag{4.1}$$

where I_p is the ionization potential of the atomic species and $E(t)$ is the electric field at the time of the ionization. The ionization times t, i.e., the starting times for the semiclassical electron trajectories, are computed by drawing random numbers from the ionization rate distribution $W(t)$.

For the most common probability distributions such as uniform, normal, or binomial distribution, we have a number of methods for drawing random samples efficiently [302, 303]. However, these methods are highly specialized and cannot sample distributions of different forms, such as given by the ionization rate $W(t)$. The simplest way to sample a general probability distribution $W(t)$ is by rejection sampling [304]. The idea is to transform the problem of sampling from the distribution W to a sampling from another, easier to sample distribution $g(t)$. Rejection sampling is described below in Algorithm 1.

Algorithm 1 Rejection sampling algorithm [304]

$M \leftarrow \min_t \frac{g(t)}{W(t)}$
$t \leftarrow$ draw a sample from g
$u \leftarrow$ draw a sample from Unif$(0, 1)$[1]
if $u \leq \frac{W(t)}{Mg(t)}$ **then**
    return t
else
    Repeat from the beginning
end if

[1]Here Unif$(0, 1)$ is the uniform probability distribution yielding values between 0 and 1.

While rejection sampling is easy to implement, it suffers from a few drawbacks. For example, rejection sampling discards a large number of samples, especially if the helper distribution g is quite different from the target distribution W [304]. This makes the algorithm generally quite inefficient [304], and the issue is even worse for high-dimensional distributions.

Alternative methods include, e.g., the Markov chain Monte Carlo (MCMC) approach [304]. MCMC methods generate a Markov chain $t_0, t_1, \ldots, t_n$ whose stationary distribution $P(t)$ is the target distribution $W(t)$ after a few initial steps [304]. One of the simplest MCMC algorithms, Metropolis-Hastings, is described in Algorithm 2 below.

Algorithm 2 Metropolis-Hastings algorithm [304]

Select an initial state $t_0 = 0$.
for $k = 0, \ldots N$ **do**
  $t' \leftarrow$ draw a sample from $g(t'|t_k)$
  $r \leftarrow \min\left(1, \frac{W(t')}{W(t_k)} \frac{g(t_k|t')}{g(t'|t_k)}\right)$
  $u \leftarrow$ draw a sample from Unif$(0, 1)$
  if $u \leq r$ **then**
    $t_{k+1} = t'$
  else
    $t_{k+1} = t_k$
  end if
end for

4.2.3 Computing the tunnel exit

After we have obtained a set of ionization times, we must compute an initial configuration for the ionized electron. The initial position of an electron trajectory generated at time t is given (in the first approximation) by the classical turning point equation [222, 305],

$$V(r) + rE(t) = -I_p, \tag{4.2}$$

where V is the atomic potential, and r the distance from the ion core in the direction of the laser polarization. In the multiphoton and tunneling regimes,

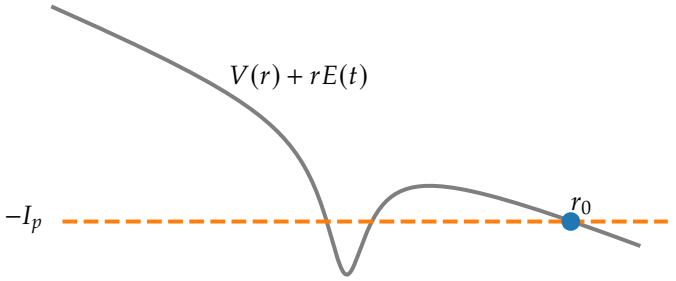

Figure 4.1: In the semiclassical model, the initial position of the electron trajectory corresponds to the further classical turning point, r_0.

Eq. (4.2) has three solutions as demonstrated in Fig. 4.1, and the initial position is the turning point r_0 furthest away from the ion core.

Eq. (4.2) can be solved numerically with any root-finding method applied to the function $f(x) = V(x) - xE(t) + I_p$. For example, the most efficient algorithm is currently [306] the algorithm 4.2 in Ref. [307] (called `TOMS748` in the following). `TOMS748` requires an interval $[a, b]$ with only a single root and $f(a)f(b) < 0$ [307]. For the soft Coulomb potential (see Sec. 2.3), which we will use later in our one-dimensional (1D) simulations, the limits $-\frac{1}{x} < V(x) < 0$ yield

$$a = \frac{\sqrt{I_p^2 - 4\|\mathbf{E}(t)\|} + I_p}{2\|\mathbf{E}(t)\|}, \text{ and} \tag{4.3}$$

$$b = \frac{I_p}{\|\mathbf{E}(t)\|}. \tag{4.4}$$

Open-source implementations of `TOMS748` can be found, e.g., in `SciPy` [306] or `Boost` [308].

4.2.4 Propagating the ensemble

After the stochastic generation of an ensemble of initial conditions for the electron trajectories, $\mathcal{E} = \left\{\left[t_0^{(k)}, x_0^{(k)}, \dot{x}_0^{(k)}\right]\right\}_{k=0}^{N-1}$, we must compute their time-evolution.[2] The trajectories evolve according to classical mechanics, i.e., (in

[2]Note that in 1D simulations we set the initial velocity to zero.

1D)

$$\frac{\mathrm{d}x}{\mathrm{d}t} = \dot{x} \tag{4.5}$$

$$\frac{\mathrm{d}\dot{x}}{\mathrm{d}t} = F_{\mathrm{atom}}(x) - xE(t), \tag{4.6}$$

where $x, \dot{x}$ are the position and velocity of the electron, F_{atom} the force exerted by the parent ion, and $E(t)$ the instantaneous laser electric field. To simplify the notation, let us rewrite this equation as

$$\frac{\mathrm{d}\mathbf{z}}{\mathrm{d}t} = \mathbf{f}(t, \mathbf{z}), \tag{4.7}$$

where $\mathbf{z} = [x, \dot{x}]^{\mathrm{T}}$ and $\mathbf{f}(t, \mathbf{z}) = [\dot{x}, F_{\mathrm{atom}}(x) - xE(t)]^{\mathrm{T}}$.

A numerical solution of this ODE builds a sequence of approximate values of the true solution,

$$\mathbf{z}(t_0), \mathbf{z}(t_1), \ldots, \mathbf{z}(t_i), \ldots, \mathbf{z}(t_n), \tag{4.8}$$

at finite number of time-instants t_i ranging from the ionization time to the end of the simulation. This kind of numerical time-stepping can be obtained with a number of algorithms including, e.g., one from the Runge-Kutta (RK) family.

In RK algorithms, the *time stepping*, i.e., the time-evolution from t_i to t_{i+1}, is obtained from [309]:

$$\mathbf{k}_1 = \mathbf{f}(t_i, \mathbf{z}_i) \tag{4.9}$$

$$\mathbf{k}_2 = \mathbf{f}(t_i + c_2 h, \mathbf{z}_i + h a_{2,1} \mathbf{k}_1) \tag{4.10}$$

$$\vdots \tag{4.11}$$

$$\mathbf{k}_s = \mathbf{f}(t_i + c_s h, \mathbf{z}_i + h(a_{s,1}\mathbf{k}_1 + \cdots + a_{s,s-1}\mathbf{k}_{s-1})) \tag{4.12}$$

$$\mathbf{z}_{i+1} = \mathbf{z}_i + h(b_1 \mathbf{k}_1 + \cdots + b_s \mathbf{k}_s), \tag{4.13}$$

where different constraints and solutions of the coefficients a, b, and c yield different RK schemes [309].

A particularly efficient RK scheme called `DOP8(5,3)` was given in Ref. [309]. `DOP8(5,3)` begins by constructing an 8th order RK scheme. The 8th order RK scheme is accompanied by 5th and 3rd order RK schemes with errors [309]:

$$\mathrm{err}_5 = \left\| \mathbf{z}^{8\text{th order}} - \mathbf{z}^{5\text{th order}} \right\| = O(h^6) \text{ and} \tag{4.14}$$

$$\mathrm{err}_3 = \left\| \mathbf{z}^{8\text{th order}} - \mathbf{z}^{3\text{rd order}} \right\| = O(h^4), \tag{4.15}$$

which are combined to yield a high order *estimate* for the error [309]:

$$\mathrm{err} = \frac{\mathrm{err}_5^2}{\sqrt{\mathrm{err}_5^2 + 0.01\mathrm{err}_3^2}} = O(h^8). \tag{4.16}$$

The above error estimate can be used for *adapting* the time step h during the time propagation as follows [309]. A trial step from t_i to $t_{i+1} = t_i + h$ is made with a step-size h. If the estimated error is smaller than a given tolerance, the step is accepted, and an optimal step-size for the next time step can be estimated from [309]

$$h_{\mathrm{opt}} = \frac{h}{\sqrt[4]{\mathrm{err}}}. \tag{4.17}$$

However, if the error estimate is larger than the given tolerance, the computed step is rejected, a smaller step-size is selected with Eq. (4.17), and time-stepping is attempted again. For more details, we refer the reader to Ref. [309].

This *adaptive time-stepping* allows `DOP8(5,3)` to adjust and correct the numerical time-evolution to keep the local error within pre-described tolerances. An open-source implementation of `DOP8(5,3)` can be found, e.g., in Ref. [309], and there are wrappers and implementations of `DOP8(5,3)` in multiple programming languages [306, 310, 311].

4.3 Solving Schrödinger's equation

The quantum mechanical (QM) description of the laser-atom interaction is based on the Schrödinger equation (see Sec. 2.2). Both the time-independent Schrödinger equation (TISE) and time-dependent Schrödinger equation (TDSE) are linear PDEs whose numerical solution is based on reducing the (often) infinite-dimensional problem to a finite dimensional approximation. This process is called *discretization* of the equations.

4.3.1 Time-independent Schrödinger equation and discretization

First, let us consider different ways to discretize the TISE. TISE is an eigenvalue problem for the time-independent Hamiltonian operator $\hat{H}_{\mathrm{TI}}$,

$$\hat{H}_{\mathrm{TI}} \left|\psi^{(n)}\right\rangle = E^{(n)} \left|\psi^{(n)}\right\rangle, \tag{4.18}$$

where $E^{(n)}, \left|\psi^{(n)}\right\rangle$ is the nth eigenpair of the equation.

If we describe the (single-particle) TISE in the coordinate space, it can be written as

$$\left[-\frac{\boldsymbol{\nabla}^2}{2} + V(\mathbf{r})\right] \psi^{(n)}(\mathbf{r}) = E_k \psi^{(n)}(\mathbf{r}),\ \mathbf{r} \in \Omega, \tag{4.19}$$

where $V(\mathbf{r})$ is the potential of the system and Ω its spatial domain. TISE also requires some boundary conditions (BCs), which in QM simulations are typically zero Dirichlet boundary conditions (ZDBCs), i.e., $\psi^{(n)}(\partial\Omega) = 0$.

In the finite difference (FD) method, we discretize the Laplacian $\boldsymbol{\nabla}^2$ with a FD approximation. For example, in 1D we can approximate [312]

$$\boldsymbol{\nabla}^2 \psi^{(n)}(x) \approx \frac{\psi^{(n)}(x + \Delta x) - 2\psi^{(n)}(x) + \psi^{(n)}(x - \Delta x)}{\Delta x^2}, \tag{4.20}$$

where Δx is the *grid spacing*. This reduces the problem of finding out the values of the wave function in all points of the domain Ω to finding out the wave function values at a *finite* number of points $\mathbf{r} \in \Omega$.

As a concrete example, let us consider the 1D TISE on an interval $\Omega = [a, b] \subset \mathbb{R}$. We first discretize the domain to N grid points,

$$[a, b] \to \mathbf{x} = \{x_0 = a, x_1 = x_0 + \Delta x, \ldots, x_{N-1} = x_0 + (N-1)\Delta x = b\}, \tag{4.21}$$

and denote the values of the nth eigenstate $\psi^{(n)}$ at these points by

$$\boldsymbol{\psi}^{(n)} = \left\{\psi_0^{(n)}, \psi_1^{(n)}, \ldots, \psi_k^{(n)} = \psi^{(n)}(x_0 + k\Delta x), \ldots, \psi_{N-1}^{(n)}\right\}. \tag{4.22}$$

The TISE with our FD Laplacian must hold in all grid points $x_k = x_0 + k\Delta x$, i.e.,

$$-\frac{1}{2\Delta x^2}\psi_{k-1}^{(n)} + \left[\frac{1}{\Delta x^2} + V(x_k)\right]\psi_k^{(n)} - \frac{1}{2\Delta x^2}\psi_{k+1}^{(n)} = E^{(n)}\psi_k^{(n)}. \tag{4.23}$$

This is a standard eigenvalue problem for the matrix

$$H_{\text{TI}}^{\text{FD}} = \begin{bmatrix} \frac{1}{\Delta x^2} + V(x_0) & -\frac{1}{2\Delta x^2} & 0 & \cdots & 0 \\ -\frac{1}{2\Delta x^2} & \frac{1}{\Delta x^2} + V(x_1) & -\frac{1}{2\Delta x^2} & \ddots & \vdots \\ 0 & -\frac{1}{2\Delta x^2} & \frac{1}{\Delta x^2} + V(x_2) & \ddots & 0 \\ \vdots & \ddots & \ddots & \ddots & -\frac{1}{2\Delta x^2} \\ 0 & \cdots & 0 & -\frac{1}{2\Delta x^2} & \frac{1}{\Delta x^2} + V(x_{N-1}) \end{bmatrix}. \tag{4.24}$$

ZDBCs are trivial to enforce by zeroing the rows and columns corresponding to a boundary point x_k in our grid and setting unity on the corresponding diagonal.

The FD discretization yields a finite eigenvalue problem

$$\mathbf{H}_{\mathrm{TI}}^{\mathrm{FD}} \boldsymbol{\psi}^{(n)} = E^{(n)} \boldsymbol{\psi}^{(n)}, \tag{4.25}$$

which can be solved with standard solvers [313, 314], but also specialized algorithms exist for TISE [315].

Alternatively to the FD method, we can discretize the *solution space* $\mathcal{H}$. The standard technique is to select an N-dimensional subspace $\mathcal{H}_N \in \mathcal{H}$ and find a basis for it, $\left\{\left|\phi_0\right\rangle, \ldots, \left|\phi_{N-1}\right\rangle\right\}$. By linearity of the Schrödinger equation, we obtain again a finite-dimensional eigenvalue problem for the expansion coefficients $\boldsymbol{\psi}^{(n)}$. However, in contrast to the FD method, we now face a *generalized* eigenvalue problem,

$$\mathbf{H}_{\mathrm{TI}}^{\mathrm{EM}} \boldsymbol{\psi}^{(n)} = E^{(n)} \mathbf{S}^{\mathrm{EM}} \boldsymbol{\psi}^{(n)}, \tag{4.26}$$

where $\mathbf{H}_{\mathrm{TI};i,j}^{\mathrm{EM}} = \left\langle \phi_i \middle| \hat{H}_{\mathrm{TI}} \middle| \phi_j \right\rangle$ is the Hamiltonian matrix and $\mathbf{S}_{i,j}^{\mathrm{EM}} = \left\langle \phi_i \middle| \phi_j \right\rangle$ the overlap matrix in our basis.

Let us consider a concrete example of the discretization of the solution space, e.g., the cylindarically symmetric three-dimensional (3D) TISE,

$$-\frac{1}{2\rho}\frac{\partial}{\partial\rho}\left(\rho\frac{\partial\psi^{(n)}}{\partial\rho}\right) - \frac{1}{2}\frac{\partial^2\psi^{(n)}}{\partial z^2} + V(\rho, z)\psi_k^{(n)} = E^{(n)}\psi^{(n)}, \tag{4.27}$$

where ρ and z are the cylindrical coordinates and we have set the magnetic quantum number m to zero. We set continuity boundary condition at $\rho = 0$, i.e.,

$$\lim_{\rho\to 0+}\left(\rho\frac{\partial\psi}{\partial\rho}\right) = 0, \tag{4.28}$$

and ZDBCs elsewhere on the domain boundary denoted by Γ; See the left panel of Fig. 4.2 for an illustration of the setup.

In the finite element method (FEM), we discretize the solution space as follows. First, we separate the (coordinate-space) domain Ω to a finite number of elementary elements, e.g., triangles in our case (see Fig. 4.2). The basis

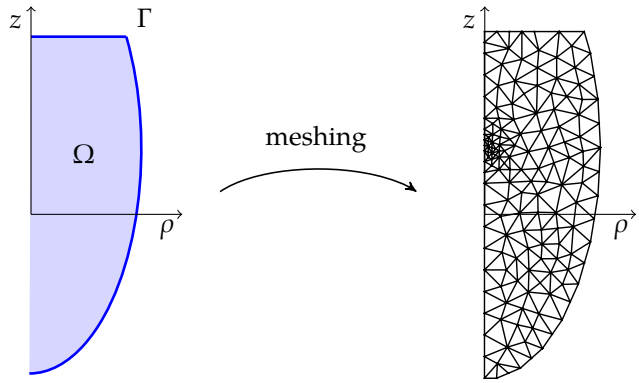

Figure 4.2: Meshing of the simulation domain Ω (cylindrical coordinates) constructs an approximation of the domain as a union of a finite number of elements, e.g., triangles in a two-dimensional case. Adapted from **Paper IV**.

functions $\phi_k(\rho, z)$ for the finite-dimensional approximation of the solution space are then chosen as low-order Lagrange polynomials which are non-zero only on a few neighboring elements.

This choice of basis functions yields sparse system matrices. The overlap matrix in FEM is trivially given by

$$\mathbf{S}^{\text{FEM}}_{\text{TI};i,j} = \langle \phi_i | \phi_j \rangle = \int_\Omega \mathrm{d}\rho \mathrm{d}z \, \rho \phi_i \phi_j, \tag{4.29}$$

and the elements are non-zero only between those basis functions whose supports overlap. The Hamiltonian matrix is slightly trickier as we need to decrease the order of the differential operator in the kinetic energy term. This can be accomplished using the Green's first identity yielding the result

$$\begin{aligned} \mathbf{H}^{\text{FEM}}_{\text{TI};i,j} &= \langle \phi_i | \hat{H}_{\text{TI}} | \phi_j \rangle \\ &= -\frac{1}{2} \int_\Omega \mathrm{d}\rho \mathrm{d}z \, \rho \sum_{\alpha=\rho,z} \frac{\partial \phi_i}{\partial \alpha} \frac{\partial \phi_j}{\partial \alpha} \\ &\quad + \int_\Omega \mathrm{d}\rho \mathrm{d}z \, \rho \phi_i V(\rho, z) \phi_j, \end{aligned} \tag{4.30}$$

where the boundary integrals have vanished due to ZDBCs. This procedure is described in more detail in, e.g., **Paper IV**. Finally, we obtain a generalized eigenvalue equation

$$\mathbf{H}_{\mathrm{TI}}^{\mathrm{FEM}}\boldsymbol{\psi}^{(n)} = E^{(n)}\mathbf{S}^{\mathrm{FEM}}\boldsymbol{\psi}^{(n)}. \tag{4.31}$$

The advantages of finite element (FE) discretization are the adaptation of the element mesh to the problem geometry and the spatial control of the solution accuracy. In addition, since the system matrices $\mathbf{H}_{\mathrm{TI}}^{\mathrm{FEM}}$ and $\mathbf{S}^{\mathrm{FEM}}$ are extremely sparse, the eigenvalue problem can be solved efficiently with Krylov-subspace methods [313, 314].

4.3.2 Time-evolution

In contrast to TISE as an eigenvalue problem, TDSE is an *initial value* problem: We must compute the time-evolution of the state $\left|\psi(t)\right\rangle$ given an initial value $\left|\psi(0)\right\rangle$ and the equation of motion,

$$-\mathrm{i}\partial_t \left|\psi(t)\right\rangle = \hat{H}_{\mathrm{TD}}(t)\left|\psi(t)\right\rangle, \tag{4.32}$$

where $\hat{H}_{\mathrm{TD}}$ is the time-dependent Hamiltonian.

The numerical solution of TDSE proceeds as follows. First, we discretize the coordinate/state-space of the problem similarly as for TISE, and select an initial state $\left|\psi(0)\right\rangle$. The initial state is often chosen as one of the eigenstates of the time-independent Hamiltonian, but in principle it can be any state.

After the spatial discretization, TDSE reduces to a system of coupled ODEs,

$$-\mathrm{i}\mathbf{S}\frac{\mathrm{d}}{\mathrm{d}t}\boldsymbol{\psi}(t) = \mathbf{H}_{\mathrm{TD}}(t)\boldsymbol{\psi}(t), \tag{4.33}$$

where $\boldsymbol{\psi}(t)$ is the time-evolving vector of our expansion coefficients and $\mathbf{H}_{\mathrm{TD}}(t)$ the discretized time-dependent Hamiltonian operator. In the FD discretization, the overlap matrix $\mathbf{S}$ is an identity matrix.

Equation (4.33) can be solved with numerous different methods. First, standard solvers for ODEs are applicable, such as the RK methods introduced in Sec. 4.2.4. Standard solvers, however, do not usually take into account additional properties of the Schrödinger equation such as norm conservation. Hence, specialized solvers are usually preferred.

Luckily, Eq. (4.33) has a formal solution [316]

$$\boldsymbol{\psi}(t) = \mathcal{T}\left\{ e^{-\mathrm{i}\mathbf{S}^{-1}\int_{t_0}^{t}\mathbf{H}_{\mathrm{TD}}(t')\,\mathrm{d}t'} \right\}\psi(t_0), \tag{4.34}$$

where $\mathcal{T}$ is the *chronological time ordering operator* [316]. For a short time span $[t_0, t_0 + \Delta t]$, where the commutator $[\mathbf{H}_{\mathrm{TD}}(t), \mathbf{H}_{\mathrm{TD}}(t')]$ $\forall t, t' \in [t_0, t_0 + \Delta t]$ (almost) vanishes, we can approximate the time-evolution in Eq. (4.34) with the exponential mid-point rule [317]

$$\boldsymbol{\psi}(t_0 + \Delta t) = e^{-\mathrm{i}\mathbf{S}^{-1}\mathbf{H}_{\mathrm{TD}}\left(t_0+\frac{\Delta t}{2}\right)\Delta t}\boldsymbol{\psi}(t_0), \tag{4.35}$$

where we only need to compute a regular matrix-exponential – or rather its action on a vector $\boldsymbol{\psi}(t_0)$. The full matrix exponential could be computed, e.g., using Padé approximants [318], but its action on $\boldsymbol{\psi}(t_0)$ can be obtained with, e.g., Krylov-subspace methods [319].

The exponential mid-point rule has the advantage that the exponential propagator is a unitary transformation, thus conserving the wave function norm [317]. Furthermore, it is time-reversible [317], and thus especially suitable for quantum optimal control theory (QOCT) simulations when we may need to propagate backwards in time (see Sec. 3.1).

Further approximations to the exponential mid-point rule include, e.g., the Crank-Nicolson (CN) method [320]. The CN propagator starts with the time-reversibility condition,

$$e^{-\mathrm{i}\mathbf{S}^{-1}\mathbf{H}_{\mathrm{TD}}\left(t_0+\frac{\Delta t}{2}\right)\frac{\Delta t}{2}}\boldsymbol{\psi}(t_0) = e^{\mathrm{i}\mathbf{S}^{-1}\mathbf{H}_{\mathrm{TD}}\left(t_0+\frac{\Delta t}{2}\right)\frac{\Delta t}{2}}\boldsymbol{\psi}(t_0 + \Delta t), \tag{4.36}$$

and expands the matrix exponentials to first order in $\mathbf{S}^{-1}\mathbf{H}_{\mathrm{TD}}$, yielding

$$\boldsymbol{\psi}(t_0+\Delta t) = \left[\mathbf{S} + \frac{\mathrm{i}\Delta t}{2}\mathbf{H}_{\mathrm{TD}}\left(t_0 + \frac{\Delta t}{2}\right)\right]^{-1}\left[\mathbf{S} - \frac{\mathrm{i}\Delta t}{2}\mathbf{H}_{\mathrm{TD}}\left(t_0 + \frac{\Delta t}{2}\right)\right]\boldsymbol{\psi}(t_0). \tag{4.37}$$

The CN method is also a unitary transformation [320], thus conserving the wave function norm in numerical simulations.

4.4 Optimization methods

4.4.1 Overview

An optimization problem corresponds to finding the minimum (or maximum) of a real-valued function.[3] Formally, this can be written as [265, 321]

$$\begin{aligned} &\text{minimize } F(\mathbf{x}),\ \mathbf{x} \in \mathbb{R}^n \\ &\text{subject to } c_i(\mathbf{x}) \geq 0,\ i = 0, 1, \ldots, m-1, \end{aligned} \tag{4.38}$$

where $F : \mathbb{R}^n \to \mathbb{R}$ is the *target* function and $c_i : \mathbb{R}^n \to \mathbb{R}$ are the *constraint* functions. In quantum control problems, the search space parameters $\mathbf{x}$ are the control knobs for the laser pulse, and the target F is an observable computed from TDSE simulations.

Multiple methods have been developed for solving these optimization problems. The simplest case of having a linear target and linear constraint functions can be solved with, e.g., the simplex algorithm [322]. For nonlinear functions such as those common in quantum control, the optimization algorithms can be classified either as derivative-free or gradient-based, depending on whether the knowledge of the gradient of the target is required.

4.4.2 Derivative-free optimization with trust-region methods

Derivative-free optimization is based on sampling the target and the constraints at multiple locations in the search space. There are various types of derivative-free optimization methods, but we focus on *trust region methods* which run an iterative search for the minimum of F by leveraging easier-to-handle *surrogate models*. In the following, we discuss three different algorithms, Constrained Optimization BY Linear Approximation (COBYLA) [321], NEW Unconstrained Optimization with quadratic Approximation (NEWUOA) [323], and Bound Optimization BY Quadratic Approximation (BOBYQA) [324], which are used later in this compendium.

Trust-region methods work by building a surrogate model $\hat{F} : \mathbb{R}^n \to \mathbb{R}$ for the target [325]. The surrogate is built on samples of the true target function F

[3] Or functional, if the search space is large.

and it comes with a *trust-region* $B \subset \mathbb{R}^n$ within which the surrogate model is expected to give a decent approximation to the target function F [325]. The trust-region is often taken as a n-sphere $B(\mathbf{x}_{\text{opt}}, \Delta)$ with radius Δ, centered on the optimal point $\mathbf{x}_{\text{opt}}$ from previous iterations [325].

The trust-region optimization proceeds iteratively by (i) minimizing the surrogate problem

$$\text{minimize } \hat{F}(\mathbf{x}),\ \mathbf{x} \in B(\mathbf{x}_{\text{opt}}, \Delta) \subset \mathbb{R}^n, \tag{4.39}$$

(ii) updating the surrogate model $\hat{F}$ by replacing old points with a new one from the surrogate optimization, and (iii) by adjusting the trust-region radius Δ if the surrogate model performs significantly worse or better than expected [325].

COBYLA is a trust region method utilizing *linear* surrogate models for both the target F and the constraints c_i [321]. It starts by constructing an n-simplex $\left\{\mathbf{x}^{(0)}, \ldots, \mathbf{x}^{(n)}\right\}$ from an initial guess and an initial trust region radius [321]. The surrogates $\hat{F}$ and $\hat{c}_i$ become linear interpolants based on the simplex. The simplex is updated by alternating between optimizing the constrained surrogate model within the trust region, refining the simplex to increase accuracy of the surrogate model or to prevent the simplex from collapsing, and decreasing the trust region radius and adjusting the interpolating surrogate model [321]. COBYLA converges when the trust region radius decreases below a predefined tolerance value [321].

NEWUOA is designed for unconstrained optimization, and it is based on *quadratic* surrogate models [323]. The advantage of NEWUOA is the fact that it does not require a full set of samples for building the quadratic model [323]. This significantly reduces the computational cost [323]. The idea is to use only $m \ll \frac{1}{2}(n+1)(n+2)$ samples[4] of the target F for building the quadratic surrogate model $\hat{F}$ [323]. The remaining degrees of freedom in the surrogate are handled by minimizing the change in the *curvature* of the quadratic model between updates to the surrogate [323]. NEWUOA also has a more recent sibling, BOBYQA, which uses the same idea for building and updating the quadratic surrogate model [324, 326]. However, BOBYQA allows for optimization inside a hypercube, instead of an unconstrained domain [324], and it also includes some tweaks for numerical stability and improving convergence [324, 326].

[4] Often $m = 2n + 1$ is a good choice [323].

4.4.3 Gradient-based optimization

As described above, the trust-region methods build their surrogate models by sampling only the target function F. More efficient optimization methods can be developed by utilizing also the gradient ∇F. First, let us consider *Newton's method* where the iterative update of the optimal point $\mathbf{x}_k \rightarrow \mathbf{x}_{k+1} = \mathbf{x}_k + \mathbf{\Delta x}_k$ follows from the 2nd order Taylor expansion of the target [327],

$$F(\mathbf{x}_{k+1}) \approx F(\mathbf{x}_k) + \nabla F(\mathbf{x}_k)^T \mathbf{\Delta x}_k + \frac{1}{2} \mathbf{\Delta x}_k^T \mathbf{H}(\mathbf{x}_k) \mathbf{\Delta x}_k, \tag{4.40}$$

where $\mathbf{H}(\mathbf{x})$ is the Hessian of F, $H_{i,j} = \frac{\partial^2 F}{\partial x_i \partial x_j}$. The initial quess $\mathbf{x}_0$ is given as an input for the optimization routine.

Minimizing the above Taylor expansion of F yields the Newton's update formula [327],

$$\mathbf{x}_{k+1} = \mathbf{x}_k - \gamma \mathbf{H}(\mathbf{x})^{-1} \nabla F(\mathbf{x}_k), \tag{4.41}$$

where $\gamma = 1$ in a rigorous setting, but it is often replaced by an estimate for a good step-size [327].

However, the computation of the Hessian $\mathbf{H}$ is often a formidable task, and we rarely have that information available in quantum control simulations. *Quasi-Newton* techniques augment the Newton's method with an update step for an *approximate Hessian* $\mathbf{B}_k \approx \mathbf{H}(\mathbf{x}_k)$ [327]. The approximate Hessian $\mathbf{B}$ is built so that is obeys the *quasi-Newton* condition [327],

$$\nabla F(\mathbf{x}_{k+1}) \approx \nabla F(\mathbf{x}_k) + \mathbf{H}(\mathbf{x}_k) \mathbf{\Delta x}_k \approx \nabla F(\mathbf{x}_k) + \mathbf{B}_{k+1} \mathbf{\Delta x}_k, \tag{4.42}$$

i.e.,

$$\mathbf{B}_{k+1} \mathbf{\Delta x}_k \approx \left[\nabla F(\mathbf{x}_{k+1}) - \nabla F(\mathbf{x}_k) \right]. \tag{4.43}$$

The Broyden-Fletcher-Goldfarb-Shannon (BFGS) algorithm updates the approximate Hessian $\mathbf{B}_k$ with [327–331]

$$\begin{aligned} \mathbf{B}_{k+1} = \mathbf{B}_k &+ \frac{\left[\nabla F(\mathbf{x}_{k+1}) - \nabla F(\mathbf{x}_k) \right] \left[\nabla F(\mathbf{x}_{k+1}) - \nabla F(\mathbf{x}_k) \right]^T}{\left[\nabla F(\mathbf{x}_{k+1}) - \nabla F(\mathbf{x}_k) \right]^T \mathbf{\Delta x}_k} \\ &- \frac{\mathbf{B}_k \mathbf{\Delta x}_k (\mathbf{B}_k \mathbf{\Delta x}_k)^T}{\mathbf{\Delta} x_k^T \mathbf{B}_k \mathbf{\Delta x}_k}, \end{aligned} \tag{4.44}$$

and computes the update step using $\mathbf{B}_k$ [327]

$$\mathbf{x}_{k+1} = \mathbf{x}_k - \gamma_k \mathbf{B}_k^{-1} \nabla F(\mathbf{x}_k), \tag{4.45}$$

where γ_k is the step-size obtained from (an approximate solution to) [327]

$$\underset{\gamma_k > 0}{\operatorname{argmin}} F\left(\mathbf{x}_k - \gamma_k \mathbf{B}_k^{-1} \nabla F(\mathbf{x}_k)\right). \tag{4.46}$$

4.4.4 Global optimization

While the trust region and quasi-Newton algorithms solve a *local* optimization problem, multiple methods exist for finding *global* minima. Evolutionary algorithms update generations of walkers in the search space based on their success [326], Bayesian methods generate global surrogate models [332], and some other methods search the parameter space by dividing it into smaller and smaller hypercubes [326]. In addition, random restarting of local optimization with different initial conditions also provides a way for global search of minima of the target.

Multi-Level Single Linkage (MLSL) is a method that utilizes repeated local optimization, using any local optimizer of your choosing [326]. It provides anti-clustering heuristics for avoiding repeated convergence to the same local optimum [326], hence improving upon mere random restarting of the local optimizer [326]. MLSL is employed in some of the studies in the next chapter, and we refer the reader to Ref. [333] for further details on the algorithm.

4.4.5 Constraints

The topic of this compendium is the optimization of driving laser pulses for controlling various quantum phenomena. As discussed in Sec. 3.2, realistic pulse waveforms are quite restricted, and hence we must also incorporate constraints when optimizing the pulse parameters.

Bounds for individual parameters x_i are the easiest to incorporate. They can be included directly in the optimization algorithm, as in the case of BOBYQA [324], or we can map the constrained optimization problem to an unconstrained one.

Consider, e.g., a 1D optimization problem

$$\text{minimize } F(x),\ x \in [a, b] \subset \mathbb{R}. \tag{4.47}$$

By mapping $\mathbb{R}$ to the search space $[a, b]$ with, e.g.,

$$g : \mathbb{R} \to [a, b], x \mapsto (b - a)\tanh(x) + a, \tag{4.48}$$

the constrained optimization problem has been transformed to an unconstrained problem

$$\text{minimize } F \circ g,\ x \in \mathbb{R}. \tag{4.49}$$

Equality constraints $c_e(x) = 0$ can either be handled by the optimization algorithm (the preferred method), as with COBYLA [321], or they can be included by increasing the search space dimensions with *Lagrange multipliers* [334]. Consider again a 1D optimization problem, but now subject to a nonlinear equality constraint:

$$\begin{aligned} &\text{minimize } F(x),\ x \in \mathbb{R} \\ &\text{subject to } c_e(x) = 0. \end{aligned} \tag{4.50}$$

By introducing an additional variable λ, we can now optimize the unconstrained two-dimensional (2D) problem

$$\text{minimize } F(x) + \lambda c_e(x),\ (x, \lambda) \in \mathbb{R}^2, \tag{4.51}$$

where the stationarity condition in the extra dimension enforces the equality constraint.

Inequality constraints $c_i(x) \geq 0$, on the other hand, can be transformed to equality constraints by the method of *slack variables* [334]. Consider again the 1D optimization problem but subject to a nonlinear inequality constraint:

$$\begin{aligned} &\text{minimize } F(x),\ x \in \mathbb{R} \\ &\text{subject to } c_i(x) \geq 0. \end{aligned} \tag{4.52}$$

By introducing a *slack variable* s, we can transform the above problem to

$$\begin{aligned} &\text{minimize } F(x),\ (x, s) \in \mathbb{R}^2 \\ &\text{subject to } c_i(x) = s^2, \end{aligned} \tag{4.53}$$

which can be handled with Lagrange multipliers yielding a 3D problem

$$\text{minimize } F(x) + \lambda \left[c_i(x) - s^2 \right], \ (x, s, \lambda) \in \mathbb{R}^3. \tag{4.54}$$

As we have discovered above, if the optimization method does not handle our nonlinear constraints, we have to increase the dimension of our search space to enforce them. This is undesirable as it increases the computational cost of the optimization. Let us briefly consider an alternative way to incorporate nonlinear constraints *without* increasing the dimension of the search space. These methods, called **augmented Lagrangian methods**, modify the target function F by adding a *penalty* term built from the constraints [335], e.g.,

$$F \mapsto F_\rho^{\text{aug}}(x, \lambda, \mu) = F(x) + \frac{\rho}{2} \left\{ \left[c_e(x) + \frac{\lambda}{\rho} \right]^2 + \max \left[0, c_i(x) + \frac{\mu}{\rho} \right]^2 \right\}, \tag{4.55}$$

where $F_\rho^{\text{aug}}(x, \lambda, \mu)$ is the augmented target and ρ, λ, μ are the penalty weight, Lagrange multiplier, and slack variable, respectively [335]. The optimization proceeds iteratively by optimizing F_ρ^{aug} with decreasing solution tolerance [335]. After each iterative solution of F_ρ^{aug}, the multipliers λ and μ are modified to better fulfill the constraints and the penalty factor ρ is increased [335]. By incorporating the constraints as iterative update of the target function, augmented Lagrangian methods provide an easy way to include arbitrary nonlinear constraints while using your favorite optimization algorithm. For more details we refer the reader to Refs. [326, 335–337].

5 Results

5.1 Optimal control of high-order harmonic generation

5.1.1 Motivation and goal

Generation of laser pulses in the attosecond regime with wavelengths in the nanometer range is usually accomplished with one of two methods: X-ray free electron lasers (XFELs) [338] or the utilization of strong-field phenomena in noble gases [74].

XFELs offer wide tunability in wavelength and pulse duration [339], and the maximum pulse intensity is several orders of magnitude higher than in devices based on strong-field phenomena in gases. The downside with XFELs is that they are massive and expensive facilities. For example, the European XFEL facility is spread across 19 hectares of land, and its construction costs were over one billion euros with an estimated yearly upkeep of over 100 million euros [340].

As an alternative attosecond X-ray pulse source, we can use high-order harmonic generation (HHG) (see Sec. 2.8). They are tabletop-sized setups [74] with negligible initial and upkeep costs compared to XFELs. However, HHG-based sources suffer from low pulse intensities, and higher frequencies and shorter duration of the resulting attosecond pulses would be beneficial for applications, e.g., by improving the temporal resolution of high-order harmonic (HH) spectroscopy [14, 43–54, 74].

Numerous schemes have been suggested for solving the issues relating to the intensity, the frequency range, and the pulse durations from HHG sources; Refs. [92, 341–345] review some of the recent advances. The solutions fall roughly into three categories: plateau extension, yield increase, or both of them simultaneously. The extension of the HHG plateau to higher energies has been demonstrated by, e.g., using two-color fields [95–97, 102, 346, 347],

chirped pulses [102–106], or by more complex tailoring of the temporal profile of the driving field [93, 94, 107–111]. The yield increase, on the other hand, has been addressed, e.g., by using two-color fields [112–117], chirped fields [100], multi-element target gases [101], and multi-color waveforms [98]. Simultaneous extension of the cutoff and increase of the HH yield has been demonstrated with, e.g., tailored two-color and multicolor fields [97, 99, 119, 120]. Recently, also HHG from solids [28–42, 53, 279, 348–351] and nanostructures[1] [278, 355, 363–367] have been proposed as prominent candidates for the generation of attosecond pulses in tabletop devices.

In Paper I (Ref. [258]) we investigate the applicability of temporally tailored femtosecond driver pulses in addressing the drawbacks of low yield and low cutoff energies generated with HHG in gases. In brief, we employ quantum optimal control theory (QOCT) (see Sec. 3.1) to find optimal pulses to *simultaneously* increase the HHG yield and the maximal photon energy.

5.1.2 Optimization scheme and model

To optimize the HH spectrum, we maximize the target functional

$$G[\mathbf{u}] = \int_{\omega_a}^{\omega_b} \left|\ddot{d}[\mathbf{u}](\omega)\right|^2 \mathrm{d}\omega, \tag{5.1}$$

where $[\omega_a, \omega_b]$ is the frequency range of the emitted radiation to be optimized and $\mathbf{u}$ denotes the optimizable parameters of the driving femtosecond pulse. Ideally, the maxima of this functional will provide simultaneously the increased HH yield and the extension of the cutoff energy of the generated harmonics.

We fix the fluence and duration T of the driving pulse and parametrise it using a frequency representation with frequencies up to a fixed maximum $\omega_{\max}$,

$$\epsilon\left[\mathbf{u} = \{A_1, \ldots, A_{N-1}\}\right](t) = \sum_{k=1}^{k \leq \left\lfloor \frac{\omega_{\max} T}{2\pi} \right\rfloor} \Theta(t)\Theta(t-T) A_k \sin\left(\frac{2\pi k}{T} t\right), \tag{5.2}$$

[1] Note that while *nanostructure-assisted* HHG (cf. *nanostructure-generated* HHG) in noble gases has been studied intensively [352–360], the current understanding is that this phenomenon will yield low intensities [361, 362] and therefore may not be not suitable for applications.

where we have $N = \left\lfloor \frac{\omega_{\max} T}{2\pi} \right\rfloor - 1$ amplitudes A_k to be optimized due to the fixed fluence constraint. This pulse parametrization sets the electric field correctly to zero at the beginning and the end of the pulse, but it lacks the freedom to adjust the relative phase of different frequency components. The optimization is performed with two different algorithms: the gradient-based Broyden-Fletcher-Goldfarb-Shannon (BFGS) and the gradient-free NEW Unconstrained Optimization with quadratic Approximation (NEWUOA) which we have already introduced in Sec. 4.4.[2]

We demonstrate this scheme in **Paper I** by optimizing the HH response of a one-dimensional (1D) hydrogen atom (introduced in Sec. 2.3). Its static potential is given by [168]

$$V(x) = -\frac{1}{\sqrt{x^2 + 1}}, \tag{5.3}$$

and we model the laser-matter interaction in the length gauge (LG) (see Sec. 2.2.1). These simulations were performed with the `Octopus` software package [135, 136], and we provide an example input file for performing the optimization simulations in the online supplementary material of this thesis [143].

We compare our optimization results shown in the following to a readily available reference pulse with the carrier frequency $\omega = 0.0569$ a.u. (≈ 1.548 eV, i.e., 800 nm Ti:sapphire lasers). The duration and the peak intensity of the reference pulse are set to $T = 1104$ a.u. (≈ 26.7 fs) and 6×10^{13} W/cm^2. We also set $\omega = 0.0569$ a.u. as the maximum allowed frequency in the optimized pulses, and they are also constructed to have the same duration and fluence (pulse energy) as our reference pulse.

5.1.3 Optimized driver pulses for HHG

A few select optimized driver pulses and the corresponding HH spectra reported in **Paper I** are shown in Fig. 5.1(a-b) and (c-d), respectively. The targeted energy ranges for the optimization were set to $1.4 \ldots 4$ a.u. ($\approx 40\,\text{eV} \ldots 110\,\text{eV}$) in Fig. 5.1(a),(c) and $1 \ldots 5$ a.u. ($\approx 30\,\text{eV} \ldots 140\,\text{eV}$) in Fig. 5.1(b),(d).

[2]The gradient for the BFGS algorithm is supplied by QOCT (see Sec. 3.1).

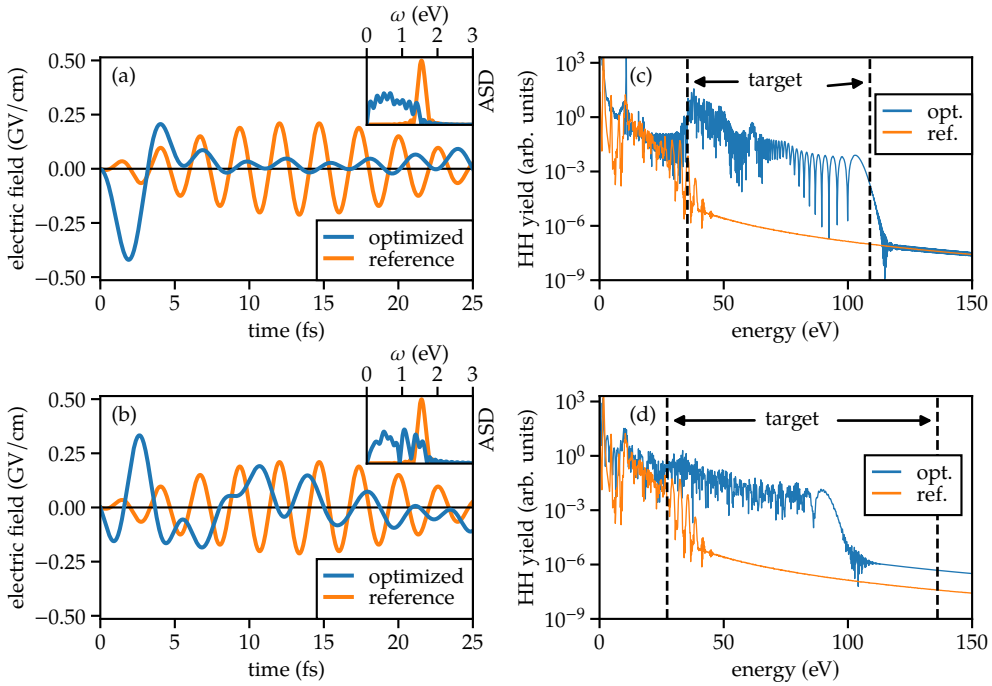

Figure 5.1: (a)-(b) Optimized driver pulses for high-order harmonic generation and (c)-(d) the corresponding single-atom dipole spectra. Adapted from **Paper I**.

The NEWUOA-optimized driver pulse in Fig. 5.1(a) extends the plateau cutoff and increases the HHG yield to perfectly fill the targeted energy range [see Fig. 5.1(b)]. The pulse is composed of a high intensity peak in the beginning followed by a low intensity oscillating tail. The high-intensity peak at the beginning of the driver is not alone responsible for the enhanced HHG. Indeed, we found that should the peak be not in the beginning but later in the pulse, it would increase the plateau cutoff only marginally from the reference spectrum, up to $\omega \approx 2.5$ a.u. (≈ 70 eV). In addition, while the low frequency components of the optimized pulse do produce higher cutoff frequencies than with the reference pulse, the low frequency components alone would result in a much lower HH yield. Only optimized and rather complex combinations of these frequency components were found to produce the kinds of multicolor driving pulses that result in the simultaneous extension of the HHG plateau cutoff and the increase of the photon yield.

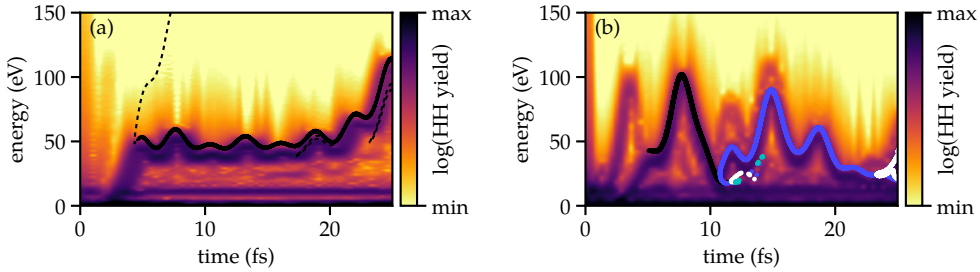

Figure 5.2: Time dependent harmonic spectra corresponding to the optimized driving pulses in Fig. 5.1 (a) and (b). Adapted from **Paper I**.

For the BFGS-optimized driver pulse in Fig. 5.1(c), the target range was slightly increased, up to $\omega = 5\,\text{a.u.}$ ($\approx 140\,\text{eV}$). Despite a more powerful optimization algorithm, we find an almost comparable cutoff extension and yield increase as in the gradient-free case, albeit with different characteristics for the driving pulse. This suggests that given the chosen pulse constraints, the obtained results already represent the maximum enhancement we can achieve for HHG.

5.1.4 Physical origins of the optimized HHG

In **Paper I** we also investigated the physical processes behind the optimized HHG. For this purpose, we have computed (1) the *time-dependent* HH spectra and (2) the return energies in a semiclassical model (see Secs. 2.9 and 4.2) as the electron trajectories return to the origin. These are shown in Fig. 5.2 for the optimized pulses of Fig. 5.1; Here the colored density profile shows the quantum mechanical (QM) time-dependent (TD) HH spectra, and the lines show the return energies in the semiclassical picture.

The return energies of the semiclassical model correspond remarkably well to the quantum harmonic spectra. The highest observed energies in the QM spectra are observed also in the semiclassical model, thus verifying the semiclassical mechanism behind the cutoff extension. The yield increase, on the other hand, can be attributed to the increased tunneling probability due to increased peak strengths of the driving pulses: A comparable yield increase can be obtained with the reference pulses using the same maximum amplitude as in the driving pulses.

5.1.5 Summary

In **Paper I** we set out to find multicolor femtosecond pulses to drive HHG in a way that would increase the yield and plateau cutoff compared to simpler pulsed lasers. We found driver pulse candidates that can *simultaneously* both increase the harmonic yield and extend the cutoff. Furthermore, we have analyzed the physical mechanisms behind the optimized HHG processes and found the yield increase to be due to increased tunneling probability and the cutoff extension due to more complicated electron dynamics that are in good agreement with a semiclassical model. Extension and applicability of the proposed scheme to three-dimensional (3D) setups and phase-matching of the optimized HHG are discussed below in Ch. 6.

5.2 Optimal control of photoelectron emission

5.2.1 Motivation and goal

In addition to HHG, another fundamental phenomenon in intense laser-atom interactions is the ionization and emission of electrons (see Sec. 2.5). While photoelectron emission – especially above-threshold ionization (ATI) – and its control with the driving laser field is interesting in itself from a fundamental point of view [246], photoelectrons can be utilized in self-interrogation spectroscopy of the parent atom, ion, molecule, or nanostructure [55, 368]. For example, laser-induced electron diffraction (LIED) allows simultaneous inquiry of multiple bond-lengths in complex molecules with the temporal resolution of the order of a few femtoseconds [61], and in ultrafast photoelectron holography, the temporal resolution can reach even sub-femtosecond time scales [64]. In both these techniques, the spatial resolution is heavily dependent on the photoelectron energies.

Obtaining higher electron energies and yields is a complicated task since the photo-electron spectrum (PES) is sensitive to multiple laser-parameters. Naturally, higher intensities result in higher electron yields and energies [23]. In addition, since carrier-envelope phase (CEP) has a dramatic effect on the characteristics of ultrashort pulses, it can be used to control both the electron yield and even the symmetry properties of the PES [242–244]. Also, the wavelength dependence of the PES with simple pulses is relatively well known [245].

In **Paper II** (Ref. [259]) we demonstrate the control of the laser-driven photoelectron emission with multicolor waveforms. Specifically, **we aim to increase the maximum photoelectron energy and the signal strength with experimentally feasible pulses**. The proposed scheme is a step towards the control of photoelectron emission for applications such as LIED and ultrafast photoelectron holography.

5.2.2 Optimization scheme and model

Similarly to **Paper I** for HHG, we optimize the target functional

$$G[\mathbf{u}] = \int_{\omega_a}^{\omega_b} S(\omega)\,\mathrm{d}\omega, \tag{5.4}$$

where $[\omega_a, \omega_b]$ is the output frequency range to be optimized, $S(\omega)$ is the PES, and $\mathbf{u}$ denotes the optimizable parameters of the driving multicolor pulse. The PES is computed with the window method introduced in Ref. [191] (see Sec. 2.6), i.e.,

$$\begin{aligned} S(\omega) &= \int_{E_a}^{E_b} \mathrm{d}E\ \mathtt{PES}(E) \\ &= \int_{E_a}^{E_b} \mathrm{d}E\ \frac{\gamma^4}{\left(\hat{H}_0 - E\right)^4 + \gamma^4}, \end{aligned} \tag{5.5}$$

where γ is a half of the energy resolution ($\Delta E\ \approx 0.5\,\mathrm{eV}$ in the present work).

In **Paper II**, we change the laser pulse parametrization from **Paper I** to improve the compatibility with modern waveform synthesizers [84, 369, 370]. The laser electric field is parametrized as a superposition of N channels – ultrashort pulses consisting of a single-frequency carrier wave with a Gaussian envelope. Each channel is parametrized by its own amplitude A_i, carrier frequency ω_i, time of maximal envelope τ_i, carrier-envelope phase (CEP) ϕ_i, and channel full width at half maximum (FWHM) σ_i, i.e.,

$$\epsilon[\mathbf{u}](t) = \sum_{i=1}^{N} A_i \cos\left[\omega_i(t-\tau_i) + \phi_i\right] \exp\left[-\ln(2)\,(t-\tau_i)^2/\sigma_i^2\right]. \tag{5.6}$$

Optimization is performed with the Multi-Level Single Linkage (MLSL) [333] global optimizer on top of the gradient-free Bound Optimization BY Quadratic Approximation (BOBYQA) [324] algorithm. Global pulse constraints such as fluence and peak intensity are enforced with the augmented Lagrangian technique [371, 372]. See Sec. 4.4 for more details on these methods.

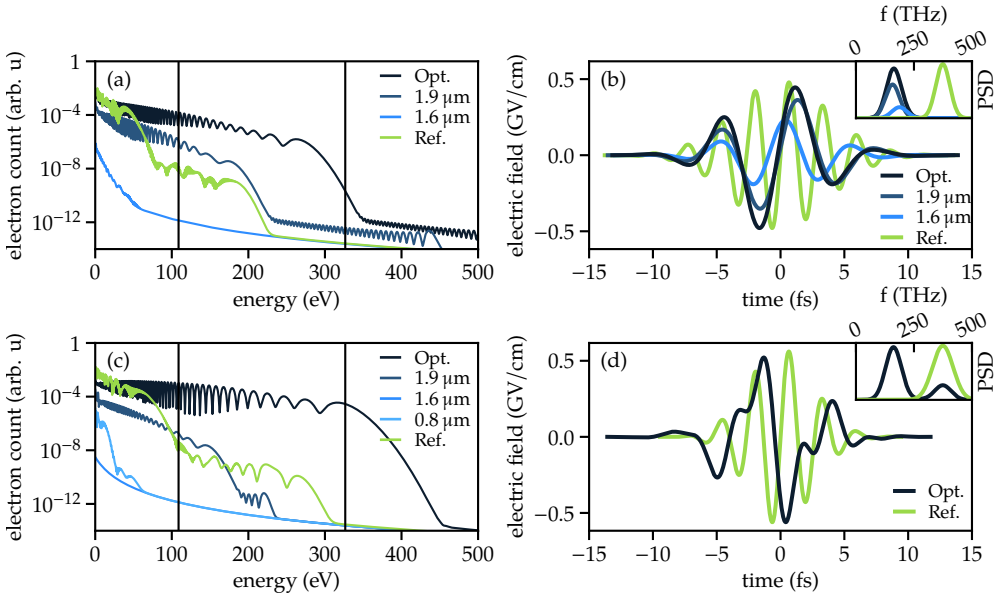

Figure 5.3: (a),(c) Optimized photoelectron spectra together with the component-wise and reference results, and (b),(d) the corresponding driving pulses. Adapted from **Paper II**.

In **Paper II**, the optimization process mixes two to three different channels with fixed central wavelengths 0.8 μm, 1.6 μm, and 1.9 μm. Each channel is restricted by $15.4\,\mathrm{V/nm} \leq A_i \leq 66.8\,\mathrm{V/nm}$, $-9.7\,\mathrm{fs} \leq \tau_i \leq 9.7\,\mathrm{fs}$, and $3.6\,\mathrm{fs} \leq \sigma_i \leq 9.7\,\mathrm{fs}$.

We demonstrate our scheme by optimizing the PES of a 1D hydrogen atom where the electron-laser interaction is modeled in the LG (see Secs. 2.2.1 and 2.3). We compare our results to (i) a readily available 800 nm femtosecond pulse with the same duration and peak intensity as with the optimized pulses and (ii) the spectra with just the individual channels of the optimized driving pulse.

5.2.3 Optimized driver pulses for ATI

First, we consider optimization with just two channels with central wavelengths 1.6 μm and 1.9 μm, and the maximum peak electric field is restricted to below 46.3 V/nm. The resulting optimal pulse is shown as a black line in Fig. 5.3(b)

together with its component channels (dark green and blue lines) and an 800 nm reference pulse of equal duration (light green).

The optimized PES in Fig. 5.3(a) shows dramatic enhancements compared to the spectra of the individual channels of the optimal pulse and the 800 nm reference pulse. First, the yield is increased 3–5 fold when comparing to the pure 1.9 μm channel and the reference pulse. Remarkably, this yield increase is achieved with the same peak amplitude as the reference pulse in contrast to the yield increase mechanism observed for HHG in **Paper I**. Furthermore, the photoelectron cutoff energy is extended by over 100 eV filling the entire targeted energy range.

An optimized driving pulse from a similar setup but with an additional 800 nm channel and a maximum peak electric field constraint of 56.6 V/nm is shown in Fig. 5.3 (d) and the corresponding spectra in Fig. 5.3 (c). Here the yield increase is even more dramatic than in the two-channel case since the photoelectron yield remains almost constant for the whole plateau region of the spectrum. The yield increase is up to *six* orders of magnitude compared to individual channels and the reference pulse, and the cutoff is extended up to 400 eV, i.e., much further than the requested energy window.

Note that here the optimized pulses spread the total pulse energy among the channels. For the optimized two-channel case, the channels are mixed in (intensity) proportions of one to three (1.6 μm : 1.9 μm), and for the three channels in proportions of 5:1:11 (0.8 μm : 1.6 μm : 1.9 μm). This is a desirable effect since it is more difficult to pack high amounts of energy to a single channel than to distribute it among multiple channels. In addition, the optimized driving pulses mix *shorter wavelength* channels to increase the PES cutoff even if these channels alone would result in spectra with much lower cutoff energies.

5.2.4 Physical origins of the optimized ATI

We have found the main process behind the optimized PES to be of semiclassical origin. This situation is similar as for the optimized HHG in **Paper I**, and we can utilize the same semiclassical model for analysis.

We demonstrate the results for the three-channel optimized driving pulse of Fig. 5.3(d). First, the QM electron density in Fig. 5.4 (a) and the semiclassical

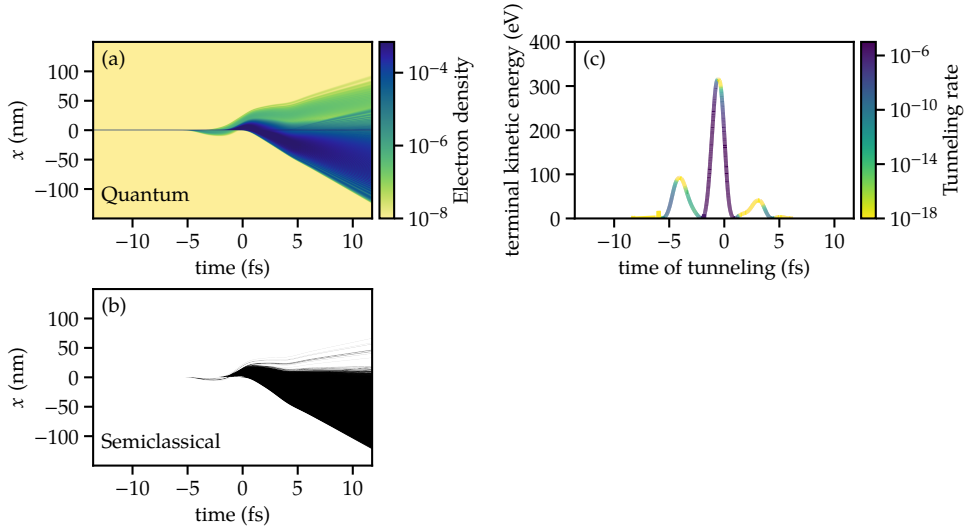

Figure 5.4: (a) Quantum mechanical electron density with the optimized three-color pulse in Fig. 5.3 (d), (b) the corresponding semiclassical trajectories (multiple black lines), and (c) the terminal kinetic energy vs. the time of tunneling in the semiclassical model with line coloring from the tunneling rate. Adapted from **Paper II**.

trajectories in Fig. 5.4 (b) bear a striking resemblance. Indeed, the dynamics of the ionized electron trajectories has a classical origin. The precise optimized mechanism is revealed by comparing the terminal kinetic energy vs. the time of tunneling in Fig. 5.4 (c) to the optimized driving field in Fig. 5.4 (d). After the peak of the electric field before $t = -2$ fs, the tunneling rate is still high enough to generate a significant amount of electron trajectories. In addition, the trajectories tunneling just before the field minimum at $t = 0$ fs feel only the driving action of the later dominant half cycle of the pulse. These trajectories yield the maximal cutoff extension, up to 315 eV in the semiclassical model – in good agreement with the beginning of the cutoff region in the QM spectrum.

5.2.5 Summary

We have demonstrated how the optimal mixing of a *few* pulse channels in the femtosecond range generates laser pulses that can increase the photoelectron yield by up to six orders of magnitude and provide photoelectrons with very

high energies up to 0.5 keV. By distributing the pulse energy among multiple channels, the proposed scheme provides an experimentally feasible technique for controlling the photoelectron emission process without the need of high intensities in single spectral channels. In addition, we have demonstrated how the physical origin of the enhanced photoemission with optimized fields can be understood in a semiclassical picture. Adaptation of the proposed scheme to optimizing attosecond spectroscopy methods is discussed below in Ch. 6.

5.3 Control of Rydberg state populations in alkali metal atoms

5.3.1 Motivation and goal

Rydberg states of atoms and molecules are characterized by long lifetimes [231, 236], mesoscopic extent of the electron wave function [230], and large dipole moments [230] (see also Sec. 2.10). These properties have made them prime candidates for applied quantum information and quantum computing [128].

Conventionally, alkali metal atoms are excited to their Rydberg states using two-photon absorption [133]. The first photon excites the valence electron from an s state to a close by $p_{1/2}$ state, from which the second photon transfers the electron population to a high-n Rydberg state [133, 230]. While this method can achieve good excitation yields [133], it requires (i) tuning of the driving lasers to the resonances between the states – which is not always possible – and (ii) long irradiation durations [133].

In Paper III (Ref. [373]) we investigate the applicability of multichannel femtosecond laser pulses for an ultrafast all-optical preparation of alkali-metal atoms in their Rydberg states. This is a step forward from previous studies with few-color femtosecond control of electron occupation in atoms [374–377].

5.3.2 Optimization scheme and model

As a prototype alkali-metal atom, we consider lithium (Li) in the single active electron (SAE) approximation. An effective atomic potential for the active valence electron in Li is given by [378]

$$V_0(r) = -\frac{1}{r}\left[Z_t + (Z - Z_t)\exp(-a_1 r) + a_2 r \exp(-a_3 r)\right], \tag{5.7}$$

where r is the distance from the atomic nucleus, $Z = 3$ the atomic number, $Z_t = 1$ the number of valence electrons, and $a_1 = 3.395$, $a_2 = 3.212$, and $a_3 = 3.207$ are parameters fitted to experimental results for the eigenenergies [378].

Initially, the SAE is in its ground state ($2s$). The electron interacts with a linearly polarized laser pulse described within the dipole approximation in the velocity

gauge (VG). The Hamiltonian operator of this system is given by (see, e.g., Sec. 2.2.1)

$$\hat{H}_{\mathrm{VG}}(t) = \frac{\hat{\mathbf{p}}^2}{2} + V_{\mathrm{atom}}(\hat{\mathbf{r}}) + A[\mathbf{u}](t) \cdot \hat{p}_z. \tag{5.8}$$

As in **Paper II**, the laser field is described by the vector potential $A[\mathbf{u}](t)$ parameterized as

$$A_z[\mathbf{u}](t) = \sum_{i=1}^{N} \frac{A_i}{\omega_i} \operatorname{env}(t - \tau_i, \sigma_i) \cos\left[\omega_i(t - \tau_i) + \phi_i\right], \tag{5.9}$$

where $\mathbf{u} = \{A_i,\ \omega_i,\ \tau_i,\ \phi_i, \sigma_i\}$ are the amplitude, frequency, time of envelope maximum, carrier-envelope phase, and envelope full width at half maximum (FWHM) of each channel. We define the channel envelopes as

$$\operatorname{env}(t - \tau, \sigma) = \begin{cases} \exp\left[-\frac{\log(2)}{1-\left(\frac{t-\tau}{2\sigma}\right)^2}\left(\frac{t-\tau}{\sigma}\right)^2\right], & |t - \tau| < 2\sigma \\ 0, & \text{otherwise} \end{cases}. \tag{5.10}$$

This resembles a Gaussian function but it goes to zero at twice the FWHM, and it is infinitely differentiable for all $t \in \mathbb{R}$. We designed this pulse parametrization to allow us to efficiently model realistic pulse shapes that are compatible with experimental light field synthesizers [83].

We aim to optimize the population of a certain set $\mathcal{I}$ of Rydberg states $\left|\phi_{n,l}\right\rangle$ at the end of the laser pulse. To this end, we introduce the natural target functional

$$G[\mathbf{u}] = \sum_{\left|\phi_{n,l}\right\rangle \in \mathcal{I}} \left|\left\langle \phi_{n,l} \middle| \psi(T_{\mathrm{max}}) \right\rangle\right|^2, \tag{5.11}$$

where $\mathbf{u}$ is the set of optimizable parameters, and $\left|\psi(T_{\mathrm{max}})\right\rangle$ is the electron state at the end of the laser pulse.

We optimize $G[\mathbf{u}]$ with the global MLSL optimizer combined with the gradient-free local optimization routine Constrained Optimization BY Linear Approximation (COBYLA) (see Sec. 4.4). The optimization process mixes one to six different pulse channels with fixed central wavelengths 0.3 µm, 0.4 µm, 0.700 224 3 µm, 800 µm, 1.6 µm, and 2 µm. Only the 0.7 µm channel is close to the system resonance $2s \rightarrow 2p$. In addition, the channel parameters are

restricted by $A_i \leq 67\,\mathrm{V/nm}$, $|\tau_i| \leq 6\,\mathrm{fs}$, and $2.4\,\mathrm{fs} \leq \sigma \leq 15\,\mathrm{fs}$. The modeling and optimization software is provided in the online supplementary of this thesis; see Ref. [143].

5.3.3 Optimized driver pulses for Rydberg-populations

In **Paper III**, we have investigated the optimized population of states

- 2p,
- 8f,
- 8i,
- $n = 7$, $l = 0 \ldots 2$,
- $n = 7$, $l = 4 \ldots 6$,
- $n = 7 \ldots 10$, $l = 4$, and
- $n = 7 \ldots 10$ (all possible l),

where n is the principal quantum number and l is the azimuthal quantum number, and we label individual target states in the spectroscopic notation. For each of these *targets*, we have optimized all possible channel combinations of the driving field. The maximum target populations and the corresponding channel combinations are shown in Table 5.1, and the best pulse for each target is further visualized in Fig. 5.5.

The target populations vary from 1.7 % for the single target state 8i up to 23 % for a larger set of target states $n = 7 \ldots 10$. The low-lying state 2p can be reached with a short resonance pulse with up to 91 % fidelity[3]. The lack of a decent excitation probability for single state targets (apart from the 2p target) suggests that the scheme lacks the finesse to optimize population transfer to a single select state. Such precise optimization may indeed require the ability to play with the resonances of the system as, e.g., in Refs. [379, 380] – something the modern waveform synthesizers are not designed to do.

[3]Note that since the optimized driving pulse has a finite duration, it has a non-zero bandwidth which activates also other transitions than the dominant 2s→2p. This results in less than 100 % target state population for the 2p target.

Table 5.1: Summary of maximum achieved target populations for different pulse channel combinations. Adopted from **Paper III**.

Target	Channels (μm)	Max. population
2p	0.7	91 %
$n = 7, l = 0 \ldots 2$	0.8, 0.7, 0.4, 0.3	14 %
	0.8, 0.7, 0.4	5 %
$n = 7, l = 4 \ldots 6$	2, 0.8, 0.7, 0.4	6 %
	2, 0.8, 0.4	3 %
$n = 7 \ldots 10, l = 4$	2, 0.7	6 %
$n = 7 \ldots 10$	2, 0.8, 0.7, 0.3	23 %
	2, 1.6, 0.8, 0.7, 0.3	21 %

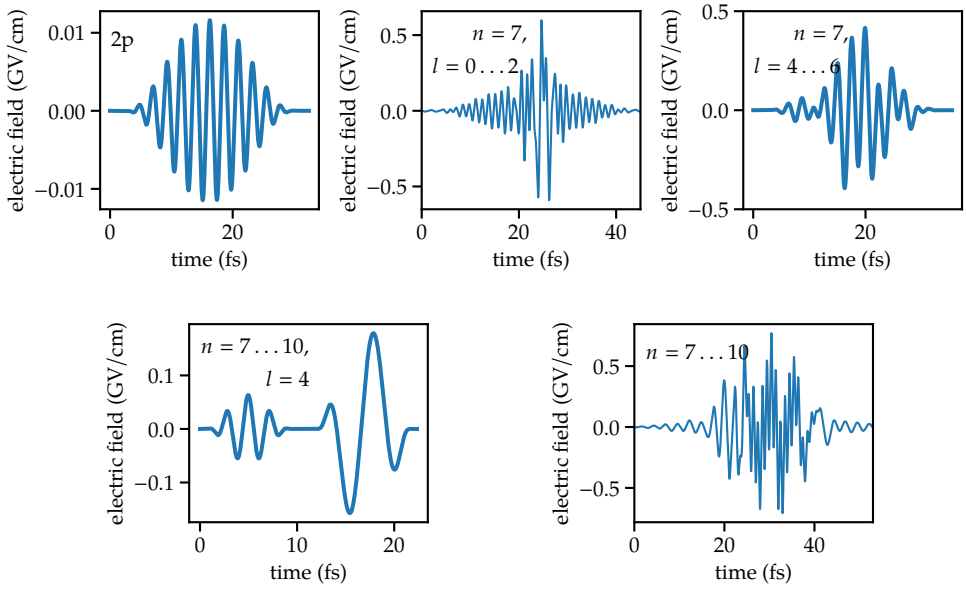

Figure 5.5: Optimized pulses yielding the maximum target occupations at the end of the pulse for each target in Table 5.1. Adapted from **Paper III**.

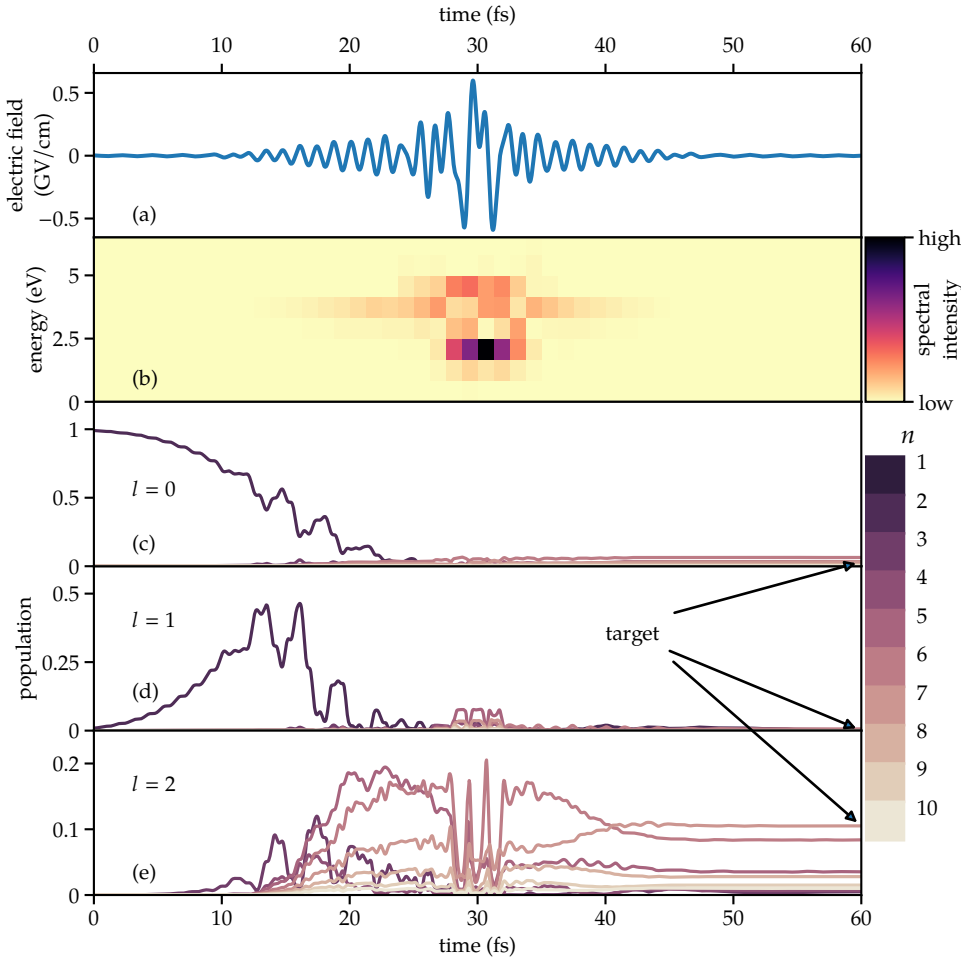

Figure 5.6: (a) Optimized pulse for the target $n = 7$, $l = 0 \ldots 2$, (b) its time-dependent power spectrum , and (c-e) the populations of different eigenstates. Adapted from **Paper III**.

5.3.4 Physical origins of optimized population transfer

The population transfer mechanisms behind the optimized pulses in Fig. 5.5 can be analyzed in multiple ways. Let us consider the target $n = 7$, $l = 0 \ldots 2$ as an illustrative example. For this target our scheme achieves a 14 % final population with the channel combination 800, 700, 400, and 300 nm. The

population dynamics start – as in all the optimal pulses we have found – with a 2s to 2p transition. This is demonstrated in Fig. 5.6. In this example, the initial 2s→2p transition was attributed to the weak 700 nm channel, and without it the target population would drop down to 0.2 %. However, generally speaking, an initial 2s→2p transition with a comparable fidelity can be achieved also without the resonant 700 nm channel. For more information, we refer the reader to **Paper III** and its supplementary online material.

We have found the population transfer mechanisms after the initial 2s→2p transition to be much more complicated. They can be analyzed by, e.g., using instantaneous pairwise transfer rates between the bound states. For the target $n = 7 \ldots 10$, $l = 4$ these pairwise transfer rates reveal relatively simple excitation paths, as we have analyzed further in **Paper III**. However, even the pairwise transfer rates do not provide much deeper insight in most of the optimized pulses but rather paint a picture of a complex population transfer processes, whose common core mechanisms are not easily understood.

5.3.5 Summary

In **Paper III** we have investigated the applicability of few-color femtosecond waveform synthesis for optimal control of exciting lithium – or more generally alkali metal – atoms from their ground state to a set of Rydberg states. Our proposed control and pulse shaping scheme was found to yield up to 23 % target populations for a few selected states, but the scheme lacks the finesse to target any individual state. Modifications to the proposed optimization scheme for increased efficiency are discussed below in Ch. 6.

We have demonstrated how the optimized population transfer processes can be analyzed by investigating the populations of individual states and instantaneous pair-wise transfer rates. The optimized processes deliver a much more complex picture of the system dynamics compared to the traditional two-step excitation process or optimal control schemes with access to system resonances.

5.4 `Fiend` – Finite Element Quantum Dynamics

5.4.1 Motivation and goal

During the last decade, ultrafast strong-field and attosecond communities have focused their attention to laser-driven phenomena in nanostructures and nanostructure-enhanced gaseous media. Nanostructures shape the driving laser electric field by plasmonic and geometric effects, giving birth to high field gradients and amplitude enhancement [381]. This results in a wide variety of strong field phenomena that differ from their atomic counterparts. Recent studies have addressed, e.g., HHG and ATI from nanostructure-enhanced gases [382–384], and electron emission from nanostructures such as tips [123, 125, 385–392] and rods [393–397].

Electromagnetic (EM) fields around a nanostructure are highly inhomogeneous [398], and they cannot be described by the typical dipole approximation Hamiltonian. Hence, many of the currently available high-performance software for the simulation of ultrafast strong-field physics in atoms and molecules are not applicable to these systems. Indeed, **efficient and accurate simulation of laser-matter interaction in nanostructures and nanostructure-enhanced gases requires specialized time-dependent Schrödinger equation (TDSE)-solvers.**

In Paper IV, we have developed a TDSE solver for nanostructures and nanodevices. The software, `FIEND`, is based on finite element (FE) discretization of the Schrödinger equation introduced in Sec. 4.3. `FIEND` has been written in `Python 3.6`, and it utilizes well-tested state-of-the-art numerical libraries. For implementation details, we refer the reader to **Paper IV** and the project website at https://gitlab.com/solanpaa/fiend.

5.4.2 Applicable systems and implementation

`Fiend` is designed for the simulation of SAE systems in cylindrically symmetric potentials. The Hamiltonian of these systems can be written as

$$\hat{H} = \hat{T_\rho} + \frac{\hat{p}_z^2}{2} + V(\hat{\rho}, \hat{z}) + W(\hat{\rho}, \hat{z}, \hat{p}_\rho, \hat{p}_z, t), \tag{5.12}$$

where $\hat{W}$ is the laser-electron interaction operator. All cylindrically symmetric interaction operators are supported, and we have implemented the following commonly used forms: the dipole approximation with the laser vector potential $\mathbf{A} = f(t)\mathbf{e}_z$ in the LG

$$W_{\mathrm{LG}} = -\frac{\partial f(t)}{\partial t}\hat{z}, \tag{5.13}$$

and in the VG

$$W_{\mathrm{VG}} = f(t)\hat{p}_z, \tag{5.14}$$

and for the quasistatic approximation beyond dipole terms we provide the interaction operator

$$\begin{aligned} W_{\mathrm{inhomogeneous}} = &\frac{1}{2}f(t)\mathbf{A}_s \cdot \mathbf{p} + \frac{1}{2}f(t)\mathbf{p} \cdot \mathbf{A}_s \\ &+ \frac{1}{2}f(t)^2\|\mathbf{A}_s(\hat{\rho}, \hat{z})\|^2. \end{aligned} \tag{5.15}$$

5.4.3 Example applications

5.4.3.1 High-harmonic generation

In **Paper I** we optimized the HH response of a 1D hydrogen atom. Extending the optimization study to a 3D model atom would require us to describe the system in a large simulation domain due to a long excursion of the electron wave function as demonstrated for 1D in **Paper I**. `FIEND` provides an efficient way to simulate these systems since the spatial accuracy of the simulation can be position-dependent.

As an example and for validating the software, we compute the HH response of a 3D hydrogen atom interacting with a laser pulse with carrier frequency corresponding to 800 nm, intensity FWHM 4.8 fs, and electric field peak intensity 36 GV/m. The interaction is modeled within the dipole approximation in the VG and the computation mesh is set to high accuracy at the origin and it gradually sparsens for larger radii up to the simulation domain radius of 42 nm. Our computation results in Fig. 5.7 show a typical HHG spectrum from a femtosecond laser pulse. The computed HH response ends with a cut-off beginning at ~ 48 eV in a good agreement with the three-step model's prediction ~ 45 eV [200, 215].

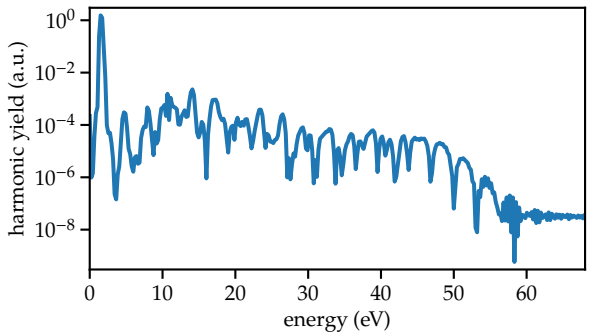

Figure 5.7: High harmonic spectrum of a hydrogen atom under a few-cycle 800 nm femtosecond laser pulse. Adapted from **Paper IV**.

5.4.3.2 Metal nanotips and inhomogeneous fields

Strong-field phenomena at metal nanotips have recently attracted attention due to their ability to shape and strengthen EM fields at the tip apex via plasmonic effects (see, e.g., Refs. [123, 125, 385–392]). In **Paper IV** we demonstrate `Fiend`'s capabilities by computing single-electron dynamics of such metal nanotapers using the correct form [Eq. (5.15)] of the interaction operator for the *inhomogeneous* laser field.

The first step is to compute the plasmon-enhanced near field. In **Paper IV** we consider a gold nanotip with apex radius 7 nm and full opening angle of 20 ° demonstrated in Fig. 5.8(a). Figure 5.8(b) shows the resulting spatial distribution $\|\mathbf{A}_s(\rho, z)\|$. The field strength is maximized at the tip apex and it decays rapidly with distance to the tip. Remarkably, this quasistatic model correctly yields the experimental field-enhancement factor $f \approx 10$ [121].

For quantum dynamics, we prepare the electron in a Gaussian wave packet [Fig. 5.8(c)]. It interacts with a femtosecond infrared (IR) pulse[4]. The evolution of the electron density is demonstrated in Figs. 5.8(c)-(f), where as expected, the electron emission is concentrated at the tip apex where the field enhancement is at its highest. At the end of the simulation, only ~2 % of the electron density has been absorbed by the boundary.

[4]See **Paper IV** for the laser parameters.

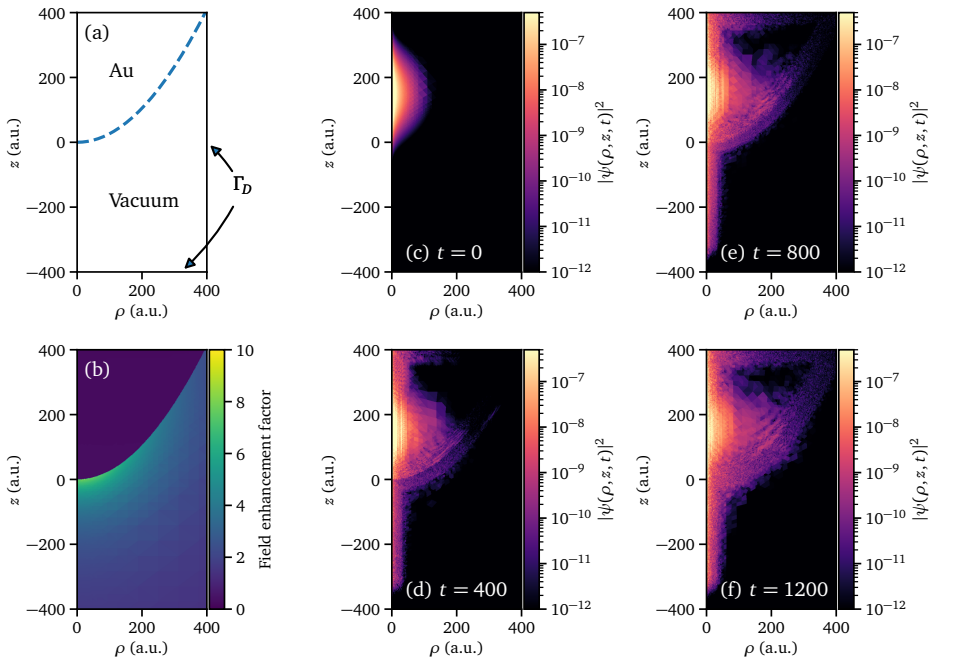

Figure 5.8: (a) Setup of the nanotip geometry where we have a sharp boundary between the gold nanotip and vacuum. (b) Computed spatial enhancement profile of the electric near field in a quasistatic approximation. (c)-(f) Snapshots of the electron density during time evolution. Adapted from **Paper IV**.

5.4.4 Summary

In **Paper IV** we introduced `Fiend` – a finite element method (FEM) simulation suite for quantum dynamics of cylindrically symmetric nanostructures. `Fiend` targets a gap in the existing set of QM simulation codes: simulation of the quantum dynamics of nanodevices *with* the correct laser-matter interaction operator for inhomogeneous EM fields. We demonstrated the use of the software by simulating HHG in a 3D hydrogen atom and photoemission from an ultra sharp gold nanotip.

6 Conclusions

In this thesis we have investigated the applicability of tailored femtosecond laser pulses for the control and optimization of strong-field processes in the attosecond time scale. In **Paper I** we investigated optimal control of high-order harmonic generation (HHG) – an ultrafast strong-field process where the driving laser field induces nonlinear emission of high-energy radiation from individual atoms in the target gas. In HHG, the strength of total emitted field accumulates coherently as the driving field and the emitted field propagate through the gas, known as phase-matching. Our optimization scheme was shown to increase the efficiency of the single-atom high-order harmonic (HH) response in a one-dimensional (1D) model with tailored femtosecond laser pulses. The proposed scheme simultaneously increases HH yield and the maximum output frequency for a fixed input energy. The enhanced HHG was explained in terms of a semiclassical three-step model.

Similar optimization schemes for HHG have later been adopted by other groups in, e.g., Refs. [97, 120, 399]. The scheme has been shown to provide increased HH energies also in three-dimensional (3D) models [97, 399], and the single-atom optimized HHG can also be coherently phase-matched in the medium [120, 281]. However, a more complete model of the setup should be adopted for the ultimate optimization of HHG in gas-jet devices. Accurate modeling of the single-atom response via time-dependent Schrödinger equation (TDSE) in contrast to approximate models is important especially for capturing the emitted HH yield correctly [400]. In addition, even many-body effects may need to be included in the single-atom response [401]. Finally, while phase-matching of single-atom optimized HHG can be achieved retroactively as in Refs. [120, 281], one might improve results by optimizing the macroscopic HH response instead of only the single-atom response.

In **Paper II** we demonstrated optimal control of above-threshold ionization (ATI) by driving it with tailored femtosecond laser pulses that can be generated in modern waveform synthesizers. Our optimization scheme was shown to

simultaneously increase the yield of the photoelectron signal as well as the maximum electron energies in a 1D model atom. These optimizations of the photo-electron spectrum (PES) were explained in terms of a semiclassical model, similarly to the optimized HHG in **Paper I**. With the studied waveform synthesizer setup, our scheme yields electron energies in the 0.5 keV range, and with further tweaking of the laser parameters this could be extended even to the keV range.

Our optimization/control scheme for the PES as well as those in, e.g., Refs. [246, 402], already demonstrate the controllability of the ATI process. However, the proposed schemes are still one step away from optimizing self-interrogation spectroscopy methods. For laser-induced electron diffraction (LIED) and HH spectroscopy, the optimization target should encode not the terminal velocity, but rather the high-energy rescattering or recombination events (see, e.g., Refs. [51, 52, 61, 63, 403, 404]), preferably weighted with the interaction duration for optimizing also the temporal resolution. For electron holography, our scheme should be extended to optimize not only the total PES but individually the direct and the rescattering components to be able to use their interference pattern as a structural probe for the parent ion or molecule [64, 70, 71, 405, 406].

In **Paper III** we developed an optimization scheme for ultrafast excitation of alkali metals in their Rydberg states with waveform-synthesized femtosecond laser pulses. The optimized excitation processes decrease the initialization times for Rydberg-state qubits by several orders of magnitude, but in its current form our scheme lacks the finesse to target individual states and provides too low fidelities. However, we expect these issues to be addressable with, e.g., more freedom in the temporal profile of the laser pulse or using slightly longer tailored pulses available from, e.g., spectral synthesizers [407]. In addition, changing the atomic species to rare gas atoms might improve the results due to more prominent frustrated tunneling [175, 408, 409]. Furthermore, we have applied the scheme for targeting low angular momentum states, whereas targeting the population of circular Rydberg states might be more efficient but would require, e.g., the inclusion of a weak magnetic field or optimizing the field polarization (see, e.g., Refs. [410–412]).

In addition to the optimization schemes provided in **papers I – III**, we have developed and released software for the simulation and analysis of optimal control of HHG and ATI in 1D model systems and extended the 3D TDSE solver

`Qprop` with an optimization package for control studies with experimentally feasible tailored femtosecond pulses. The software are freely available in Ref. [143]. However, the emergence of attosecond science in nanoscale devices [278, 351, 413] requires the development of new TDSE solvers for simulating strong-field phenomena in spatially inhomogeneous driving laser fields. We have addressed this issue in **Paper IV**, where we developed `FIEND` – a modern finite element method (FEM) suite for simulating nonlinear light-matter interaction in nanodevices.

Finally, the optimization and control of strong-field phenomena has mainly focused on the optimization of the driving laser field. In gas-jet setups, there are studies optimizing the macroscopic parameters of the target gas (see, e.g., Refs. [414, 415]), but the emergence of nanoscale attosecond science is opening up new avenues. Nanostructures can be shaped almost arbitrarily (see, e.g., Refs. [416, 417]), and it will be feasible to optimize not only the temporal profile of the driving laser field but also its *spatial* profile via the nanostructure shape. This will open up possibilities for, e.g., optimizing nanostructure-enhanced generation of ultrashort attosecond light and electron bursts. Going even further and bringing nanostructure-enhancement to solid-state attosecond phenomena will face the issue of solving the coupled Maxwell-Schrödinger system for interacting electrons. This is a topic of ongoing investigations (see, e.g., Refs. [418–424]). However, the simulation and especially the *optimization* of nanostructure-enhanced strong-field attosecond phenomena in the solid state might even be out of reach with current computing technologies, requiring us to wait till the exascale era [425–429] of supercomputing.

References

[1] See, e.g., A. H. Zewail, *Femtochemistry: Atomic-Scale Dynamics of the Chemical Bond*, J. Phys. Chem. A **104**, 5660 (2000) and the references therein.

[2] See, e.g., H. Ibrahim et al., *Tabletop imaging of structural evolutions in chemical reactions demonstrated for the acetylene cation*, Nat. Commun. **5**, 4422 (2014).

[3] M. Dantus and A. Zewail, *Introduction: Femtochemistry*, Chem. Rev. **104**, 1717 (2004).

[4] See, e.g., R. J. D. Miller, *Femtosecond Crystallography with Ultrabright Electrons and X-rays: Capturing Chemistry in Action*, Science **343**, 1108 (2014).

[5] See, e.g., F. Krausz, *From femtochemistry to attophysics*, Phys. World **14**, 41 (2001).

[6] L. Torlina et al., *Interpreting attoclock measurements of tunnelling times*, Nat. Phys. **11**, 503 (2015).

[7] C. Hofmann, A. S. Landsman, and U. Keller, *Attoclock revisited on quantum tunneling time*, in IEEE Photonics Conf. (IPC) (2017), pp. 449–450.

[8] N. Camus et al., *Experimental Evidence for Quantum Tunneling Time*, Phys. Rev. Lett. **119**, 023201 (2017).

[9] T. Zimmermann, S. Mishra, B. R. Doran, D. F. Gordon, and A. S. Landsman, *Tunneling Time and Weak Measurement in Strong Field Ionization*, Phys. Rev. Lett. **116**, 233603 (2016).

[10] N. Teeny, E. Yakaboylu, H. Bauke, and C. H. Keitel, *Ionization Time and Exit Momentum in Strong-Field Tunnel Ionization*, Phys. Rev. Lett. **116**, 063003 (2016).

[11] R. Pazourek, S. Nagele, and J. Burgdörfer, *Attosecond chronoscopy of photoemission*, Rev. Mod. Phys. **87**, 765 (2015).

[12] See, e.g., J. Mauritsson, G. Vampa, and C. Vozzi, *Emerging attosecond technologies*, J. Opt. **20**, 110201 (2018) and the references therein.

[13] Z. Chang, P. B. Corkum, and S. R. Leone, *Attosecond optics and technology: progress to date and future prospects*, J. Opt. Soc. Am. B **33**, 1081 (2016).

[14] See, e.g., P. Peng, C. Marceau, and D. M. Villeneuve, *Attosecond imaging of molecules using high harmonic spectroscopy*, Nat. Rev. Phys. **1**, 144 (2019) and the references therein.

[15] P. M. Kraus, M. Zürch, S. K. Cushing, D. M. Neumark, and S. R. Leone, *The ultrafast X-ray spectroscopic revolution in chemical dynamics*, Nat. Rev. Chem. **2**, 82 (2018).

[16] S. R. Leone and D. M. Neumark, *Attosecond science in atomic, molecular, and condensed matter physics*, Faraday Discuss. **194**, 15 (2016).

[17] S. M. Teichmann, F. Silva, S. L. Cousin, M. Hemmer, and J. Biegert, *0.5-keV Soft X-ray attosecond continua*, Nat. Commun. **7**, 11493 (2016).

[18] Y. Pertot et al., *Time-resolved x-ray absorption spectroscopy with a water window high-harmonic source*, Science **355**, 264 (2017).

[19] A. R. Attar et al., *Femtosecond x-ray spectroscopy of an electrocyclic ring-opening reaction*, Science **356**, 54 (2017).

[20] See, e.g., X. Ren et al., *Attosecond light sources in the water window*, J. Opt. **20**, 023001 (2018).

[21] L. Young et al., *Roadmap of ultrafast x-ray atomic and molecular physics*, J. Phys. B **51**, 032003 (2018).

[22] See, e.g., F. Krausz and M. Ivanov, *Attosecond physics*, Rev. Mod. Phys. **81**, 163 (2009) and the references therein.

[23] See, e.g., K. J. Schafer, B. Yang, L. F. DiMauro, and K. C. Kulander, *Above threshold ionization beyond the high harmonic cutoff*, Phys. Rev. Lett. **70**, 1599 (1993).

[24] W. Becker, A. Lohr, and M. Kleber, *Effects of rescattering on above-threshold ionization*, J. Phys. B **27**, L325 (1994).

[25] G. G. Paulus, W. Nicklich, and H. Walther, *Investigation of Above-Threshold Ionization with Femtosecond Pulses: Connection Between Plateau and Angular Distribution of the Photoelectrons*, Europhys. Lett. **27**, 267 (1994).

[26] See, e.g., W. Becker, S. P. Goreslavski, D. B. Milošević, and G. G. Paulus, *The plateau in above-threshold ionization: the keystone of rescattering physics*, J. Phys. B **51**, 162002 (2018) and the references therein.

[27] See, e.g., C. D. Lin, A.-T. Le, C. Jin, and H. Wei, *Attosecond and Strong-Field Physics: Principles and Applications* (Cambridge University Press, 2018).

[28] S. Chatziathanasiou et al., *Generation of Attosecond Light Pulses from Gas and Solid State Media*, Photonics **4** (2017).

[29] H. Kim, S. Han, Y. W. Kim, S. Kim, and S.-W. Kim, *Generation of Coherent Extreme-Ultraviolet Radiation from Bulk Sapphire Crystal*, ACS Photonics **4**, 1627 (2017).

[30] J.-B. Li, X. Zhang, S.-J. Yue, H.-M. Wu, B.-T. Hu, and H.-C. Du, *Enhancement of the second plateau in solid high-order harmonic spectra by the two-color fields*, Opt. Express **25**, 18603 (2017).

[31] H. Liu et al., *Enhanced high-harmonic generation from an all-dielectric metasurface*, Nat. Phys. **14**, 1006 (2018).

[32] T.-Y. Du, D. Tang, X.-H. Huang, and X.-B. Bian, *Multichannel high-order harmonic generation from solids*, Phys. Rev. A **97**, 043413 (2018).

[33] K. Imasaka, T. Kaji, T. Shimura, and S. Ashihara, *Antenna-enhanced high harmonic generation in a wide-bandgap semiconductor ZnO*, Opt. Express **26**, 21364 (2018).

[34] S. Ghimire and D. A. Reis, *High-harmonic generation from solids*, Nat. Phys. **15**, 10 (2019).

[35] S. Gholam-Mirzaei, J. E. Beetar, A. Chacón, and M. Chini, *High-harmonic generation in ZnO driven by self-compressed mid-infrared pulses*, J. Opt. Soc. Am. B **35**, A27 (2018).

[36] H. Liu, Y. Li, Y. S. You, S. Ghimire, T. F. Heinz, and D. A. Reis, *High-harmonic generation from an atomically thin semiconductor*, Nat. Phys. **13**, 262 (2016).

[37] N. Yoshikawa, T. Tamaya, and K. Tanaka, *High-harmonic generation in graphene enhanced by elliptically polarized light excitation*, Science **356**, 736 (2017).

[38] M. Taucer et al., *Nonperturbative harmonic generation in graphene from intense midinfrared pulsed light*, Phys. Rev. B **96**, 195420 (2017).

[39] S. Ghimire, A. D. DiChiara, E. Sistrunk, P. Agostini, L. F. DiMauro, and D. A. Reis, *Observation of high-order harmonic generation in a bulk crystal*, Nat. Phys. **7**, 138 (2010).

[40] S. Jiang, J. Chen, H. Wei, C. Yu, R. Lu, and C. D. Lin, *Role of the Transition Dipole Amplitude and Phase on the Generation of Odd and Even High-Order Harmonics in Crystals*, Phys. Rev. Lett. **120**, 253201 (2018).

[41] S. Gholam-Mirzaei, J. Beetar, and M. Chini, *High harmonic generation in ZnO with a high-power mid-IR OPA*, Appl. Phys. Lett. **110**, 061101 (2017).

[42] G. Vampa et al., *Linking high harmonics from gases and solids*, Nature **522**, 462 (2015).

[43] J. Itatani et al., *Tomographic imaging of molecular orbitals*, Nature **432**, 867 (2004).

[44] H. J. Wörner, H. Niikura, J. B. Bertrand, P. B. Corkum, and D. M. Villeneuve, *Observation of Electronic Structure Minima in High-Harmonic Generation*, Phys. Rev. Lett. **102**, 103901 (2009).

[45] S. Haessler et al., *Attosecond imaging of molecular electronic wavepackets*, Nat. Phys. **6**, Article, 200 (2010).

[46] S. Haessler, J. Caillat, and P. Salières, *Self-probing of molecules with high harmonic generation*, J. Phys. B **44**, 203001 (2011).

[47] P. M. Kraus, A. Rupenyan, and H. J. Wörner, *High-Harmonic Spectroscopy of Oriented OCS Molecules: Emission of Even and Odd Harmonics*, Phys. Rev. Lett. **109**, 233903 (2012).

[48] T. Bredtmann, S. Chelkowski, and A. D. Bandrauk, *Monitoring attosecond dynamics of coherent electron-nuclear wave packets by molecular high-order-harmonic generation*, Phys. Rev. A **84**, 021401 (2011).

[49] H. Niikura, H. J. Wörner, D. M. Villeneuve, and P. B. Corkum, *Probing the Spatial Structure of a Molecular Attosecond Electron Wave Packet Using Shaped Recollision Trajectories*, Phys. Rev. Lett. **107**, 093004 (2011).

[50] H. Soifer et al., *Near-Threshold High-Order Harmonic Spectroscopy with Aligned Molecules*, Phys. Rev. Lett. **105**, 143904 (2010).

[51] H. J. Wörner, J. B. Bertrand, D. V. Kartashov, P. B. Corkum, and D. M. Villeneuve, *Following a chemical reaction using high-harmonic interferometry*, Nature **466**, 604 (2010).

[52] A. D. Shiner et al., *Probing collective multi-electron dynamics in xenon with high-harmonic spectroscopy*, Nat. Phys. **7**, 464 (2011).

[53] T. T. Luu, M. Garg, S. Y. Kruchinin, A. Moulet, M. T. Hassan, and E. Goulielmakis, *Extreme ultraviolet high-harmonic spectroscopy of solids*, Nature **521**, 498 (2015).

[54] D. Baykusheva, M. S. Ahsan, N. Lin, and H. J. Wörner, *Bicircular High-Harmonic Spectroscopy Reveals Dynamical Symmetries of Atoms and Molecules*, Phys. Rev. Lett. **116**, 123001 (2016).

[55] T. Zuo, A. Bandrauk, and P. Corkum, *Laser-induced electron diffraction: a new tool for probing ultrafast molecular dynamics*, Chem. Phys. Lett. **259**, 313 (1996).

[56] M. Meckel et al., *Laser-Induced Electron Tunneling and Diffraction*, Science **320**, 1478 (2008).

[57] C. D. Lin, A.-T. Le, Z. Chen, T. Morishita, and R. Lucchese, *Strong-field rescattering physics—self-imaging of a molecule by its own electrons*, J. Phys. B **43**, 122001 (2010).

[58] J. Xu et al., *Laser-Induced Electron Diffraction for Probing Rare Gas Atoms*, Phys. Rev. Lett. **109**, 233002 (2012).

[59] See, e.g., C. I. Blaga et al., *Imaging ultrafast molecular dynamics with laser-induced electron diffraction*, Nature **483**, 194 (2012).

[60] K.-J. Yuan, H. Lu, and A. D. Bandrauk, *Electron Interference in Molecular Photoionization by Attosecond Laser Pulses*, ChemPhysChem **14**, 1496 (2013).

[61] M. G. Pullen et al., *Imaging an aligned polyatomic molecule with laser-induced electron diffraction*, Nat. Commun. **6**, 7262 (2015).

[62] Y. Ito et al., *Extracting conformational structure information of benzene molecules via laser-induced electron diffraction*, Struct. Dyn. **3**, 034303 (2016).

[63] B. Wolter et al., *Ultrafast electron diffraction imaging of bond breaking in di-ionized acetylene*, Science **354**, 308 (2016).

[64] Y. Huismans et al., *Time-Resolved Holography with Photoelectrons*, Science **331**, 61 (2011).

[65] F. Lépine, M. Y. Ivanov, and M. J. J. Vrakking, *Attosecond molecular dynamics: fact or fiction?*, Nat. Photonics **8**, 195 (2014).

[66] M. Meckel et al., *Signatures of the continuum electron phase in molecular strong-field photoelectron holography*, Nat. Phys. **10**, 594 (2014).

[67] M. Nisoli, P. Decleva, F. Calegari, A. Palacios, and F. Martín, *Attosecond Electron Dynamics in Molecules*, Chem. Rev. **117**, PMID: 28488433, 10760 (2017).

[68] M. Haertelt, X.-B. Bian, M. Spanner, A. Staudte, and P. B. Corkum, *Probing Molecular Dynamics by Laser-Induced Backscattering Holography*, Phys. Rev. Lett. **116**, 133001 (2016).

[69] S. G. Walt et al., *Dynamics of valence-shell electrons and nuclei probed by strong-field holography and rescattering*, Nat. Commun. **8**, Article, 15651 (2017).

[70] M. He, Y. Li, Y. Zhou, M. Li, W. Cao, and P. Lu, *Direct Visualization of Valence Electron Motion Using Strong-Field Photoelectron Holography*, Phys. Rev. Lett. **120**, 133204 (2018).

[71] G. Porat et al., *Attosecond time-resolved photoelectron holography*, Nat. Commun. **9**, 2805 (2018).

[72] H. Rabitz, R. de Vivie-Riedle, M. Motzkus, and K. Kompa, *Whither the Future of Controlling Quantum Phenomena?*, Science **288**, 824 (2000).

[73] X. Xie et al., *Attosecond-Recollision-Controlled Selective Fragmentation of Polyatomic Molecules*, Phys. Rev. Lett. **109**, 243001 (2012).

[74] See, e.g., P. B. Corkum and F. Krausz, *Attosecond science*, Nat. Phys. **3**, 381 (2007) and the references therein.

[75] R. Kienberger, M. Uiberacker, M. F. Kling, and F. Krausz, *Attosecond physics comes of age: from tracing to steering electrons at sub-atomic scales*, J. Mod. Opt. **54**, 1985 (2007).

[76] P. Salières, A. Maquet, S. Haessler, J. Caillat, and R. Taïeb, *Imaging orbitals with attosecond and Ångström resolutions: toward attochemistry?*, Rep. Prog. Phys. **75**, 062401 (2012).

[77] V. Despré, N. V. Golubev, and A. I. Kuleff, *Charge Migration in Propiolic Acid: A Full Quantum Dynamical Study*, Phys. Rev. Lett. **121**, 203002 (2018).

[78] P. M. Kraus et al., *Measurement and laser control of attosecond charge migration in ionized iodoacetylene*, Science **350**, 790 (2015).

[79] C. Arnold, O. Vendrell, R. Welsch, and R. Santra, *Control of Nuclear Dynamics through Conical Intersections and Electronic Coherences*, Phys. Rev. Lett. **120**, 123001 (2018).

[80] E. Lindroth et al., *Challenges and opportunities in attosecond and XFEL science*, Nat. Rev. Phys. **1**, 107 (2019).

[81] M. F. Kling, P. von den Hoff, I. Znakovskaya, and R. de Vivie-Riedle, *(Sub-)femtosecond control of molecular reactions via tailoring the electric field of light*, Phys. Chem. Chem. Phys. **15**, 9448 (2013).

[82] E. Goulielmakis et al., *Attosecond Control and Measurement: Lightwave Electronics*, Science **317**, 769 (2007).

[83] See, e.g., M. T. Hassan et al., *Invited Article: Attosecond photonics: Synthesis and control of light transients*, Rev. Sci. Instrum. **83**, 111301 (2012) and the references therein.

[84] A. Wirth et al., *Synthesized Light Transients*, Science **334**, 195 (2011).

[85] H. Fattahi et al., *Third-generation femtosecond technology*, Optica **1**, 45 (2014).

[86] R. J. Levis, G. M. Menkir, and H. Rabitz, *Selective Bond Dissociation and Rearrangement with Optimally Tailored, Strong-Field Laser Pulses*, Science **292**, 709 (2001).

[87] S. K. Lee, H. B. Schlegel, and W. Li, *Bond-Selective Dissociation of Polyatomic Cations in Mid-Infrared Strong Fields*, J. Phys. Chem. A **117**, PMID: 24099343, 11202 (2013).

[88] A. S. Alnaser et al., *Subfemtosecond steering of hydrocarbon deprotonation through superposition of vibrational modes*, Nat. Commun. **5**, Article, 3800 (2014).

[89] A. du Plessis, C. A. Strydom, H. Uys, and L. R. Botha, *Laser induced and controlled chemical reaction of carbon monoxide and hydrogen*, J. Chem. Phys. **135**, 204303 (2011).

[90] P. Nuernberger, D. Wolpert, H. Weiss, and G. Gerber, *Femtosecond quantum control of molecular bond formation*, Proc. Natl. Acad. Sci. **107**, 10366 (2010).

[91] L. Levin, W. Skomorowski, L. Rybak, R. Kosloff, C. P. Koch, and Z. Amitay, *Coherent Control of Bond Making*, Phys. Rev. Lett. **114**, 233003 (2015).

[92] C. Winterfeldt, C. Spielmann, and G. Gerber, *Colloquium: Optimal control of high-harmonic generation*, Rev. Mod. Phys. **80**, 117 (2008).

[93] M. Wendl, M. Högner, and H. Fattahi, *Theoretical Study: High Harmonic Generation by Light Transients.* Appl. Sci. **8**, 728 (2018).

[94] M. Qin and D. E. Kim, *Stabilization of isolated attosecond pulse by controlling the emission time of high-order harmonics*, J. Phys. Commun. **2**, 035001 (2018).

[95] T. Shao, G. Zhao, B. Wen, and H. Yang, *Theoretical exploration of laser-parameter effects on the generation of an isolated attosecond pulse from two-color high-order harmonic generation*, Phys. Rev. A **82**, 063838 (2010).

[96] Z. Zeng, Y. Cheng, X. Song, R. Li, and Z. Xu, *Generation of an Extreme Ultraviolet Supercontinuum in a Two-Color Laser Field*, Phys. Rev. Lett. **98**, 203901 (2007).

[97] Y. Chou, P.-C. Li, T.-S. Ho, and S.-I. Chu, *Optimal control of high-order harmonics for the generation of an isolated ultrashort attosecond pulse with two-color midinfrared laser fields*, Phys. Rev. A **91**, 063408 (2015).

[98] C. Jin, G. Wang, H. Wei, A.-T. Le, and C. D. Lin, *Waveforms for optimal sub-keV high-order harmonics with synthesized two- or three-colour laser fields*, Nat. Commun. **5**, Article, 4003 (2014).

[99] S. Haessler et al., *Optimization of Quantum Trajectories Driven by Strong-Field Waveforms*, Phys. Rev. X **4**, 021028 (2014).

[100] X. Wang, C. Jin, and C. D. Lin, *Coherent control of high-harmonic generation using waveform-synthesized chirped laser fields*, Phys. Rev. A **90**, 023416 (2014).

[101] E. J. Takahashi, T. Kanai, K. L. Ishikawa, Y. Nabekawa, and K. Midorikawa, *Dramatic Enhancement of High-Order Harmonic Generation*, Phys. Rev. Lett. **99**, 053904 (2007).

[102] D. Peng, M. V. Frolov, L.-W. Pi, and A. F. Starace, *Enhancing high-order harmonic generation by sculpting waveforms with chirp*, Phys. Rev. A **97**, 053414 (2018).

[103] Y. Xiang, Y. Niu, and S. Gong, *Control of the high-order harmonics cutoff through the combination of a chirped laser and static electric field*, Phys. Rev. A **79**, 053419 (2009).

[104] D. G. Lee, J.-H. Kim, K.-H. Hong, and C. H. Nam, *Coherent Control of High-Order Harmonics with Chirped Femtosecond Laser Pulses*, Phys. Rev. Lett. **87**, 243902 (2001).

[105] J. J. Carrera and S.-I. Chu, *Extension of high-order harmonic generation cutoff via coherent control of intense few-cycle chirped laser pulses*, Phys. Rev. A **75**, 033807 (2007).

[106] Neyra, Enrique, Videla, Fabian, Pérez-Hernández, Jose Antonio, Ciappina, Marcelo F., Roso, Luis, and Torchia, Gustavo A., *High-order harmonic generation driven by chirped laser pulses induced by linear and non linear phenomena*, Eur. Phys. J. D **70**, 243 (2016).

[107] E. Räsänen and L. B. Madsen, *Strong-field-ionization suppression by light-field control*, Phys. Rev. A **86**, 033426 (2012).

[108] S. B. P. Radnor, L. E. Chipperfield, P. Kinsler, and G. H. C. New, *Carrier-wave steepened pulses and gradient-gated high-order harmonic generation*, Phys. Rev. A **77**, 033806 (2008).

[109] L. E. Chipperfield, J. S. Robinson, J. W. G. Tisch, and J. P. Marangos, *Ideal Waveform to Generate the Maximum Possible Electron Recollision Energy for Any Given Oscillation Period*, Phys. Rev. Lett. **102**, 063003 (2009).

[110] E. Balogh, B. Bódi, V. Tosa, E. Goulielmakis, K. Varjú, and P. Dombi, *Genetic optimization of attosecond-pulse generation in light-field synthesizers*, Phys. Rev. A **90**, 023855 (2014).

[111] B. Bódi, E. Balogh, V. Tosa, E. Goulielmakis, K. Varjú, and P. Dombi, *Attosecond pulse generation with an optimization loop in a light-field-synthesizer*, Opt. Express **24**, 21957 (2016).

[112] K. L. Ishikawa, *Photoemission and Ionization of He^+ under Simultaneous Irradiation of Fundamental Laser and High-Order Harmonic Pulses*, Phys. Rev. Lett. **91**, 043002 (2003).

[113] A. Fleischer and N. Moiseyev, *Amplification of high-order harmonics using weak perturbative high-frequency radiation*, Phys. Rev. A **77**, 010102 (2008).

[114] I. J. Kim et al., *Highly Efficient High-Harmonic Generation in an Orthogonally Polarized Two-Color Laser Field*, Phys. Rev. Lett. **94**, 243901 (2005).

[115] F. Brizuela et al., *Efficient high-order harmonic generation boosted by below-threshold harmonics*, Sci. Rep. **3** (2013).

[116] E. Mansten, J. M. Dahlström, P. Johnsson, M. Swoboda, A. L'Huillier, and J. Mauritsson, *Spectral shaping of attosecond pulses using two-colour laser fields*, New J. Phys. **10**, 083041 (2008).

[117] J. M. Dahlström, A. L'Huillier, and J. Mauritsson, *Quantum mechanical approach to probing the birth of attosecond pulses using a two-colour field*, J. Phys. B **44**, 095602 (2011).

[118] D.-S. Guo, C. Yu, J. Zhang, J. Gao, Z.-W. Sun, and Z. Sun, *On the cutoff law of laser induced high harmonic spectra*, Front. Phys. **10**, 209 (2015).

[119] C. Serrat, *Intrapulse x-ray parametric amplification in high-order-harmonic generation*, Phys. Rev. A **93**, 063415 (2016).

[120] G.-L. Wang, L.-H. Zhou, S.-F. Zhao, and X.-X. Zhou, *Synthesis of Two-Color Laser Pulses for the Harmonic Cutoff Extension*, Commun. Theor. Phys. **65**, 601 (2016).

[121] C. Ropers, D. R. Solli, C. P. Schulz, C. Lienau, and T. Elsaesser, *Localized Multiphoton Emission of Femtosecond Electron Pulses from Metal Nanotips*, Phys. Rev. Lett. **98**, 043907 (2007).

[122] M. Krüger, M. Schenk, M. Förster, and P. Hommelhoff, *Attosecond physics in photoemission from a metal nanotip*, J. Phys. B **45**, 074006 (2012).

[123] R. Bormann, S. Strauch, S. Schäfer, and C. Ropers, *An ultrafast electron microscope gun driven by two-photon photoemission from a nanotip cathode*, J. Appl. Phys. **118**, 173105 (2015).

[124] M. Förster et al., *Two-Color Coherent Control of Femtosecond Above-Threshold Photoemission from a Tungsten Nanotip*, Phys. Rev. Lett. **117**, 217601 (2016).

[125] B. Piglosiewicz et al., *Carrier-envelope phase effects on the strong-field photoemission of electrons from metallic nanostructures*, Nat. Photonics **8**, 37 (2013).

[126] See, e.g., A. Acín et al., *The quantum technologies roadmap: a European community view*, New J. Phys. **20**, 080201 (2018).

[127] See, e.g., T. D. Ladd, F. Jelezko, R. Laflamme, Y. Nakamura, C. Monroe, and J. L. O'Brien, *Quantum computers*, Nature **464**, 45 (2010) and the references therein.

[128] M. Saffman, T. G. Walker, and K. Mølmer, *Quantum information with Rydberg atoms*, Rev. Mod. Phys. **82**, 2313 (2010).

[129] M. Saffman, *Quantum computing with atomic qubits and Rydberg interactions: progress and challenges*, J. Phys. B **49**, 202001 (2016).

[130] Nobel Media AB, *The Nobel Prize in Physics 2018*, `https://www.nobelprize.org/uploads/2018/10/press-physics2018.pdf` (visited on 02/11/2019).

[131] J. Zhang et al., *Observation of a many-body dynamical phase transition with a 53-qubit quantum simulator*, Nature **551**, 601 (2017).

[132] H. Bernien et al., *Probing many-body dynamics on a 51-atom quantum simulator*, Nature **551**, 579 (2017).

[133] See, e.g., T. A. Johnson et al., *Rabi Oscillations between Ground and Rydberg States with Dipole-Dipole Atomic Interactions*, Phys. Rev. Lett. **100**, 113003 (2008).

[134] D. Bauer and P. Koval, *Qprop: A Schrödinger-solver for intense laser–atom interaction*, Comput. Phys. Commun. **174**, 396 (2006).

[135] M. A. Marques, A. Castro, G. F. Bertsch, and A. Rubio, *octopus: a first-principles tool for excited electron–ion dynamics*, Comput. Phys. Commun. **151**, 60 (2003).

[136] A. Castro et al., *octopus: a tool for the application of time-dependent density functional theory*, Phys. Stat. Sol. (b) **243**, 2465 (2006).

[137] C. Ó. Broin and L. Nikolopoulos, *A GPGPU based program to solve the TDSE in intense laser fields through the finite difference approach*, Comput. Phys. Commun. **185**, 1791 (2014).

[138] B. Schmidt and U. Lorenz, *WavePacket: A Matlab package for numerical quantum dynamics. I: Closed quantum systems and discrete variable representations*, Comput. Phys. Commun. **213**, 223 (2017).

[139] S. Patchkovskii and H. Muller, *Simple, accurate, and efficient implementation of 1-electron atomic time-dependent Schrödinger equation in spherical coordinates*, Comput. Phys. Commun. **199**, 153 (2016).

[140] A. Scrinzi, *Infinite-range exterior complex scaling as a perfect absorber in time-dependent problems*, Phys. Rev. A **81**, 053845 (2010).

[141] L. Tao and A. Scrinzi, *Photo-electron momentum spectra from minimal volumes: the time-dependent surface flux method*, New J. Phys. **14**, 013021 (2012).

[142] X. Guan, C. J. Noble, O. Zatsarinny, K. Bartschat, and B. I. Schneider, *ALTDSE: An Arnoldi–Lanczos program to solve the time-dependent Schrödinger equation*, Comput. Phys. Commun. **180**, 2401 (2009).

[143] J. Solanpää, *Solanpää Dissertation Online Supplementary Material*, (2019) https://dx.doi.org/10.5281/zenodo.2636472.

[144] See, e.g., B. Wolter et al., *Strong-Field Physics with Mid-IR Fields*, Phys. Rev. X **5**, 021034 (2015) and the references therein.

[145] See, e.g., J. Levesque, D. Zeidler, J. P. Marangos, P. B. Corkum, and D. M. Villeneuve, *High Harmonic Generation and the Role of Atomic Orbital Wave Functions*, Phys. Rev. Lett. **98**, 183903 (2007).

[146] D. R. Hartree, *The Wave Mechanics of an Atom with a Non-Coulomb Central Field. Part I. Theory and Methods*, Math. Proc. Camb. Philos. Soc. **24**, 89 (1928).

[147] L. D. Landau and E. M. Lifshitz, *Quantum Mechanics: Non-relativistic Theory*, 3rd ed. (Pergamon, 1981).

[148] C. D. Lin, A.-T. Le, C. Jin, and H. Wei, *Attosecond and Strong-Field Physics: Principles and Applications* (Cambridge University Press, Cambridge, UK, 2018).

[149] T. E. Moe and M. Førre, *Ionization of atomic hydrogen by an intense x-ray laser pulse: An ab initio study of the breakdown of the dipole approximation*, Phys. Rev. A **97**, 013415 (2018).

[150] M. Førre, S. Selstø, J. P. Hansen, and L. B. Madsen, *Exact Nondipole Kramers-Henneberger Form of the Light-Atom Hamiltonian: An Application to Atomic Stabilization and Photoelectron Energy Spectra*, Phys. Rev. Lett. **95**, 043601 (2005).

[151] M. Førre, J. P. Hansen, L. Kocbach, S. Selstø, and L. B. Madsen, *Nondipole Ionization Dynamics of Atoms in Superintense High-Frequency Attosecond Pulses*, Phys. Rev. Lett. **97**, 043601 (2006).

[152] M. Førre, S. Selstø, J. P. Hansen, T. K. Kjeldsen, and L. B. Madsen, *Molecules in intense xuv pulses: Beyond the dipole approximation in linearly and circularly polarized fields*, Phys. Rev. A **76**, 033415 (2007).

[153] M. Førre, *Nondipole ionization dynamics of excited atoms in intense femtosecond pulses*, Phys. Rev. A **74**, 065401 (2006).

[154] D. Dimitrovski, M. Førre, and L. B. Madsen, *Strong-field short-pulse nondipole dynamics*, Phys. Rev. A **80**, 053412 (2009).

[155] M. Førre and A. S. Simonsen, *Nondipole ionization dynamics in atoms induced by intense xuv laser fields*, Phys. Rev. A **90**, 053411 (2014).

[156] A. S. Simonsen and M. Førre, *Magnetic-field-induced enhancement of atomic stabilization in intense high-frequency laser fields*, Phys. Rev. A **92**, 013405 (2015).

[157] M. Førre and A. S. Simonsen, *Generalized velocity-gauge form of the light-matter interaction Hamiltonian beyond the dipole approximation*, Phys. Rev. A **93**, 013423 (2016).

[158] A. S. Simonsen and M. Førre, *Dipole-forbidden atomic transitions induced by superintense x-ray laser fields*, Phys. Rev. A **93**, 063425 (2016).

[159] A. S. Simonsen, T. Kjellsson, M. Førre, E. Lindroth, and S. Selstø, *Ionization dynamics beyond the dipole approximation induced by the pulse envelope*, Phys. Rev. A **93**, 053411 (2016).

[160] T. Kjellsson, M. Førre, A. S. Simonsen, S. Selstø, and E. Lindroth, *Alternative gauge for the description of the light-matter interaction in a relativistic framework*, Phys. Rev. A **96**, 023426 (2017).

[161] T. Kjellsson Lindblom, *Relativistic light-matter interaction*, PhD thesis (Stockholm University, Department of Physics, 2017).

[162] H. Bauke, H. G. Hetzheim, G. R. Mocken, M. Ruf, and C. H. Keitel, *Relativistic ionization characteristics of laser-driven hydrogenlike ions*, Phys. Rev. A **83**, 063414 (2011).

[163] Y. V. Vanne and A. Saenz, *Solution of the time-dependent Dirac equation for multiphoton ionization of highly charged hydrogenlike ions*, Phys. Rev. A **85**, 033411 (2012).

[164] T. Kjellsson, S. Selstø, and E. Lindroth, *Relativistic ionization dynamics for a hydrogen atom exposed to superintense XUV laser pulses*, Phys. Rev. A **95**, 043403 (2017).

[165] F. Grossmann, *Theoretical Femtosecond Physics: Atoms and Molecules in Strong Laser Fields* (Springer-Verlag, Berlin, GE, 2008).

[166] E. Cormier and P. Lambropoulos, *Optimal gauge and gauge invariance in non-perturbative time-dependent calculation of above-threshold ionization*, J. Phys. B: At. Mol. Opt. Phys. **29**, 1667 (1996).

[167] Y.-C. Han and L. B. Madsen, *Comparison between length and velocity gauges in quantum simulations of high-order harmonic generation*, Phys. Rev. A **81**, 063430 (2010).

[168] J. Javanainen, J. H. Eberly, and Q. Su, *Numerical simulations of multiphoton ionization and above-threshold electron spectra*, Phys. Rev. A **38**, 3430 (1988).

[169] W.-C. Liu and C. W. Clark, *Closed-form solutions of the Schrodinger equation for a model one-dimensional hydrogen atom*, J. Phys. B **25**, L517 (1992).

[170] S. Majorosi, M. G. Benedict, and A. Czirják, *Improved one-dimensional model potentials for strong-field simulations*, Phys. Rev. A **98**, 023401 (2018).

[171] A. A. Silaev, M. Y. Ryabikin, and N. V. Vvedenskii, *Strong-field phenomena caused by ultrashort laser pulses: Effective one- and two-dimensional quantum-mechanical descriptions*, Phys. Rev. A **82**, 033416 (2010).

[172] A. Galstyan et al., *Modelling laser-atom interactions in the strong field regime*, Eur. Phys. J. D **71**, 97 (2017).

[173] A. L. Frapiccini, A. Hamido, F. Mota-Furtado, P. F. O'Mahony, and B. Piraux, *Multiresolution schemes for time-scaled propagation of wave packets*, Phys. Rev. A **91**, 043423 (2015).

[174] Y. V. Popov et al., *Separable Potentials Model for Atoms and Molecules in Strong Ultrashort Laser Pulses*, in *Progress in Photon Science: Recent Advances*, edited by K. Yamanouchi, S. Tunik, and V. Makarov (Springer International Publishing, Cham, 2019), pp. 221–242.

[175] B. Piraux, F. Mota-Furtado, P. F. O'Mahony, A. Galstyan, and Y. V. Popov, *Excitation of Rydberg wave packets in the tunneling regime*, Phys. Rev. A **96**, 043403 (2017).

[176] See, e.g., U. De Giovannini, D. Varsano, M. A. L. Marques, H. Appel, E. K. U. Gross, and A. Rubio, *Ab initio angle- and energy-resolved photoelectron spectroscopy with time-dependent density-functional theory*, Phys. Rev. A **85**, 062515 (2012).

[177] See, e.g., S. V. Popruzhenko, *Keldysh theory of strong field ionization: history, applications, difficulties and perspectives*, J. Phys. B **47**, 204001 (2014).

[178] F. H. M. Faisal, *Introduction to Atomic Dynamics in Intense Light Fields*, in *Lectures on Ultrafast Intense Laser Science 1: Volume 1*, edited by K. Yamanouchi (Springer Berlin Heidelberg, Berlin, Heidelberg, 2011), pp. 1–40.

[179] L. V. Keldysh, *IONIZATION IN THE FIELD OF A STRONG ELECTROMAGNETIC WAVE*, J. Exptl. Theoret. Phys. **47**, 1945 (1964).

[180] A. S. Landsman and U. Keller, *Attosecond science and the tunnelling time problem*, Phys. Rep. **547**, 1 (2015).

[181] H. R. Reiss, *Unsuitability of the Keldysh parameter for laser fields*, Phys. Rev. A **82**, 023418 (2010).

[182] H. R. Reiss, *Limits on Tunneling Theories of Strong-Field Ionization*, Phys. Rev. Lett. **101**, 043002 (2008).

[183] H. R. Reiss, *Foundations of Strong-Field Physics*, in *Lectures on Ultrafast Intense Laser Science 1: Volume 1*, edited by K. Yamanouchi (Springer Berlin Heidelberg, Berlin, Heidelberg, 2011), pp. 41–84.

[184] E. E. Serebryannikov and A. M. Zheltikov, *Strong-Field Photoionization as Excited-State Tunneling*, Phys. Rev. Lett. **116**, 123901 (2016).

[185] M. Klaiber and J. S. Briggs, *Crossover from tunneling to multiphoton ionization of atoms*, Phys. Rev. A **94**, 053405 (2016).

[186] M. Lewenstein and A. L'Huillier, *Principles of Single Atom Physics: High-Order Harmonic Generation, Above-Threshold Ionization and Non-Sequential Ionization*, in *Strong Field Laser Physics*, edited by T. Brabec (Springer, New York, USA, 2008), pp. 147–184.

[187] See, e.g., W. Becker, F. Grasbon, R. Kopold, D. Milošević, G. Paulus, and H. Walther, *Above-Threshold Ionization: From Classical Features to Quantum Effects*, in , Vol. 48, edited by B. Bederson and H. Walther, Advances In Atomic, Molecular, and Optical Physics (Academic Press, 2002), pp. 35–98 and the references therein.

[188] B. Yang, K. J. Schafer, B. Walker, K. C. Kulander, P. Agostini, and L. F. DiMauro, *Intensity-dependent scattering rings in high order above-threshold ionization*, Phys. Rev. Lett. **71**, 3770 (1993).

[189] G. G. Paulus, W. Nicklich, H. Xu, P. Lambropoulos, and H. Walther, *Plateau in above threshold ionization spectra*, Phys. Rev. Lett. **72**, 2851 (1994).

[190] See, e.g., F. Catoire and H. Bachau, *Extraction of the absolute value of the photoelectron spectrum probability density by means of the resolvent technique*, Phys. Rev. A **85**, 023422 (2012) and the references therein.

[191] K. J. Schafer and K. C. Kulander, *Energy analysis of time-dependent wave functions: Application to above-threshold ionization*, Phys. Rev. A **42**, 5794 (1990).

[192] J. C. Baggesen and L. B. Madsen, *On the dipole, velocity and acceleration forms in high- order harmonic generation from a single atom or molecule*, J. Phys. B: At. Mol. Opt. Phys. **44**, 115601 (2011).

[193] J. A. Pérez-Hernández and L. Plaja, *Comment on 'On the dipole, velocity and acceleration forms in high-order harmonic generation from a single atom or molecule'*, J. Phys. B **45**, 028001 (2011).

[194] J. Jackson, *Classical Electrodynamics*, 3rd ed. (Wiley India Pvt. Limited, 2007).

[195] K. S. Kunz and R. J. Luebbers, *The Finite Difference Time Domain Method for Electromagnetics* (CRC Press, Florida, USA, 1993).

[196] J. F. Reintjes, *Nonlinear Optical Parametric Processes in Liquids and Gases* (Academic Press, 1984).

[197] D. G. Duffy, *Green's Functions with Applications*, 2nd ed. (CRC Press, FL, USA, 2015).

[198] See, e.g., T. Sato, Y. Orimo, T. Teramura, O. Tugs, and K. L. Ishikawa, *Time-Dependent Complete-Active-Space Self-Consistent-Field Method for Ultrafast Intense Laser Science*, in *Progress in Ultrafast Intense Laser Science XIV*, edited by K. Yamanouchi, P. Martin, M. Sentis, L. Ruxin, and D. Normand (Springer International Publishing, Cham, 2018), pp. 143–171 for more details..

[199] P. B. Corkum, *Plasma perspective on strong field multiphoton ionization*, Phys. Rev. Lett. **71**, 1994 (1993).

[200] J. L. Krause, K. J. Schafer, and K. C. Kulander, *High-order harmonic generation from atoms and ions in the high intensity regime*, Phys. Rev. Lett. **68**, 3535 (1992).

[201] K. Kulander, K. Schafer, and J. Krause, *Dynamics of Short-Pulse Excitation, Ionization and Harmonic Conversion*, in *Super-Intense Laser-Atom Physics*, edited by B. Piraux, A. L'Huillier, and K. Rzążewski (Springer, Boston, USA, 1993), pp. 95–110.

[202] See, e.g., J. J. Sakurai and J. Napolitano, *Modern Quantum Mechanics*, 2nd ed. (Cambridge University Press, Cambridge, UK, 2017) and the references therein.

[203] I. P. Christov, M. M. Murnane, and H. C. Kapteyn, *High-Harmonic Generation of Attosecond Pulses in the "Single-Cycle" Regime*, Phys. Rev. Lett. **78**, 1251 (1997).

[204] G. Sansone, L. Poletto, and M. Nisoli, *High-energy attosecond light sources*, Nat. Photonics **5**, 655 (2011).

[205] P. Saliéres and I. Christov, *Macroscopic Effects in High-Order Harmonic Generation*, in *Strong Field Laser Physics*, edited by T. Brabec (Springer, New York, USA, 2008), pp. 147–184.

[206] See, e.g., C. Trallero-Herrero et al., *Generation of broad XUV continuous high harmonic spectra and isolated attosecond pulses with intense mid-infrared lasers*, J. Phys. B **45**, 011001 (2011).

[207] M. Chini, K. Zhao, and Z. Chang, *The generation, characterization and applications of broadband isolated attosecond pulses*, Nat. Photonics **8**, 178 (2014).

[208] F. Calegari, G. Sansone, S. Stagira, C. Vozzi, and M. Nisoli, *Advances in attosecond science*, J. Phys. B **49**, 062001 (2016).

[209] G. A. Reider, *XUV attosecond pulses: generation and measurement*, J. Phys. D: Appl. Phys. **37**, R37 (2004).

[210] P. Lan, P. Lu, W. Cao, Y. Li, and X. Wang, *Attosecond ionization gating for isolated attosecond electron wave packet and broadband attosecond xuv pulses*, Phys. Rev. A **76**, 051801 (2007).

[211] P. B. Corkum, N. H. Burnett, and M. Y. Ivanov, *Subfemtosecond pulses*, Opt. Lett. **19**, 1870 (1994).

[212] I. J. Sola et al., *Controlling attosecond electron dynamics by phase-stabilized polarization gating*, Nat. Phys. **2**, 319 (2006).

[213] H. Vincenti and F. Quéré, *Attosecond Lighthouses: How To Use Spatiotemporally Coupled Light Fields To Generate Isolated Attosecond Pulses*, Phys. Rev. Lett. **108**, 113904 (2012).

[214] K. T. Kim et al., *Photonic streaking of attosecond pulse trains*, Nat. Photonics **7**, Article, 651 (2013).

[215] M. Lewenstein, P. Balcou, M. Y. Ivanov, A. L'Huillier, and P. B. Corkum, *Theory of high-harmonic generation by low-frequency laser fields*, Phys. Rev. A **49**, 2117 (1994).

[216] M. Ammosov, N. Delone, and V. Krainov, *Tunnel ionization of complex atoms and of atomic ions in an alternating electromagnetic field*, J. Exptl. Theoret. Phys. **91**, 2008 (1986).

[217] N. B. Delone and V. P. Krainov, *Energy and angular electron spectra for the tunnel ionization of atoms by strong low-frequency radiation*, J. Opt. Soc. Am. B **8**, 1207 (1991).

[218] A. M. Perelomov, V. S. Popov, and M. V. Terent'ev, *IONIZATION OF ATOMS IN AN ALTERNATING ELECTRICAL FIELD*, J. Exptl. Theoret. Phys. **50**, 1393 (1965).

[219] A. M. Perelomov and V. S. Popov, *IONIZATION OF ATOMS IN AN ALTERNATING ELECTRICAL FIELD. III*, J. Exptl. Theoret. Phys. **52**, 512 (1967).

[220] See, e.g., H. Reiss, *Foundations of the Strong Field Approximation*, in *Progress in Ultrafast Intense Laser Science III*, edited by K. Yamanouchi, S. L. Chin, P. Agostini, and G. Ferrante (Springer, Berling, Heidelberg, 2008).

[221] N. I. Shvetsov-Shilovski et al., *Semiclassical two-step model for strong-field ionization*, Phys. Rev. A **94**, 013415 (2016).

[222] A. N. Pfeiffer et al., *Attoclock reveals natural coordinates of the laser-induced tunnelling current flow in atoms*, Nat. Phys. **8**, 76 (2011).

[223] N. Camus et al., *Experimental Evidence for Wigner's Tunneling Time*, J. Phys. Conf. Ser. **999**, 012004 (2018).

[224] A. L'Huillier et al., *High-order Harmonic-generation cutoff*, Phys. Rev. A **48**, R3433 (1993).

[225] C.-G. Wahlström et al., *High-order harmonic generation in rare gases with an intense short-pulse laser*, Phys. Rev. A **48**, 4709.

[226] Z. Chang, A. Rundquist, H. Wang, M. M. Murnane, and H. C. Kapteyn, *Generation of Coherent Soft X Rays at 2.7 nm Using High Harmonics*, Phys. Rev. Lett. **79**, 2967 (1997).

[227] M. Busuladžić, A. Gazibegović-Busuladžić, and D. B. Milošević, *High-order above-threshold ionization in a laser field: Influence of the ionization potential on the high-energy cutoff*, Laser Phys. **16**, 289 (2006).

[228] . Milo ševi ć, Hasovi ć, Busulad ži ć, Gazibegovi ć-Busulad ži ć, and W. Becker, *Intensity-dependent enhancements in high-order above-threshold ionization*, Phys. Rev. A **76**, 053410 (2007).

[229] C. Figueira de Morisson Faria, H. Schomerus, and W. Becker, *High-order above-threshold ionization: The uniform approximation and the effect of the binding potential*, Phys. Rev. A **66**, 043413 (2002).

[230] T. F. Gallagher, *Rydberg atoms* (Cambridge University Press, Cambridge, UK, 1994).

[231] See, e.g., C. E. Theodosiou, *Lifetimes of alkali-metal—atom Rydberg states*, Phys. Rev. A **30**, 2881 (1984) and the references therein.

[232] S. V. Andreev, V. I. Mishin, and V. S. Letokhov, *Rydberg levels and ionization potential of francium measured by laser-resonance ionization in a hot cavity*, J. Opt. Soc. Am. B **5**, 2190 (1988).

[233] M. L. Ginter and J. G. Eden, *Rydberg states of the rare gas dimers*, Can. J. Chem. **82**, 762 (2004).

[234] H. .-. Wang, W. S. Felps, and S. P. McGlynn, *Molecular Rydberg states. VII. Water*, J. Chem. Phys. **67**, 2614 (1977).

[235] See, e.g., T. Betts and V. McKoy, *Rydberg States of Diatomic and Polyatomic Molecules Using Model Potentials*, J. Chem. Phys. **54**, 113 (1971).

[236] M. Mack, J. Grimmel, F. Karlewski, L. Sárkány, H. Hattermann, and J. Fortágh, *All-optical measurement of Rydberg-state lifetimes*, Phys. Rev. A **92**, 012517 (2015).

[237] See, e.g., M. Saffman, T. G. Walker, and K. Mølmer, *Quantum information with Rydberg atoms*, Rev. Mod. Phys. **82**, 2313 (2010) and the references therein.

[238] D. Barredo, S. de Léséleuc, V. Lienhard, T. Lahaye, and A. Browaeys, *An atom-by-atom assembler of defect-free arbitrary two-dimensional atomic arrays*, Science **354**, 1021 (2016).

[239] D. Barredo, V. Lienhard, S. de Léséleuc, T. Lahaye, and A. Browaeys, *Synthetic three-dimensional atomic structures assembled atom by atom*, Nature **561**, 79 (2018).

[240] A. Ashkin, *Acceleration and Trapping of Particles by Radiation Pressure*, Phys. Rev. Lett. **24**, 156 (1970).

[241] A. Ashkin, J. M. Dziedzic, J. E. Bjorkholm, and S. Chu, *Observation of a single-beam gradient force optical trap for dielectric particles*, Opt. Lett. **11**, 288 (1986).

[242] G. G. Paulus et al., *Absolute-phase phenomena in photoionization with few-cycle laser pulses*, Nature **414**, 182 (2001).

[243] D. B. Milošević, G. G. Paulus, and W. Becker, *High-order above-threshold ionization with few-cycle pulse: a meter of the absolute phase*, Opt. Express **11**, 1418 (2003).

[244] N. I. Shvetsov-Shilovski, E. Räsänen, G. G. Paulus, and L. B. Madsen, *Asymmetric photoelectron momentum distributions due to quantum interference in strong-field ionization by a few-cycle pulse*, Phys. Rev. A **89**, 043431 (2014).

[245] See, e.g., W. Quan et al., *Classical Aspects in Above-Threshold Ionization with a Midinfrared Strong Laser Field*, Phys. Rev. Lett. **103**, 093001 (2009).

[246] R. E. Goetz, A. Karamatskou, R. Santra, and C. P. Koch, *Quantum optimal control of photoelectron spectra and angular distributions*, Phys. Rev. A **93**, 013413 (2016).

[247] D. Meshulach and Y. Silberberg, *Coherent quantum control of multiphoton transitions by shaped ultrashort optical pulses*, Phys. Rev. A **60**, 1287 (1999).

[248] S. M. Cavaletto, Z. Harman, T. Pfeifer, and C. H. Keitel, *Deterministic strong-field quantum control*, Phys. Rev. A **95**, 043413 (2017).

[249] J. P. Palao, D. M. Reich, and C. P. Koch, *Steering the optimization pathway in the control landscape using constraints*, Phys. Rev. A **88**, 053409 (2013).

[250] D. Meshulach and Y. Silberberg, *Coherent quantum control of two-photon transitions by a femtosecond laser pulse*, Nature **396**, 239 (1998).

[251] J. Werschnik and E. K. U. Gross, *Quantum optimal control theory*, J. Phys. B **40**, R175 (2007).

[252] C. Brif, R. Chakrabarti, and H. Rabitz, *Control of quantum phenomena: past, present and future*, New J. Phys. **12**, 075008 (2010).

[253] J. Zhang, Y.-x. Liu, R.-B. Wu, K. Jacobs, and F. Nori, *Quantum feedback: Theory, experiments, and applications*, Phys. Rep. **679**, 1 (2017).

[254] R. S. Judson and H. Rabitz, *Teaching lasers to control molecules*, Phys. Rev. Lett. **68**, 1500 (1992).

[255] J. J. W. H. Sørensen, M. O. Aranburu, T. Heinzel, and J. F. Sherson, *Quantum optimal control in a chopped basis: Applications in control of Bose-Einstein condensates*, Phys. Rev. A **98**, 022119 (2018).

[256] T. Caneva, T. Calarco, and S. Montangero, *Chopped random-basis quantum optimization*, Phys. Rev. A **84**, 022326 (2011).

[257] P. Doria, T. Calarco, and S. Montangero, *Optimal Control Technique for Many-Body Quantum Dynamics*, Phys. Rev. Lett. **106**, 190501 (2011).

[258] J. Solanpää, J. A. Budagosky, N. I. Shvetsov-Shilovski, A. Castro, A. Rubio, and E. Räsänen, *Optimal control of high-harmonic generation by intense few-cycle pulses*, Phys. Rev. A **90**, 053402 (2014).

[259] J. Solanpää, M. F. Ciappina, and E. Räsänen, *Optimal control of photoelectron emission by realistic waveforms*, J. Mod. Opt. **64**, 1784 (2017).

[260] M. Bukov, A. G. R. Day, D. Sels, P. Weinberg, A. Polkovnikov, and P. Mehta, *Reinforcement Learning in Different Phases of Quantum Control*, Phys. Rev. X **8**, 031086 (2018).

[261] See, e.g., S. J. Glaser et al., *Training Schrödinger's cat: quantum optimal control*, Eur. Phys. J. D **69**, 279 (2015) and the references therein.

[262] A. Castro and E. Gross, *Quantum Optimal Control*, in *Fundamentals of Time-Dependent Density Functional Theory*, edited by M. Marques, N. Maitra, F. Nogueira, E. Gross, and A. Rubio (Springer, Berlin, DE, 2012).

[263] J. M. Geremia, W. Zhu, and H. Rabitz, *Incorporating physical implementation concerns into closed loop quantum control experiments*, J. Chem. Phys. **113**, 10841 (2000).

[264] H. Zhang and H. Rabitz, *Robust optimal control of quantum molecular systems in the presence of disturbances and uncertainties*, Phys. Rev. A **49**, 2241 (1994).

[265] M. J. Powell, *On trust region methods for unconstrained minimization without derivatives*, Mathematical programming **97**, 605 (2003).

[266] K. W. Moore and H. Rabitz, *Exploring quantum control landscapes: Topology, features, and optimization scaling*, Phys. Rev. A **84**, 012109 (2011).

[267] G. Riviello et al., *Searching for quantum optimal controls under severe constraints*, Phys. Rev. A **91**, 043401 (2015).

[268] K. W. Moore and H. Rabitz, *Exploring constrained quantum control landscapes*, J. Chem. Phys. **137**, 134113 (2012).

[269] B. Morschheuser, J. Hamari, and J. Koivisto, *Gamification in Crowdsourcing: A Review*, in the Forty-ninth Hawaii International Conference on System Sciences (HICSS) (2016), pp. 4375–4384.

[270] R. Bonney et al., *Next Steps for Citizen Science*, Science **343**, 1436 (2014).

[271] A. Lieberoth, M. K. Pedersen, A. C. Marin, T. Planke, and J. F. Sherson, *Getting humans to do quantum optimization-user acquisition, engagement and early results from the citizen cyberscience game Quantum Moves*, Human Computation **1** (2014).

[272] J. J. W. H. Sørensen et al., *Exploring the quantum speed limit with computer games*, Nature **532**, 210 (2016).

[273] R. Heck et al., *Remote optimization of an ultracold atoms experiment by experts and citizen scientists*, Proc. Natl. Acad. Sci. **115**, E11231 (2018).

[274] D. Sels, *Stochastic gradient ascent outperforms gamers in the Quantum Moves game*, Phys. Rev. A **97**, 040302 (2018).

[275] H. Fattahi, *Sub-cycle light transients for attosecond, X-ray, four-dimensional imaging*, Contemp. Phys. **57**, 580 (2016).

[276] C. Manzoni et al., *Coherent pulse synthesis: towards sub-cycle optical waveforms*, Laser Photonics Rev. **9**, 129 (2015).

[277] D. E. Rivas et al., *Next Generation Driver for Attosecond and Laser-plasma Physics*, Sci. Rep. **7**, 5224 (2017).

[278] M. F. Ciappina et al., *Attosecond physics at the nanoscale*, Rep. Prog. Phys. **80**, 054401 (2017).

[279] G. Vampa, H. Fattahi, J. Vuckovic, and F. Krausz, *Attosecond nanophotonics*, Nat. Photonics **11**, 210 (2017).

[280] C. Jin and C. D. Lin, *Optimization of multi-color laser waveform for high-order harmonic generation*, Chin. Phys. B **25**, 094213 (2016).

[281] X. Li, J. Fan, J. Ma, G. Wang, and C. Jin, *Application of optimized waveforms for enhancing high-harmonic yields in a three-color laser-field synthesizer*, Opt. Express **27**, 841 (2019).

[282] I. P. Christov, R. Bartels, H. C. Kapteyn, and M. M. Murnane, *Attosecond Time-Scale Intra-atomic Phase Matching of High Harmonic Generation*, Phys. Rev. Lett. **86**, 5458 (2001).

[283] X. Chu and S.-I. Chu, *Optimization of high-order harmonic generation by genetic algorithm and wavelet time-frequency analysis of quantum dipole emission*, Phys. Rev. A **64**, 021403 (2001).

[284] A. Castro, A. Rubio, and E. K. U. Gross, *Enhancing and controlling single-atom high-harmonic generation spectra: a time-dependent density-functional scheme*, Eur. Phys. J B **88**, 191 (2015).

[285] T. Pfeifer, D. Walter, C. Winterfeldt, C. Spielmann, and G. Gerber, *Controlling the spectral shape of coherent soft X-rays*, Appl. Phys. B **80**, 277 (2005).

[286] R. Bartels et al., *Shaped-pulse optimization of coherent emission of high-harmonic soft X-rays*, Nature **406**, 164 (2000).

[287] D. Kammerlander, A. Castro, and M. A. L. Marques, *Optimization of the ionization time of an atom with tailored laser pulses: a theoretical study*, Eur. Phys. J B **90**, 91 (2017).

[288] A. D. Bandrauk and H. T. Yu, *Laser control of molecular ionization with intense short laser pulses*, Int. J. Mass Spectrom. **192**, 379 (1999).

[289] A. Castro, E. Räsänen, A. Rubio, and E. K. U. Gross, *Femtosecond laser pulse shaping for enhanced ionization*, Europhys. Lett. **87**, 53001 (2009).

[290] M. Hellgren, E. Räsänen, and E. K. U. Gross, *Optimal control of strong-field ionization with time-dependent density-functional theory*, Phys. Rev. A **88**, 013414 (2013).

[291] N. I. Shvetsov-Shilovski, L. B. Madsen, and E. Räsänen, *Suppression of strong-field ionization by optimal pulse shaping: Application to hydrogen and the hydrogen molecular ion*, Phys. Rev. A **91**, 023425 (2015).

[292] A. Lindinger, S. M. Weber, A. Merli, F. Sauer, M. Plewicki, and L. Wöste, *Optimal control methods applied on the ionization processes of alkali dimers*, J. Photochem. Photobiol., A **180**, 256 (2006).

[293] B. Schäfer-Bung et al., *Optimal Control of Ionization Processes in NaK: Comparison between Theory and Experiment*, J. Phys. Chem. A **108**, 4175 (2004).

[294] W. Salzmann et al., *Coherent control with shaped femtosecond laser pulses applied to ultracold molecules*, Phys. Rev. A **73**, 023414 (2006).

[295] C. Trallero-Herrero, J. L. Cohen, and T. Weinacht, *Strong-Field Atomic Phase Matching*, Phys. Rev. Lett. **96**, 063603 (2006).

[296] S. Lee, J. Lim, C. Y. Park, and J. Ahn, *Strong-field quantum control of 2+1 photon absorption of atomic sodium*, Opt. Express **19**, 2266 (2011).

[297] C. Trallero-Herrero, S. D. Clow, T. Bergeman, and T. Weinacht, *Strong field coherent control of atomic population transfer*, J. Phys. B **41**, 074014 (2008).

[298] V. C. Gregoric, X. Kang, Z. C. Liu, Z. A. Rowley, T. J. Carroll, and M. W. Noel, *Quantum control via a genetic algorithm of the field ionization pathway of a Rydberg electron*, Phys. Rev. A **96**, 023403 (2017).

[299] T. C. Weinacht and P. H. Bucksbaum, *Using feedback for coherent control of quantum systems*, J. Opt. B: Quantum and Semiclassical Optics **4**, R35 (2002).

[300] L. F. Richardson, *On the approximate arithmetical solution by finite differences of physical problems involving differential equations, with an application to the stresses in a masonry dam*, Proc. R. Soc. Lond. A. Math. Phys. Sci. **83**, 335 (1910).

[301] B. Gustafsson, *Scientific Computing – A Historical Perspective* (Springer, Cham, CH, 2018).

[302] G. E. P. Box and M. E. Muller, *A Note on the Generation of Random Normal Deviates*, Ann. Math. Statist. **29**, 610 (1958).

[303] M. Matsumoto and T. Nishimura, *Mersenne Twister: A 623-dimensionally Equidistributed Uniform Pseudo-random Number Generator*, ACM Trans. Model. Comput. Simul. **8**, 3 (1998).

[304] J. Voss, *An Introduction to Statistical Computing: A Simulation-based Approach*, Wiley Series in Computational Statistics (Wiley, 2013).

[305] N. I. Shvetsov-Shilovski, D. Dimitrovski, and L. B. Madsen, *Ionization in elliptically polarized pulses: Multielectron polarization effects and asymmetry of photoelectron momentum distributions*, Phys. Rev. A **85**, 023428 (2012).

[306] E. Jones, T. Oliphant, P. Peterson, et al., *`SciPy`: Open source scientific tools for Python*, (2001) `http://www.scipy.org/` (visited on 11/19/2018).

[307] G. E. Alefeld, F. A. Potra, and Y. Shi, *Algorithm 748: Enclosing Zeros of Continuous Functions*, ACM Trans. Math. Softw. **21**, 327 (1995).

[308] *Boost C++ Libraries*, https://www.boost.org (visited on 03/14/2019).

[309] E. Hairer, S. Nørsett, and G. Wanner, *Solving Ordinary Differential Equations I Nonstiff problems*, 2nd ed. (Springer, Berlin, DE, 1993).

[310] E. Hairer, *Fortran and Matlab Codes*, https://www.unige.ch/~hairer/software.html (visited on 03/14/2019).

[311] K. Soetaert, J. Cash, and F. Mazzia, *deTestSet: Test Set for Differential Equations*, (2017) https://cran.r-project.org/package=deTestSet (visited on 03/14/2019).

[312] See, e.g., R. LeVeque, *Finite Difference Methods for Ordinary and Partial Differential Equations* (Society for Industrial and Applied Mathematics, 2007).

[313] V. Hernandez, J. E. Roman, and V. Vidal, *SLEPc: A Scalable and Flexible Toolkit for the Solution of Eigenvalue Problems*, ACM Trans. Math. Software **31**, 351 (2005).

[314] J. E. Roman, C. Campos, E. Romero, and A. Tomas, *SLEPc Users Manual*, tech. rep. DSIC-II/24/02 - Revision 3.9 (D. Sistemes Informàtics i Computació, Universitat Politècnica de València, 2018).

[315] See, e.g., L. Lehtovaara, J. Toivanen, and J. Eloranta, *Solution of time-independent Schrödinger equation by the imaginary time propagation method*, J. Comput. Phys. **221**, 148 (2007) and the references therein.

[316] G. Stefanucci and R. Van Leeuwen, *Nonequilibrium many-body theory of quantum systems: a modern introduction* (Cambridge University Press, UK, 2013).

[317] See, e.g., A. Gómez Pueyo, M. A. L. Marques, A. Rubio, and A. Castro, *Propagators for the Time-Dependent Kohn–Sham Equations: Multistep, Runge–Kutta, Exponential Runge–Kutta, and Commutator Free Magnus Methods*, J. Chem. Theory Comput. **14**, PMID: 29672048, 3040 (2018).

[318] See, e.g., A. Al-Mohy and N. Higham, *A New Scaling and Squaring Algorithm for the Matrix Exponential*, SIAM Journal on Matrix Analysis and Applications **31**, 970 (2010).

[319] See, e.g., C. Moler and C. Van Loan, *Nineteen dubious ways to compute the exponential of a matrix, twenty-five years later*, SIAM Rev. **45**, 3 (2003).

[320] J. Crank and P. Nicolson, *A practical method for numerical evaluation of solutions of partial differential equations of the heat-conduction type*, Adv. Comput. Math. **6**, 207 (1996).

[321] M. J. D. Powell, *A Direct Search Optimization Method That Models the Objective and Constraint Functions by Linear Interpolation*, in *Advances in Optimization and Numerical Analysis*, edited by S. Gomez and J.-P. Hennart (Springer Netherlands, Dordrecht, 1994), pp. 51–67.

[322] G. B. Dantzig, *Maximization of a linear function of variables subject to linear inequalities*, Activity analysis of production and allocation **13**, 339 (1951) available in, e.g., R. Cottle, *The Basic George B. Dantzig* (Stanford Business Books, USA, 2003)..

[323] M. J. Powell, *The NEWUOA software for unconstrained optimization without derivatives*, in *Large-scale nonlinear optimization* (Springer, MA, USA, 2006), pp. 255–297.

[324] M. J. D. Powell, *The BOBYQA algorithm for bound constrained optimization without derivatives*, tech. rep. (Univ. of Cambridge, Dept. of Appl. Math. and Theor. Phys., 2009).

[325] A. Conn, N. Gould, and P. Toint, *Trust Region Methods* (Society for Industrial and Applied Mathematics, 2000).

[326] S. G. Johnson, *The NLopt nonlinear-optimization package*, `http://ab-initio.mit.edu/nlopt` (visited on 03/21/2019).

[327] W. Sun and Y.-X. Yuan, *Optimization Theory and Methods: Nonlinear Programming* (Springer, US, 2006).

[328] C. G. BROYDEN, *The Convergence of a Class of Double-rank Minimization Algorithms 1. General Considerations*, IMA J. Appl. Math. **6**, 76 (1970).

[329] R. Fletcher, *A new approach to variable metric algorithms*, Comput. J. **13**, 317 (1970).

[330] D. Goldfarb, *A family of variable-metric methods derived by variational means*, Math. Comp **24**, 23 (1970).

[331] D. F. Shanno, *Conditioning of quasi-Newton methods for function minimization*, Math. Comp **24**, 647 (1970).

[332] B. Shahriari, K. Swersky, Z. Wang, R. P. Adams, and N. de Freitas, *Taking the Human Out of the Loop: A Review of Bayesian Optimization*, Proc. IEEE **104**, 148 (2016).

[333] A. H. G. R. Kan and G. T. Timmer, *Stochastic global optimization methods*, Math. Prog. **39**, 27 (1987).

[334] See, e.g., J. S. Arora, *Introduction to Optimum Design*, 4th ed. (Academic Press, Boston, US, 2017).

[335] E. Birgin and J. Martínez, *Practical Augmented Lagrangian Methods for Constrained Optimization* (Society for Industrial and Applied Mathematics, Philadelphia, PA, 2014).

[336] E. Birgin and J. Martínez, *Improving ultimate convergence of an augmented Lagrangian method*, Optim. Method. Softw. **23**, 177 (2008).

[337] A. Conn, N. Gould, and P. Toint, *A Globally Convergent Augmented Lagrangian Algorithm for Optimization with General Constraints and Simple Bounds*, SIAM Journal on Numerical Analysis **28**, 545 (1991).

[338] See, e.g., B. W. J. McNeil and N. R. Thompson, *X-ray free-electron lasers*, Nat. Photonics **4**, 814 (2010) and the references therein.

[339] J. D. Sadler et al., *Compression of X-ray Free Electron Laser Pulses to Attosecond Duration*, Sci. Rep. **5**, 16755 (2015).

[340] European X-Ray Free-Electron Laser Facility GmbH, *Facts and Figures*, `https://www.xfel.eu/facility/overview/facts_amp_figures/index_eng.html` (visited on 02/11/2019).

[341] M. Kohler, T. Pfeifer, K. Hatsagortsyan, and C. Keitel, *Chapter 4 - Frontiers of Atomic High-Harmonic Generation*, in *Advances in Atomic, Molecular, and Optical Physics*, Vol. 61, edited by E. A. Paul Berman and C. Lin (Academic Press, 2012).

[342] W. Boutu, M. Ducousso, J.-F. Hergott, and H. Merdji, *Overview on HHG High-Flux Sources*, in *Optical Technologies for Extreme-Ultraviolet and Soft X-ray Coherent Sources*, edited by F. Canova and L. Poletto (Springer Berlin Heidelberg, Berlin, Heidelberg, 2015), pp. 63–78.

[343] V. V. Strelkov, V. T. Platonenko, A. F. Sterzhantov, and M. Y. Ryabikin, *Attosecond electromagnetic pulses: generation, measurement, and application. Generation of high-order harmonics of an intense laser field for attosecond pulse production*, Phys. Usp. **59**, 425 (2016).

[344] F. Calegari, G. Sansone, S. Stagira, C. Vozzi, and M. Nisoli, *Advances in attosecond science*, J. Phys. B **49**, 062001 (2016).

[345] L. Young et al., *Roadmap of ultrafast x-ray atomic and molecular physics*, J. Phys. B **51**, 032003 (2018).

[346] D. Peng, L.-W. Pi, M. V. Frolov, and A. F. Starace, *Enhancing high-order-harmonic generation by time delays between two-color, few-cycle pulses*, Phys. Rev. A **95**, 033413 (2017).

[347] M. Førre, E. Mével, and E. Constant, *Seeded attosecond-pulse generation in structured media: A road for attosecond optics*, Phys. Rev. A **83**, 021402 (2011).

[348] S. Ghimire et al., *Strong-field and attosecond physics in solids*, J. Phys. B **47**, 204030 (2014).

[349] Y. S. You, D. Reis, and S. Ghimire, *Anisotropic high-harmonic generation in bulk?crystals*, Nat. Phys. **13**, 345 (2016).

[350] Z. Wang et al., *The roles of photo-carrier doping and driving wavelength in high harmonic generation from a semiconductor*, Nat. Commun. **8**, 1686 (2017).

[351] S. Y. Kruchinin, F. Krausz, and V. S. Yakovlev, *Colloquium: Strong-field phenomena in periodic systems*, Rev. Mod. Phys. **90**, 021002 (2018).

[352] S. Kim, J. Jin, Y.-J. Kim, I.-Y. Park, Y. Kim, and S.-W. Kim, *High-harmonic generation by resonant plasmon field enhancement*, Nature **453**, 757 (2008).

[353] A. Husakou, S.-J. Im, and J. Herrmann, *Theory of plasmon-enhanced high-order harmonic generation in the vicinity of metal nanostructures in noble gases*, Phys. Rev. A **83**, 043839 (2011).

[354] A. Husakou, F. Kelkensberg, J. Herrmann, and M. J. J. Vrakking, *Polarization gating and circularly-polarized high harmonic generation using plasmonic enhancement in metal nanostructures*, Opt. Express **19**, 25346 (2011).

[355] S. L. Stebbings et al., *Generation of isolated attosecond extreme ultraviolet pulses employing nanoplasmonic field enhancement: optimization of coupled ellipsoids*, New J. Phys. **13**, 073010 (2011).

[356] S. Kim, J. Jin, Y.-J. Kim, I.-Y. Park, Y. Kim, and S.-W. Kim, *Kim et al. reply*, Nature **485**, E1 (2012).

[357] T. Shaaran, R. Nicolas, B. Iwan, M. Kovacev, and H. Merdji, *Nano-plasmonic near field phase matching of attosecond pulses*, Sci. Rep. **7**, 6356 (2017).

[358] M. Blanco, C. Hernández-García, A. Chacón, M. Lewenstein, M. T. Flores-Arias, and L. Plaja, *Phase matching effects in high harmonic generation at the nanometer scale*, Opt. Express **25**, 14974 (2017).

[359] E. Neyra et al., *High-order harmonic generation driven by inhomogeneous plasmonics fields spatially bounded: influence on the cut-off law*, J. Opt. **20**, 034002 (2018).

[360] H. Ebadian and M. Mohebbi, *Plasmonic nanostructure assisted HHG in NIR spectrum and thermal analysis*, J. Phys. D: Appl. Phys. **51**, 075307 (2018).

[361] F. Wang et al., *Macroscopic effect of plasmon-driven high-order-harmonic generation*, Phys. Rev. A **96**, 033407 (2017).

[362] M. Sivis, M. Duwe, B. Abel, and C. Ropers, *Nanostructure-enhanced atomic line emission*, Nature **485**, E1 (2012).

[363] M. Krüger, C. Lemell, G. Wachter, J. Burgdörfer, and P. Hommelhoff, *Attosecond physics phenomena at nanometric tips*, J. Phys. B **51**, 172001 (2018).

[364] L. Seiffert, T. Paschen, P. Hommelhoff, and T. Fennel, *High-order above-threshold photoemission from nanotips controlled with two-color laser fields*, J. Phys. B **51**, 134001 (2018).

[365] M. Ciappina, J. A. Pérez-Hernández, T. Shaaran, and M. Lewenstein, *Coherent XUV generation driven by sharp metal tips photoemission*, Eur. Phys. J. D **68**, 172 (2014).

[366] D.-H. Lee et al., *Observation of strongly enhanced ultrashort pulses in 3-D metallic funnel-waveguide*, Opt. Express **22**, 17360 (2014).

[367] S. Han et al., *High-harmonic generation by field enhanced femtosecond pulses in metal-sapphire nanostructure*, Nat. Commun. **7**, 13105 (2016).

[368] M. Spanner, O. Smirnova, P. B. Corkum, and M. Y. Ivanov, *Reading diffraction images in strong field ionization of diatomic molecules*, J. Phys. B **37**, L243 (2004).

[369] H. Fattahi et al., *Third-generation femtosecond technology*, Optica **1**, 45 (2014).

[370] M. T. Hassan et al., *Optical attosecond pulses and tracking the nonlinear response of bound electrons*, Nature **530**, 66 (2016).

[371] A. R. Conn, N. I. M. Gould, and P. L. Toint, *A globally convergent augmented Lagrangian algorithm for optimization with general constraints and simple bounds*, SIAM J. Numer. Anal. **28**, 545 (1991).

[372] E. G. Birgin and J. M. Martínez, *Improving ultimate convergence of an augmented Lagrangian method*, Optim. Method. Softw. **23**, 177 (2008).

[373] J. Solanpää and E. Räsänen, *Control of Rydberg-state population with realistic femtosecond laser pulses*, Phys. Rev. A **98**, 053422 (2018).

[374] See, e.g., T. Hornung, R. Meier, D. Zeidler, K.-L. Kompa, D. Proch, and M. Motzkus, *Optimal control of one- and two-photon transitions with shaped femtosecond pulses and feedback*, Appl. Phys. B **71**, 277 (2000) and the references therein.

[375] R. Netz, T. Feurer, G. Roberts, and R. Sauerbrey, *Coherent population dynamics of a three-level atom in spacetime*, Phys. Rev. A **65**, 043406 (2002).

[376] B. Chatel, J. Degert, S. Stock, and B. Girard, *Competition between sequential and direct paths in a two-photon transition*, Phys. Rev. A **68**, 041402 (2003).

[377] A. Präkelt, M. Wollenhaupt, C. Sarpe-Tudoran, and T. Baumert, *Phase control of a two-photon transition with shaped femtosecond laser-pulse sequences*, Phys. Rev. A **70**, 063407 (2004).

[378] W. Schweizer, P. Faßbinder, and R. González-Féez, *MODEL POTENTIALS FOR ALKALI METAL ATOMS AND Li-LIKE IONS*, At. Data Nucl. Data Tables **72**, 33 (1999).

[379] W. Zhu, J. Botina, and H. Rabitz, *Rapidly convergent iteration methods for quantum optimal control of population*, J. Chem. Phys. **108**, 1953 (1998).

[380] M. Sugawara, *Local control theory for coherent manipulation of population dynamics*, Chem. Phys. Lett. **358**, 290 (2002).

[381] See, e.g., N. Behr and M. B. Raschke, *Optical Antenna Properties of Scanning Probe Tips: Plasmonic Light Scattering, Tip-Sample Coupling, and Near-Field Enhancement*, J. Phys. Chem. C **112**, 3766 (2008) and the references therein.

[382] L. Ortmann et al., *Emergence of a Higher Energy Structure in Strong Field Ionization with Inhomogeneous Electric Fields*, Phys. Rev. Lett. **119**, 053204 (2017).

[383] L. Ortmann and A. S. Landsman, *Analysis of the higher-energy structure in strong-field ionization with inhomogeneous electric fields*, Phys. Rev. A **97**, 023420 (2018).

[384] M. F. Ciappina et al., *Emergence of a Higher Energy Structure in Strong Field Ionization with Inhomogeneous Laser Fields*, in High-Brightness Sources and Light-driven Interactions (2018).

[385] M. Kruger, M. Schenk, M. Forster, and P. Hommelhoff, *Attosecond physics in photoemission from a metal nanotip*, J. Phys. B **45**, 074006 (2012).

[386] L. Wimmer, G. Herink, D. R. Solli, S. V. Yalunin, K. E. Echternkamp, and C. Ropers, *Terahertz control of nanotip photoemission*, Nat. Phys. **10**, 43 (2014).

[387] G. M. Caruso, F. Houdellier, P. Abeilhou, and A. Arbouet, *Development of an ultrafast electron source based on a cold-field emission gun for ultrafast coherent TEM*, Appl. Phys. Lett. **111**, 023101 (2017).

[388] B. Barwick, C. Corder, J. Strohaber, N. Chandler-Smith, C. Uiterwaal, and H. Batelaan, *Laser-induced ultrafast electron emission from a field emission tip*, New J. Phys. **9**, 142 (2007).

[389] G. Herink, D. R. Solli, M. Gulde, and C. Ropers, *Field-driven photoemission from nanostructures quenches the quiver motion*, Nature **483**, 190 (2012).

[390] R. Bormann, M. Gulde, A. Weismann, S. V. Yalunin, and C. Ropers, *Tip-Enhanced Strong-Field Photoemission*, Phys. Rev. Lett. **105**, 147601 (2010).

[391] B. Förg et al., *Attosecond nanoscale near-field sampling*, Nat. Commun. **7**, 11717 (2016).

[392] S. V. Yalunin et al., *Field localization and rescattering in tip-enhanced photoemission*, Ann. Phys. **525**, L12.

[393] R. G. Hobbs et al., *High-density Au nanorod optical field-emitter arrays*, Nanotechnology **25**, 465304 (2014).

[394] F. Kusa, K. E. Echternkamp, G. Herink, C. Ropers, and S. Ashihara, *Optical field emission from resonant gold nanorods driven by femtosecond mid-infrared pulses*, AIP Adv. **5**, 077138 (2015).

[395] A. Grubisic et al., *Plasmonic Near-Electric Field Enhancement Effects in Ultrafast Photoelectron Emission: Correlated Spatial and Laser Polarization Microscopy Studies of Individual Ag Nanocubes*, Nano Lett. **12**, 4823 (2012).

[396] R. G. Hobbs et al., *High-Yield, Ultrafast, Surface Plasmon-Enhanced, Au Nanorod Optical Field Electron Emitter Arrays*, ACS Nano **8**, 11474 (2014).

[397] A. Grubisic, V. Schweikhard, T. A. Baker, and D. J. Nesbitt, *Coherent Multiphoton Photoelectron Emission from Single Au Nanorods: The Critical Role of Plasmonic Electric Near-Field Enhancement*, ACS Nano **7**, 87 (2013).

[398] J. A. Schuller, E. S. Barnard, W. Cai, Y. C. Jun, J. S. White, and M. L. Brongersma, *Plasmonics for extreme light concentration and manipulation*, Nat. Mater. **9**, 193 (2010).

[399] Y. Chou, P.-C. Li, T.-S. Ho, and S.-I. Chu, *Generation of an isolated few-attosecond pulse in optimized inhomogeneous two-color fields*, Phys. Rev. A **92**, 023423 (2015).

[400] S. N. Pugliese, A. S. Simonsen, M. Førre, and J. P. Hansen, *High-order-harmonic spectra from atoms in intense laser fields: Exact versus approximate methods*, Phys. Rev. A **92**, 023424 (2015).

[401] S. Sukiasyan, C. McDonald, C. Destefani, M. Y. Ivanov, and T. Brabec, *Multielectron Correlation in High-Harmonic Generation: A 2D Model Analysis*, Phys. Rev. Lett. **102**, 223002 (2009).

[402] E. V. Gryzlova, A. N. Grum-Grzhimailo, E. I. Staroselskaya, N. Douguet, and K. Bartschat, *Quantum coherent control of the photoelectron angular distribution in bichromatic-field ionization of atomic neon*, Phys. Rev. A **97**, 013420 (2018).

[403] S. N. Yurchenko, S. Patchkovskii, I. V. Litvinyuk, P. B. Corkum, and G. L. Yudin, *Laser-Induced Interference, Focusing, and Diffraction of Rescattering Molecular Photoelectrons*, Phys. Rev. Lett. **93**, 223003 (2004).

[404] C. Vozzi et al., *Controlling Two-Center Interference in Molecular High Harmonic Generation*, Phys. Rev. Lett. **95**, 153902 (2005).

[405] L. Chen, C. Huang, X. Zhu, P. Lan, and P. Lu, *Molecular photoelectron holography by an attosecond XUV pulse in a strong infrared laser field*, Opt. Express **22**, 20421 (2014).

[406] X.-B. Bian and A. D. Bandrauk, *Attosecond Time-Resolved Imaging of Molecular Structure by Photoelectron Holography*, Phys. Rev. Lett. **108**, 263003 (2012).

[407] See, e.g., S. Rausch, T. Binhammer, A. Harth, F. X. Kärtner, and U. Morgner, *Few-cycle femtosecond field synthesizer*, Opt. Express **16**, 17410 (2008).

[408] T. Nubbemeyer, K. Gorling, A. Saenz, U. Eichmann, and W. Sandner, *Strong-Field Tunneling without Ionization*, Phys. Rev. Lett. **101**, 233001 (2008).

[409] S. Larimian et al., *Coincidence spectroscopy of high-lying Rydberg states produced in strong laser fields*, Phys. Rev. A **94**, 033401 (2016).

[410] A. Signoles et al., *Coherent Transfer between Low-Angular-Momentum and Circular Rydberg States*, Phys. Rev. Lett. **118**, 253603 (2017).

[411] S. Patsch, D. M. Reich, J.-M. Raimond, M. Brune, S. Gleyzes, and C. P. Koch, *Fast and accurate circularization of a Rydberg atom*, Phys. Rev. A **97**, 053418 (2018).

[412] A. A. Morgan, V. Zhelyazkova, and S. D. Hogan, *Preparation of circular Rydberg states in helium with $n \geq 70$ using a modified version of the crossed-fields method*, Phys. Rev. A **98**, 043416 (2018).

[413] M. Krüger, C. Lemell, G. Wachter, J. Burgdörfer, and P. Hommelhoff, *Attosecond physics phenomena at nanometric tips*, J. Phys. B **51**, 172001 (2018).

[414] C. Jin and C. D. Lin, *Spatially coherent high-order harmonics generated at optimal high gas pressure with high-intensity one- or two-color laser pulses*, Phys. Rev. A **94**, 043804 (2016).

[415] X.-Y. Li, G.-L. Wang, and X.-X. Zhou, *Effects of pressure and gas-jet thickness on the generation of attosecond pulse*, Chin. Phys. B **23**, 013102 (2014).

[416] V. Linko, B. Shen, K. Tapio, J. J. Toppari, M. A. Kostiainen, and S. Tuukkanen, *One-step large-scale deposition of salt-free DNA origami nanostructures*, Sci. Rep. **5**, Article, 15634 (2015).

[417] B. Shen et al., *Plasmonic nanostructures through DNA-assisted lithography*, Sci. Adv. **4** (2018).

[418] K. Yabana, T. Sugiyama, Y. Shinohara, T. Otobe, and G. F. Bertsch, *Time-dependent density functional theory for strong electromagnetic fields in crystalline solids*, Phys. Rev. B **85**, 045134 (2012).

[419] S. A. Sato and K. Yabana, *Maxwell + TDDFT multi-scale simulation for laser-matter interactions*, J. Adv. Simul. Sci. Eng. **1**, 98 (2014).

[420] Y. Li, S. He, A. Russakoff, and K. Varga, *Accurate time propagation method for the coupled Maxwell and Kohn-Sham equations*, Phys. Rev. E **94**, 023314 (2016).

[421] V. A. Goncharov, *Nonlinear optical response in solids from time-dependent density-functional theory simulations*, J. Chem. Phys. **139**, 084104 (2013).

[422] E. Lorin, S. Chelkowski, and A. Bandrauk, *A numerical Maxwell–Schrödinger model for intense laser–matter interaction and propagation*, Comput. Phys. Commun. **177**, 908 (2007).

[423] M. Noda et al., *SALMON: Scalable Ab-initio Light–Matter simulator for Optics and Nanoscience*, Comput. Phys. Commun. **235**, 356 (2019).

[424] M. Ruggenthaler, N. Tancogne-Dejean, J. Flick, H. Appel, and A. Rubio, *From a quantum-electrodynamical light-matter description to novel spectroscopies*, Nat. Rev. Chem. **2**, 0118 (2018).

[425] J. Dongarra, S. Gottlieb, and W. T. C. Kramer, *Race to Exascale*, Comput. Sci. Eng. **21**, 4 (2019).

[426] D. Qian and Z. Luan, *High Performance Computing Development in China: A Brief Review and Perspectives*, Comput. Sci. Eng. **21**, 6 (2019).

[427] D. Kothe, S. Lee, and I. Qualters, *Exascale Computing in the United States*, Comput. Sci. Eng. **21**, 17 (2019).

[428] G. Kalbe, *The European Approach to the Exascale Challenge*, Comput. Sci. Eng. **21**, 42 (2019).

[429] B. Sorensen, *Japan's Flagship 2020 "Post-K" System*, Comput. Sci. Eng. **21**, 48 (2019).

Original papers

Optimal control of high-harmonic generation by intense few-cycle pulses

J. Solanpää, J. A. Budagosky, N. I. Shvetsov-Shilovski, A. Castro, A. Rubio, and E. Räsänen
Optimal control of high-harmonic generation by intense few-cycle pulses
Phys. Rev. A **90**, 053402 (2014)

Optimal control of high-harmonic generation by intense few-cycle pulses

J. Solanpää,[1,*] J. A. Budagosky,[2] N. I. Shvetsov-Shilovski,[1] A. Castro,[2,3] A. Rubio,[4,5] and E. Räsänen[1,†]

[1]*Department of Physics, Tampere University of Technology, Tampere FI-33101, Finland*

[2]*Institute for Biocomputation and Physics of Complex Systems (BIFI) and Zaragoza Center for Advanced Modeling (ZCAM), University of Zaragoza, E-50009 Zaragoza, Spain*

[3]*ARAID Foundation, María de Luna 11, Edificio CEEI Aragón, Zaragoza E-50018, Spain*

[4]*Max Planck Institute for the Structure and Dynamics of Matter, 22761 Hamburg, Germany*

[5]*Nano-Bio Spectroscopy Group and ETSF, Departamento de Física de Materiales, CFM CSIC-UPV/EHU-MPC and DIPC, Universidad del País Vasco, E-20018 San Sebastián, Spain*

(Received 23 June 2014; published 3 November 2014)

At the core of attosecond science lies the ability to generate laser pulses of subfemtosecond duration. In tabletop devices the process relies on high-harmonic generation, where a major challenge is to obtain high yields and high cutoff energies required for the generation of attosecond pulses. We develop a computational method that can simultaneously resolve these issues by optimizing the driving pulses using quantum optimal control theory. Our target functional, an integral over the harmonic yield over a desired energy range, leads to a remarkable cutoff extension and yield enhancement for a one-dimensional model H atom. The physical enhancement process is shown to be twofold: the cutoff extension is of classical origin, whereas the yield enhancement arises from increased tunneling probability. The scheme is directly applicable to more realistic models and, within straightforward refinements, also to experimental verification.

DOI: 10.1103/PhysRevA.90.053402 PACS number(s): 32.80.Rm, 42.65.Ky, 42.65.Re, 42.79.Nv

The revolution of attosecond science, i.e., monitoring and controlling the dynamics of electrons in their native time scale, relies on the generation of laser pulses with duration of a few dozen attoseconds [1]. Such pulses can be generated by using large-scale free-electron laser facilities [2] or in tabletop devices using high-harmonic generation (HHG), an ultrafast frequency conversion process [1]. Using tabletop devices, however, comes with a price: the generated attosecond pulses are often too long and they suffer from low intensity [1].

A high-harmonic spectrum has an energy range of nearly constant intensity (plateau), which ends in a distinctive cutoff [3]. Attosecond pulses are formed from the harmonics on the plateau [1]. Hence, the low amplitude of the pulses is due to low harmonic yield and the pulse duration is determined by the cutoff energy (the higher the energy, the shorter the pulse) [1]. The objectives of increasing the yield and reducing the pulse duration can be addressed by temporal shaping of the driving pulse—already experimentally realizable either with multicolor fields or with more sophisticated techniques [4]. Yet a crucial question remains unanswered: how to find the optimal shape of the driving pulse to enhance HHG.

Numerous previous studies have tackled the issues of cutoff and yield; for a recent review see, e.g., Refs. [5,6]. The main scheme behind the cutoff extension has been using two-color laser fields [7,8] or chirped pulses [9–11], but also steepening of the carrier wave [12] or even using a sawtooth pulse should extend the cutoff [13]. In addition, combined temporal and spatial synthesis of the driving field has been shown to extend the cutoff [14]. A previous study based on quantum optimal control theory (QOCT), for example, demonstrated some cutoff extension, albeit with a low yield, by maximizing the ground-state occupation at the end of the pulse [15]. Yield increase of the plateau has been accomplished, e.g., by two-color fields [16–21] and also by using a mixture of two target gases [22]. In a separate work [23], some of the authors of the present work addressed the selective enhancement of harmonic peaks; selective harmonic enhancement has been studied using QOCT also in Ref. [24], and experimentally, e.g., in Ref. [25]. Recently also the attosecond pulse generation has been optimized using genetic algorithms [26].

In this paper, we provide an efficient computational method to *simultaneously* enhance both the yield and the cutoff energy of the harmonic plateau by optimizing the driving pulses with QOCT [27–29]. The optimal pulses are found by maximizing the target functional, an integral over the harmonic yield over a desired energy range. Surprisingly, the enhancements are achieved with fixed-fluence pulses; i.e., the search is performed over the set of pulses with equal duration and fixed fluence (integrated intensity). We examine in detail the physical origin behind the enhancement, which is found to be of classical nature to a significant extent.

To demonstrate our method, we use one-dimensional hydrogen with the soft-Coulomb potential [30] $V(x) = -1/\sqrt{x^2+1}$ as our model system and the laser-electron interaction is calculated in the dipole approximation. The harmonic spectra are calculated from the Fourier transform of the dipole acceleration $\ddot{d}(\omega)$ as $S(\omega) = |\ddot{d}(\omega)|^2/\omega^2$ as suggested in Ref. [31]. Unless otherwise specified, Hartree atomic units (a.u.) are used throughout the paper, i.e., $\hbar = q_e = m_e = 1/(4\pi\epsilon_0) = 1$. The time-evolution operator is calculated using the exponential midpoint rule [32] with the Lanczos algorithm [33] for the operator exponential; during time propagation we also use imaginary absorbing boundaries. We use box sizes of 4000–6000, grid spacings of 0.2–0.3, and time steps of 0.03–0.05; the parameters have been checked to ensure full convergence. Most of the calculations—including QOCT discussed below—are done in length gauge using the OCTOPUS code [34].

In QOCT one solves for a laser pulse $\epsilon(t)$ that maximizes a target functional $J_1[\epsilon]$. To optimize the harmonic spectrum,

*janne@solanpaa.fi

†esa.rasanen@tut.fi

we have implemented a target of the form

$$J_1[\epsilon] = \int_{\omega_a}^{\omega_b} |\ddot{d}[\epsilon](\omega)|^2 \, d\omega, \tag{1}$$

where $[\omega_a,\omega_b]$ is the frequency range for the desired enhancement of the HHG spectrum. The field ϵ is represented by a set of parameters, and maximization of the functional defined in Eq. (1) amounts to a function maximization for those parameters. We have used both a gradient-free algorithm (NEWUOA [35]) and the gradient-based Broyden-Fletcher-Goldfarb-Shannon (BFGS) algorithm [36] (the expression for the gradient is supplied by the QOCT). As we will see, both algorithms provide similar enhancements in the harmonic spectrum. The optimized pulses are constrained by (i) a finite number of frequencies with the maximum frequency $\omega_{\max}$, (ii) a fixed pulse length, and (iii) a fixed fluence which is set to that of a single-frequency *reference* pulse, whose shape is shown in the figures below. For each set of pulse constraints, we begin the optimization from several (5–10) random initial pulses and report here the best result; it is important to note that QOCT always converges into a *local* maximum in the parameter space.

First we apply the NEWUOA algorithm to optimize a laser pulse for HHG in the target interval $\omega \in [1.3,4]$ a.u. The pulse length is fixed to $T = 1104$ (26.7 fs) and the carrier frequency of the reference pulse is $\omega = 0.0569$ a.u. (wavelength $\lambda \approx 800$ nm corresponding to the typical range of Ti:sapphire lasers), which we choose to keep as the maximum allowed frequency of the optimized pulse to prevent the formation of complicated pulses with high-frequency components. The peak intensity of the reference pulse is 6×10^{13} W/cm^2, and the fluence is kept constant in the optimization. The reference and optimized pulses are shown in Fig. 1(a) as red (light gray) and blue (dark gray) lines, respectively. The optimized harmonic spectrum in Fig. 1(b) completely fulfills the desired target, and in addition to the cutoff extension, the yield is also increased by several orders of magnitude.

Next we comment on the two most obvious characteristics of the optimized pulse in Fig. 1(a). First, it is important to note that the high-intensity half cycle in the beginning is not responsible for the significant increase in the HHG yield and cutoff. If this part were later in the pulse, the cutoff would be at $\omega \approx 2.5$ a.u. A similar effect is seen if, e.g., the last low-intensity peak is missing. Second, as shown in the inset of Fig. 1(a), the optimized pulse contains lower-frequency components. Indeed, the standard theoretical HHG considerations predict that lower frequencies should lead to higher cutoff energy due to higher ponderomotive energy. However, merely using low-frequency single-color pulses produces very low yields. It is the shaped multifrequency pulses that produce both the large cutoff and high intensities. Furthermore, in the case of HHG resulting from pulses that have a single carrier frequency, the harmonic peaks are equally separated by twice the carrier frequency. In the case of optimized pulses, however, we find no connection between the frequency components in the pulse and the HHG peak separations. This is expected in view of the complexity of the optimized pulse in the time-frequency plane, even though we applied rather simple pulse constraints as explained above.

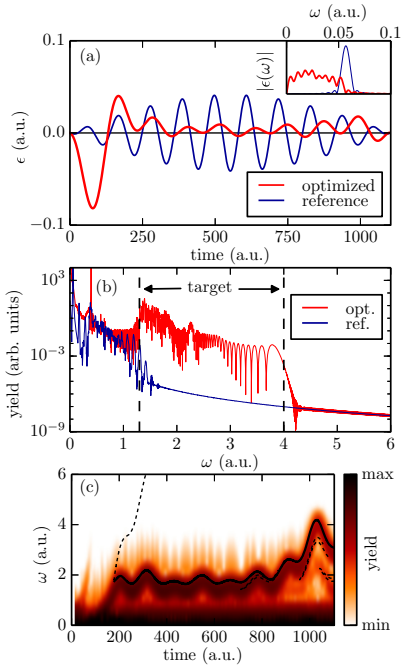

FIG. 1. (Color online) Optimization results for the HHG spectrum with the target range $\omega \in [1.3,4]$ a.u. The pulse length is $T = 1104$ a.u. and the frequency of the reference pulse is $\omega = 0.0569$ a.u., equal to the maximum frequency in the optimization. The fluence is kept constant. (a) Optimized [red (light gray)] and reference [blue (dark gray)] pulses and their frequencies (inset). (b) High-harmonic spectra for optimized [red (light gray)] and reference [blue (dark gray)] pulses. The target range is shown with vertical dashed lines. (c) Quantum-mechanical time-dependent harmonic spectrum in log scale [color (gray scale)] and return energies calculated from the semiclassical model (solid line). Spurious branches from a uniform tunneling rate are shown with dashed lines (see text).

The emission process is further demonstrated in Fig. 1(c), where the color (gray scale) image shows the time-frequency map of the quantum dipole acceleration, $\ddot{d}(t,\omega)$. The time-frequency map is calculated as a discrete short-time Fourier transform (STFT) [37] using the Blackman window function [38]. In essence, the time axis is split into multiple overlapping windows, and the dipole acceleration is Fourier transformed in each window. Finally, we plot the quantity $S(t,\omega) = |\ddot{d}(t,\omega)|^2/\omega^2$ in log scale in analog with the harmonic yield; here t corresponds to the middle of each time window of the STFTs. $S(t,\omega)$ essentially describes HHG *in time*. Bicubic interpolation is used for slight visual improvements. The cutoff extension up to $\omega \lesssim 2.5$ a.u. occurs throughout the pulse as it is the effect of the high-intensity peak. The full extension up to $\omega = 4$ a.u., however, occurs only at the end of the pulse. This

clarifies the above-mentioned fact that the complete structure of the optimized pulse is important.

Next we examine the physical origin of the cutoff extension in more detail by employing semiclassical simulations. An ensemble of classical trajectories is propagated with initial times t_0 distributed according to either a uniform tunneling rate $w(t_0) \sim 1$ or exponential tunneling rate $w(t_0) \sim \exp\{-[2(2I_p)^{3/2}]/[3|\epsilon(t_0)|]\}$ [39–41], where $I_p = 0.669$ a.u. is the ionization potential of our system. At the tunnel exit obtained from the classical turning point equation $V(x) + F_x(t)x = -I_p$, the velocity is set to zero and the electron is propagated classically. Upon return of the tunneled electron to the origin, a photon is emitted with frequency corresponding to the kinetic energy of the electron; also later returns are recorded and taken into account. Note that in contrast to the three-step (simple man) model [42], where the electron starts from the origin and moves in the laser field only, the electron in our model starts at the tunnel exit and moves in the combined force field of the laser and the atomic potential. It should be noted that in contrast to our semiclassical simulation taking the atomic potential into account, the three-step model underestimates the cutoff energy. For the parameters of Fig. 2 the cutoff calculated from the three-step model corresponds to 3.2 a.u. (compare to 4.2 a.u. predicted by semiclassical simulations with binding potential shown in Fig. 2).

The return energy maps of the semiclassical model as a function of the return time (solid curves) are compared with the time-dependent harmonic spectrum in Fig. 1(c). Due to the pulse shape, the electron can return only once to the origin. With uniform tunneling distribution, the semiclassical model exhibits a few spurious branches (dashed black curves), which are suppressed when using the exponential tunneling rate. The remarkable agreement between the semiclassical and quantum descriptions highlights the classical origin of the cutoff extension.

In Fig. 2(a) we show a BFGS-optimized pulse [red (light gray)] with the same reference pulse [blue (dark gray)] as in Fig. 1. The target range is now $\omega \in [1,5]$ a.u., i.e., considerably larger than in the previous case. Despite a slightly more complicated temporal shape of the optimized pulse, the resulting HHG spectrum [Fig. 2(b)] is similar to the first case. Now, however, the optimized pulse allows multiple returns of the electron to the origin as shown in Fig. 2(c) when using an exponential tunneling rate. Not all of the quantum-mechanical harmonic emissions can be found in the semiclassical model with exponential tunneling distribution. They are, however, allowed by the semiclassical model and visible when using a uniform tunneling rate. Therefore, the semiclassical picture does agree with the quantum description, but the exponential tunneling distribution does not produce all tunneling events.

Next we double the pulse length while keeping the peak intensity of the reference pulse, the maximum frequency, and the target HHG range the same (note that the fluence is also doubled). The BFGS-optimized pulse of Fig. 3(a) now leads to complete extension of the cutoff all the way up to $\omega = 5$ a.u., as demonstrated in Fig. 3(b). This is likely due to higher fluence and more freedom in the shaping of the longer pulse.

The effect of late returns [see, e.g., Fig. 2(c)] can be analyzed in the semiclassical picture. The harmonic spectrum can be calculated as a histogram of the electron energies

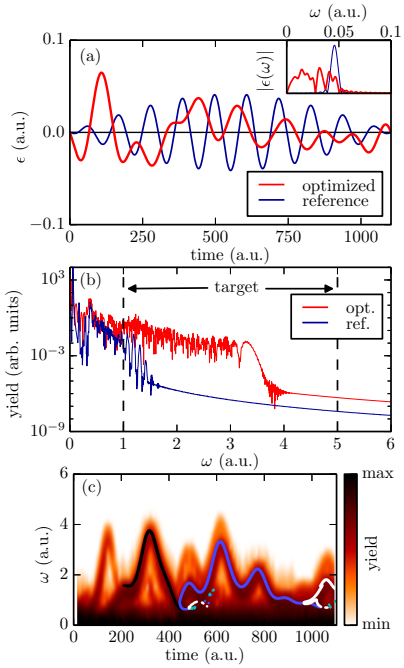

FIG. 2. (Color online) Same as Fig. 1 but for an extended target range (up to $\omega = 5$ a.u.) and for the gradient-based BFGS optimization algorithm. In (c), energies of an electron calculated from the semiclassical model upon its first, second, third, and fourth return to the origin are shown with black, blue (medium gray), white, and cyan (light gray) curves, respectively.

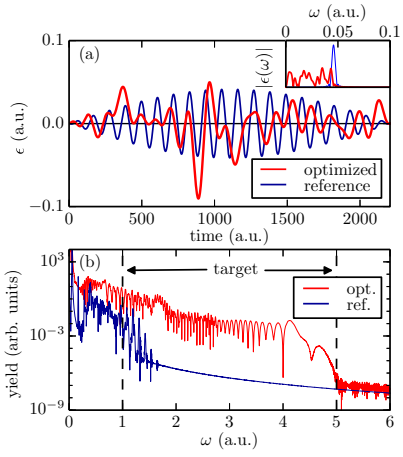

FIG. 3. (Color online) Same as Figs. 2(a) and 2(b) but for a longer pulse with $T = 2209$ a.u. (53.5 fs).

upon return to the origin with weights from the exponential tunneling rate (see above). The resulting spectra demonstrate varying contributions of late returns between different pulses. Even in the case of pulse of Fig. 2(a), where late returns are evident, their contributions to the spectra in the semiclassical models are minimal. In contrast, for the optimal pulse of Fig. 3, also the second return plays an important role in enhanced HHG.

The yield increase can be attributed to the increased tunneling probability compared to the reference pulses. Indeed, the yield increase of comparable, albeit slightly larger, magnitude can be found when using single-frequency pulses with the same maximum amplitude as in the optimized pulses, but the extension of the cutoff does not reach the optimized results. Sensitivity of HHG to the pulse amplitude has been previously reported in, e.g., Refs. [18,43]. The sensitivity is also obvious from the analytic factorization of the HHG rates in Ref. [44]. We emphasize that the yield increase of the presented optimized HHG arises from an increased tunneling rate, not from resonances as, e.g., in Ref. [16]: in our case a minimum of seven-photon absorption would be required, which is highly unlikely.

Finally, we verify which stationary states are involved in the enhanced HHG process. For this purpose, we solve the time-dependent Schrödinger equation in *momentum space and velocity gauge* by expanding the state in terms of the eigenstates of the field-free Hamiltonian [45]. Note that the occupations are gauge dependent. We find that approximately four lowest bound states are essential for the enhanced HHG, but ten are required for (nearly) full convergence of the spectrum; the numbers are similar for reference pulses. However, in the optimized HHG much of the electron density reaches high-energy continuum states, whereas for the reference pulse the electron occupation is mostly in the bound states and in the low-energy continuum (see Fig. 4).

To summarize, we have developed an optimal-control scheme to simultaneously enhance both the yield and the cutoff energy of HHG. Our target functional, an integral over the harmonic yield in a desired energy range, leads to a significant increase in the HHG yield and cutoff energy within two different optimization algorithms. Furthermore, we have shown through semiclassical studies that the extension of the cutoff is of classical origin. Instead, the increase in the harmonic yield is found to be due to increased

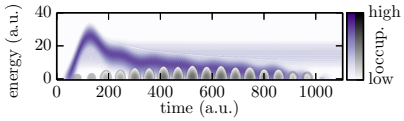

FIG. 4. (Color online) Occupations (log scale) of stationary states in velocity gauge for the reference (gray bulb-shaped structures at the bottom) and optimized (colored structures elsewhere) pulse of Fig. 1.

tunneling probability arising from increased peak amplitudes, while the fluence is kept constant in the optimization. We note that in higher-dimensional models, the harmonic yield will be affected by transversal spreading of the electron wave packet. However, our preliminary results (not shown here) demonstrate even the one-dimensional-optimized pulses provide qualitatively similar cutoff extension and no significant loss of yield also when applied to a two-dimensional model; we expect a similar tendency also for three dimensions. In addition, by doing the optimization within the same dimensionality, there can be additional degrees of freedom in the pulse regarding, e.g., polarization, number of frequency components, and pulse sources, which will help counter the issue of wave packet spreading.

We leave the detailed analysis of realistic pulse constraints to three-dimensional and many-electron models, where such analysis will be more relevant. With such refinements, we expect our method to be usable also in experimental applications, which can have direct implications in the development of efficient, flexible, and tunable light-emitting tabletop devices.

This work was supported by the Academy of Finland; COST Action CM1204 (XLIC); the European Community's FP7 through the CRONOS project, Grant No. 280879; the European Research Council Advanced Grant DYNamo (Grant No. ERC-2010-AdG-267374); Grupos Consolidados UPV/EHU del Gobierno Vasco (Grant No. IT578-13); Spanish Grant No. FIS2010-21282-C02-01; and the University of Zaragoza (Project No. UZ2012-CIE-06). We also acknowledge CSC—the Finnish IT Center for Science—for computational resources. Several PYTHON extensions [46–48] were used for the analysis.

[1] See, e.g., P. B. Corkum and F. Krausz, Nat. Phys. **3**, 381 (2007).

[2] See, e.g., B. W. J. McNeil and N. R. Thompson, Nat. Photonics **4**, 814 (2010), and references therein.

[3] See, e.g., A. Scrinzi and H. G. Muller, in *Strong Field Laser Physics*, edited by T. Brabec (Springer, New York, 2008).

[4] See, e.g., A. Wirth, M. T. Hassan, I. Grgura, J. Gagnon, A. Moulet, T. T. Luu, S. Pabst, R. Santra, Z. A. Alahmed, A. M. Azzeer *et al.*, Science **334**, 195 (2011). H. Fattahi, H. G. Barros, M. Gorjan, T. Nubbemeyer, B. Alsaif, C. Y. Teisset, M. Schultze, S. Prinz, M. Haefner, M. Ueffing *et al.*, Optica **1**, 45 (2014).

[5] C. Winterfeldt, C. Spielmann, and G. Gerber, Rev. Mod. Phys. **80**, 117 (2008).

[6] M. Kohler, T. Pfeifer, K. Hatsagortsyan, and C. Keitel, in *Advances in Atomic, Molecular, and Optical Physics*, Vol. 61, edited by E. A. Paul Berman and C. Lin (Academic Press, New York, 2012).

[7] T. Shao, G. Zhao, B. Wen, and H. Yang, Phys. Rev. A **82**, 063838 (2010).

[8] Z. Zeng, Y. Cheng, X. Song, R. Li, and Z. Xu, Phys. Rev. Lett. **98**, 203901 (2007).

[9] D. G. Lee, J.-H. Kim, K.-H. Hong, and C. H. Nam, Phys. Rev. Lett. **87**, 243902 (2001).

[10] J. J. Carrera and Shih-I Chu, Phys. Rev. A **75**, 033807 (2007).
[11] Y. Xiang, Y. Niu, and S. Gong, Phys. Rev. A **79**, 053419 (2009).
[12] S. B. P. Radnor, L. E. Chipperfield, P. Kinsler, and G. H. C. New, Phys. Rev. A **77**, 033806 (2008).
[13] L. E. Chipperfield, J. S. Robinson, J. W. G. Tisch, and J. P. Marangos, Phys. Rev. Lett. **102**, 063003 (2009).
[14] J. A. Pérez-Hernández, M. F. Ciappina, M. Lewenstein, L. Roso, and A. Zaïr, Phys. Rev. Lett. **110**, 053001 (2013).
[15] E. Räsänen and L. B. Madsen, Phys. Rev. A **86**, 033426 (2012).
[16] K. L. Ishikawa, Phys. Rev. Lett. **91**, 043002 (2003).
[17] K. L. Ishikawa, Phys. Rev. A **70**, 013412 (2004).
[18] I. J. Kim, C. M. Kim, H. T. Kim, G. H. Lee, Y. S. Lee, J. Y. Park, D. J. Cho, and C. H. Nam, Phys. Rev. Lett. **94**, 243901 (2005).
[19] F. Brizuela, C. M. Heyl, P. Rudawski, D. Kroon, L. Rading, J. M. Dahlström, J. Mauritsson, P. Johnsson, C. L. Arnold, and A. L'Huillier, Sci. Rep. **3**, 1410 (2013).
[20] E. Mansten, J. M. Dahlström, P. Johnsson, M. Swoboda, A. L'Huillier, and J. Mauritsson, New J. Phys. **10**, 083041 (2008).
[21] A. Fleischer and N. Moiseyev, Phys. Rev. A **77**, 010102 (2008).
[22] E. J. Takahashi, T. Kanai, K. L. Ishikawa, Y. Nabekawa, and K. Midorikawa, Phys. Rev. Lett. **99**, 053904 (2007).
[23] A. Castro, A. Rubio, and E. K. U. Gross (unpublished).
[24] I. Schaefer and R. Kosloff, Phys. Rev. A **86**, 063417 (2012).
[25] P. Wei, J. Miao, Z. Zeng, C. Li, X. Ge, R. Li, and Z. Xu, Phys. Rev. Lett. **110**, 233903 (2013).
[26] E. Balogh, B. Bódi, V. Tosa, E. Goulielmakis, K. Varjú, and P. Dombi, Phys. Rev. A **90**, 023855 (2014).
[27] A. P. Peirce, M. A. Dahleh, and H. Rabitz, Phys. Rev. A **37**, 4950 (1988).
[28] R. Kosloff, S. Rice, P. Gaspard, S. Tersigni, and D. Tannor, Chem. Phys. **139**, 201 (1989).
[29] For a recent review on QOCT, see, e.g., J. Werschnik and E. K. U. Gross, J. Phys. B **40**, R175 (2007); C. Brif, R. Chakrabarti, and H. Rabitz, New J. Phys. **12**, 075008 (2010).
[30] J. Javanainen, J. H. Eberly, and Q. Su, Phys. Rev. A **38**, 3430 (1988).
[31] J. C. Baggesen and L. B. Madsen, J. Phys. B **44**, 115601 (2011).
[32] See, e.g., A. Castro, M. A. L. Marques, and A. Rubio, J. Chem. Phys. **121**, 3425 (2004).
[33] M. Hochbruck and C. Lubich, SIAM J. Numer. Anal. **34**, 1911 (1977).
[34] M. A. Marques, A. Castro, G. F. Bertsch, and A. Rubio, Comput. Phys. Commun. **151**, 60 (2003); A. Castro, H. Appel, M. Oliveira, C. A. Rozzi, X. Andrade, F. Lorenzen, M. A. L. Marques, E. K. U. Gross, and A. Rubio, Phys. Status Solidi B **243**, 2465 (2006).
[35] M. J. D. Powell, IMA J. Numer. Anal. **28**, 649 (2008).
[36] R. Fletcher, *Practical Methods of Optimization*, 2nd ed. (Wiley, New York, 2000).
[37] J. B. Allen, IEEE Trans. Acoust., Speech, Signal Process. **ASSP-25**, 235 (1977).
[38] R. B. Blackman and J. W. Tukey, *The Measurement of Power Spectra* (Dover, New York, 1958).
[39] A. Perelomov, V. Popov, and M. Terent'ev, Zh. Eksp. Teor. Fiz. **50**, 1393 (1966) [Sov. Phys. JETP **23**, 924 (1966)].
[40] M. Ammosov, N. Delone, and V. Krainov, Zh. Eksp. Teor. Fiz. **91**, 2008 (1986) [Sov. Phys. JETP **64**, 1191 (1986)].
[41] N. B. Delone and V. P. Krainov, J. Opt. Soc. Am. B **8**, 1207 (1991).
[42] P. B. Corkum, Phys. Rev. Lett. **71**, 1994 (1993).
[43] J. M. Dahlström, A. L'Huillier, and J. Mauritsson, J. Phys. B **44**, 095602 (2011).
[44] M. V. Frolov, N. L. Manakov, T. S. Sarantseva, M. Y. Emelin, M. Y. Ryabikin, and A. F. Starace, Phys. Rev. Lett. **102**, 243901 (2009).
[45] N. I. Shvetsov-Shilovski, E. Räsänen, G. G. Paulus, and L. B. Madsen, Phys. Rev. A **89**, 043431 (2014).
[46] F. Prez and B. E. Granger, Comput. Sci. Eng. **9**, 21 (2007).
[47] J. D. Hunter, Comput. Sci. Eng. **9**, 90 (2007).
[48] E. Jones, T. Oliphant, P. Peterson *et al.*, www.scipy.org (2011); T. E. Oliphant, Comput. Sci. Eng. **9**, 10 (2007).

Optimal control of photoelectron emission by realistic waveforms

The following article is a re-typeset Accepted Manuscript of

J. Solanpää, M. Ciappina, and E. Räsänen
Optimal control of photoelectron emisison by realistic waveforms
J. Mod. Opt **64**, 1784–1792 (2017)

Optimal control of photoelectron emission by realistic waveforms

J. Solanpää,[1,*], M. F. Ciappina,[2,3] and E. Räsänen[1]
[1]*Laboratory of Physics, Tampere University of Technology, Tampere FI-33101, Finland*
[2]*Max-Planck-Institut für Quantenoptik, Garching D-85748, Germany*
[3]*Institute of Physics of the ASCR, ELI-Beamlines/HiLASE/PALS, Na Slovance 2, 182 21 Prague, Czech Republic*

(Received 4 November 2016; Accepted 27 March 2017)

Recent experimental techniques in multicolor waveform synthesis allow the temporal shaping of strong femtosecond laser pulses with applications in the control of quantum mechanical processes in atoms, molecules, and nanostructures. Prediction of the shapes of the optimal waveforms can be done computationally using quantum optimal control theory (QOCT). In this work we demonstrate the control of above-threshold photoemission of one-dimensional hydrogen model with pulses feasible for experimental waveform synthesis. By mixing different spectral channels and thus lowering the intensity requirements for individual channels, the resulting optimal pulses can extend the cutoff energies by at least up to 50% and bring up the electron yield by several orders of magnitude. Insights into the electron dynamics for optimized photoelectron emission are obtained with a semiclassical two-step model.
DOI: 10.1080/09500340.2017.1317857

1. Introduction

When atoms, molecules, and bulk matter interact with strong and short laser fields new and peculiar phenomena appear, configuring what nowadays we know as attosecond physics or attosecond science [1]. In particular, the so-called above-threshold ionization (ATI) has been a particularly appealing subject in both experimental and theoretical physics. In ATI, an atomic or molecular electron is pulled out to the continuum by the action of the laser electric field and, after a subsequent dynamics, which includes the recollision mechanism, either the electron energy or several components of the electron momentum are experimentally measured (see e.g. [2] for a review about both experimental and theoretical developments). The ATI phenomenon was first observed more than three decades ago by Agostini et al. [3], and it was established that it occurs when an atom or molecule absorbs more photons than the minimum threshold number required to ionize it, hence the name ATI, leaving the leftover energy being converted to the kinetic energy of the released electron.

With the constant advances in laser technology, it is routine today to generate few-cycle pulses, i.e., laser pulses whose electric field comprises only one or two complete optical cycles, which find an ample range of applications in basic science, for instance, in the control of chemical reactions and molecular motion [4, 5]. From a technological viewpoint they are the workhorses in the generation of high order harmonics in atoms and molecules and the creation of isolated extreme ultraviolet

(XUV) pulses [6, 7]. In a few-cycle laser pulse the electric field can be characterized by its duration in time and by the so-called carrier-envelope phase (CEP), defined as the relative phase between the maximum of the pulse envelope and the nearest maximum of the carrier wave. When compared with a multicycle pulse, the electric field of few-cycle pulses changes dramatically its temporal shape with the CEP [8, 9]. From a more fundamental viewpoint, it has been experimentally observed that the CEP plays an instrumental role in high-order-harmonic generation [10], the emission direction of electrons from atoms [11], and in the yield of nonsequential double ionization [12]. Currently, investigations of ATI generated by few-cycle driving laser pulses have attracted so much interest due to the strong sensitivity of the energy and angle-resolved 2D photoelectron spectra to the absolute value of the CEP [13, 14]. Consequently, this feature of the laser ionized electron renders the ATI phenomenon as a very valuable tool for few-cycle laser pulse characterization. One of the most widely used techniques to characterize the CEP of a few-cycle laser pulse is to measure the so-called backward-forward asymmetry of the energy-resolved ATI spectrum, from which the absolute value of the CEP can be directly inferred [11]. In addition, nothing but the high-energy region of the photoelectron spectra appears to be the most sensitive one to the absolute CEP and, consequently, electrons with large kinetic energy are needed in order to characterize it [15].

Recent experiments using plasmon field enhancement have demonstrated that the high-order harmonic generation (HHG) cutoff and ATI photoelectron spectra could be extended further [16, 17]. Plasmonic-enhanced fields appear when a metal nanostructure or nanoparticle is illuminated by a short laser pulse. These fields are spatially inhomogeneous in a nanometric region, due to the strong confinement of the so-called plasmonics 'hot spots' and the distortion of the electric field by the surface plasmons induced in the nanosystem. One should note, however, that a recent controversy about the outcome of the experiments of Ref. [16] has arisen [18–20]. Consequently, alternative systems to the metal bow-tie-shaped nanostructures have appeared [21]. From a theoretical viewpoint, however, these experiments have sparked an intense and constant activity [22–44].

An step forward would be to use multicolor waveforms or field transients to drive the ATI phenomenon (for a recent article see e.g. Ref. [45]). These laser sources present unique characteristics, as noticeable sub-fs changes in the laser electric field [46, 47]. In addition, a large set of parameters is available to control, with great precision, the shape of the laser electric field. For instance, by manipulating both the amplitude and relative phases of the different *colors*, it would be possible to tailor the laser electric field with an attosecond precision [48].

Clever design of the shape of the laser electric field gives us the ability to control quantum mechanical (QM) processes. Prediction of the parameters for the waveforms can be achieved either via genetic evolution of the laser parameters in learning-loop experiments (see, e.g., Ref. [49] and references therein) or via *quantum optimal control*

theory (QOCT) simulations [49–52], where computational tools are used to predict the optimal pulse shapes for a given *target*, i.e., the desired outcome of the QM process. QOCT has been successfully used to control, e.g., ultrafast strong-field phenomena such as high-harmonic generation [53–55], strong-field ionization [56–59], and photoelectron emission [45].

However, in ultrafast strong-field physics, there have yet to be any experiments using laser pulses designed with QOCT. This is in contrast to many other fields within the QOCT community (see, e.g., Ref. [60] and the references therein). The reason may be, in part, due to the fact that several previous studies using QOCT in controlling strong-field phenomena produce laser pulses that are not fully compatible with experimental multicolor waveform synthesis despite several advances in incorporating constraints to QOCT (see, e.g., Refs. [52, 61] and the references therein). A recent work by *B. Bódi et al.* in Ref. [62] brings QOCT within ultrafast strong-field physics towards predicting experimentally feasible waveforms. In their work, the total laser electric field is a superposition of four predefined pulses of different colors (channels) that are obtained from experimental setups. This computational scheme, simulating a single multicolor waveform synthesizer, allows experimental compatibility, in principle.

As in the work by *B. Bódi et al.*, we present the optimizable pulse as a superposition of component pulses (channels), but do not address any specific light-field synthesizer. Hence, instead of using channel information from an existing experimental setup, each channel is represented by a single-frequency carrier wave with a Gaussian envelope. This analytical basis has several advantages: while providing experimentally feasible pulses, we can (1) easily change the channel specifications and (2) use gradient-based optimization methods if desired. We note that QOCT-schemes representing the field in a basis have been proposed and applied earlier to a variety of systems [63–68]. In contrast to previous methods, in our scheme we aim at compatibility with modern waveform synthesizers for ultrashort strong-field physics. First, we use the most natural analytical basis for pulses produced for such systems, and second, we add CEP as an optimizable quantity. With respect to physical constraints, our method can enforce arbitrary constraints for the total laser electric field as well as the component channels.

In the next Sections we describe the scheme and use it to optimize multicolor waveforms or field transients for different *targets*, namely the photoelectron yield and/or the ATI energy cutoff. The ultimate goal is to push the limits in the energy conversion, in the sense to reach as energetic electrons as possible, with a given input laser energy.

2. Optimization scheme

We describe the total electric field as a superposition of N channels represented as ultrashort pulses consisting of a single-frequency carrier wave with a gaussian envelope.

Each of the channels has their own amplitude A_i, carrier frequency ω_i, center time τ_i, carrier-envelope phase (CEP) ϕ_i, and duration σ_i, i.e.,

$$\epsilon[\mathbf{u}](t) = \sum_{i=1}^{N} A_i \cos\left[\omega_i(t-\tau_i)+\phi_i\right] \exp\left[-\ln(2)\,(t-\tau_i)^2/\sigma_i^2\right], \tag{1}$$

where $\mathbf{u}$ denotes the optimizable parameters. We can choose at will the number of component pulses N, and which parameters are kept fixed and which are optimized. Note that chirp, and in higher dimensions also polarization, can be easily added to the representation as optimizable parameters. The total field of Eq. (1) always satisfies $\epsilon(-\infty) = \epsilon(\infty) = 0$ and $\left|\int \epsilon(t)\,\mathrm{d}t\right| \approx 0$ whenever $\sigma_i \gtrsim 200$ a.u. for wavelengths < 2 μm; If $\sigma_i \lesssim 200$ a.u., one would need to add $\int \epsilon(t)\,\mathrm{d}t = 0$ as a global optimization constraint to have the optimized pulses strictly conform to Maxwell's equations, although we omit this in the following demonstrations.

We test our scheme in a one-dimensional (1D) hydrogen-like atom, but full 3D approaches and multielectronic systems within the single active electron approximation (SAE) could be used. The pulses are optimized to maximize the photoelectron yield and energy. We take up to $N = 3$ channels, each with a fixed frequency and duration. Thus, the optimizable parameters are the amplitudes A, CEPs ϕ, and time-delays via τs in line with modern waveform synthesis experiments (see, e.g., Refs. [47, 69, 70]). The 1D Hamiltonian of our system can be written as

$$\hat{H} = \frac{\hat{p}^2}{2} + V(\hat{x}) + \hat{x}\epsilon[\mathbf{u}](t), \tag{2}$$

where $V(x) = -1/\sqrt{x^2+1}$ is the soft Coulomb potential. We represent the system on a real space grid of length $L \approx 530$ nm (10,000 a.u.) with a spacing $\Delta x \approx 13$ pm (0.25 a.u.).

The time propagation begins from the ground state, and the time evolution is calculated by the exponential mid-point rule with time step $\Delta t \approx 1.2$ as, i.e., $\hat{U}(t \to t+\Delta t) \approx \exp\left[-i\Delta t \hat{H}(t+\Delta t/2)\right]$. Action of the matrix exponential on the state, i.e., $\hat{U}|\psi\rangle$, is done using the new algorithm from Ref. [71] as implemented in *SciPy* [72].

To target the photoelectron spectrum (PES), we optimize the integral of the PES over some energy range $[E_a, E_b]$ (see Ref. [53] for a similar target in HHG). Calculation of the PES is done according to Ref [73], i.e., we calculate the PES at the end of the pulse using an energy window technique. This target functional can be written as

$$G[\mathbf{u}] = \langle \Psi[\mathbf{u}](T)|\hat{O}|\Psi[\mathbf{u}](T)\rangle, \tag{3}$$

where

$$\hat{O} = \int_{E_a}^{E_b} \mathrm{d}E\ \mathtt{PES}(E) = \int_{E_a}^{E_b} \mathrm{d}E\ \frac{\gamma^4}{\left(\hat{H}_0 - E\right)^4 + \gamma^4}, \tag{4}$$

and γ is half of the energy resolution ($\Delta E \approx 0.6$ eV for the cases studied in the present work).

Optimization of this target can be achieved in two ways. First, we can increase the yield of the photoelectrons (larger integrand values), or second, as the PES has a sharp cutoff, we can extend the cutoff energy (provided that E_b has been set large enough). In practice, the optimal pulses typically fill both these goals, i.e., we get increase both in the photoelectron yield and in the cutoff energy.

These ingredients are already enough for gradient-free optimization schemes, which we will use in the rest of the paper. Calculation of the gradient of Eq. (3) for the pulse representation in Eq. (1) would be trivial following, e.g., Ref. [52]. However, we found that calculation of an auxiliary wavefunction called the *costate*, at the end of the pulse, was numerically challenging for the chosen target operator. For other methods of calculating the PES it could be easier to obtain the costate (and hence the gradient). For instance, calculating the PES as a projection to plane waves would result in the costate at the end of the pulse being just a band-pass filtered final wavefunction.

Optimization of the target is done with *Multi-Level Single-Linkage* (MLSL) global optimizer [74]. The MLSL algorithm conducts a series of local optimization searches within a bounded domain while avoiding (1) repeated searches of previously found local maxima and (2) starting local searches near the search space boundaries [74, 75]. For local optimization, we employ a gradient free algorithm called *Bound Optimization by Quadratic Approximation* (BOBYQA [76, 77]) [78] which, together with MLSL, allows us to bound the optimization variables. In particular, the amplitude of each channel is capped to $A \in [0.03, 0.13]$ a.u., the full-width half maximum (FWHM) to $\sigma \in [3.6, 9.7]$ fs and the maximum time-delay between channels to ~ 9.7 fs. The pulse constraints (fluence and peak intensity) are nonlinear in the search space and can not be handled by bounds for the optimization variables. These global constraints are enforced via the augmented lagrangian technique [79, 80]. For the optimization algorithms, we use the *nlopt* library [75] implementations.

The optimization routine begins from a random pulse configuration usually giving low yield and small cutoff energies for the PES. During the optimization, the algorithms find several locally optimal pulses for our target. Here we show the best of the locally optimal pulses and compare it with:

i) a commonly available reference pulse with carrier wavelength of 800 nm with the same fluence and peak intensity as the optimized pulse and

ii) the separate channels of the optimized pulse.

3. Optimization results

The easiest way to increase the photoelectron energies would be to increase the peak intensity or the wavelength of the driving laser pulse. There is, however, a limit

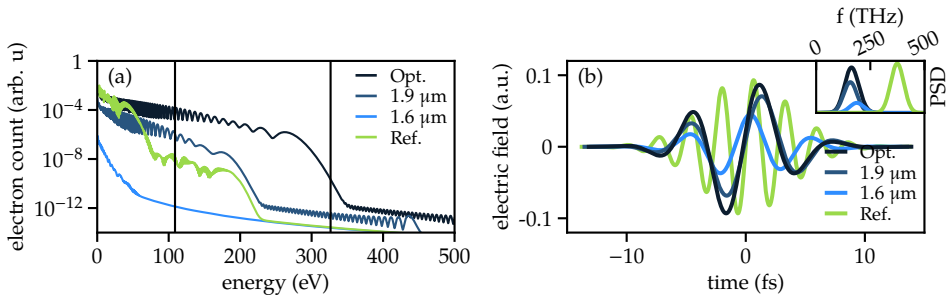

Figure 1: (a) Optimized photoelectron spectrum (PES) with a two-channel pulse (black) demonstrates up to 3 orders of magnitude increase in the yield and over 100 eV extension of the cutoff energy compared to the nm single-channel (800) reference pulse [green (light gray) curve], and single channels of the optimal pulse [blue lines]. (b) The optimized pulse (black) is composed of two channels (dark blue and blue), and the reference pulse (green) has the same peak intensity and fluence as the optimized pulse, but different spectral range. The power spectral distributions of the pulses are shown in the inset.

to the dominant wavelength of strong femtosecond laser pulses, and currently, in experimental multicolor waveform synthesis, it is easier to distribute energy between different channels than to concentrate it all to a single channel [69].

Hence, we begin by setting up two spectral channels, the simplest possible multicolor waveform configuration. The channels have partially overlapping spectral shapes with central frequencies corresponding to wavelengths of 1.6 μm and 1.9 μm. Furthermore, the peak laser electric field is constrained below 0.09 a.u. (corresponding to a peak intensity $\approx 2.8 \cdot 10^{14}$ W/cm^2), and the fluence to 3 a.u., but it turns out that the peak field constraint is more restricting than the fluence constraint in this case. The targeted energy range is approximately from $E_a = 110$ eV (~ 4 a.u.) to $E_b = 330$ eV (~ 12 a.u.) shown as vertical lines together with the spectra in Fig. 1(a).

The optimized spectrum [black curve in Fig. 1(a)] has a cutoff energy of ~ 300 eV. This is ~ 50 % more than for the 1.9 μm channel of the optimized pulse (dark blue curve), and in addition, the yield is increased by up to 3 orders of magnitude. If we compare the optimized spectrum to what is obtained for a commonly available 800 nm pulse (green curve), we observe even more dramatic enhancements.

The optimized pulse [black line in Fig. 1(b)] mixes the 1.6 μm and 1.9 μm channels roughly in proportions of one to three when comparing their respective intensities. Essentially, the optimization algorithm finds the correct CEP and time-delay for each channel in order to increase the peak intensity and fluence of the total field compared to the 1.9 μm channel only. This achieves the desired effect, i.e., the enhancement of

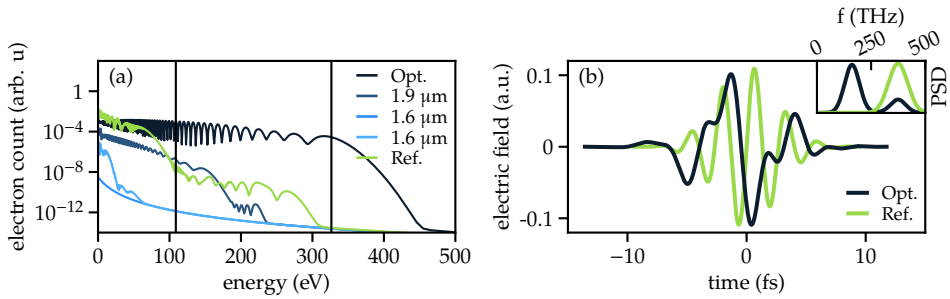

Figure 2: (a) Optimized photoelectron spectrum (PES) with a three-channel pulse (black) shows a yield enhancement up to 6 orders of magnitude and a dramatic cutoff extension (more than 100 eV) compared to the single-channel (800 nm) reference pulse (green), and single channels of the optimal pulse (blue lines). (b) The optimization changes the dominant spectral contribution to lower frequencies as seen from the power spectral densities (PSDs) of the laser pulses in the inset, and it also increases the duration of the major cycle of the optimized pulse.

the PES without concentrating all the pulse energy to a single channel.

The pulse shapes allowed by the two-channels are quite restricted, and we can increase the degrees of freedom by adding in another spectral channel. The three-channel optimization is conducted with central frequencies of the channels corresponding to wavelengths 0.8 μm, 1.6 μm, and 1.9 μm, and we also increase the peak field constraint to 0.11 a.u. The target remains the same as for two-channel optimization, i.e., from $E_a = 110$ eV to $E_b = 330$ eV. Figure 2(a) shows the optimized PES (black) and compares it to the reference spectrum of the 800 nm pulse (green) and the spectra obtained for single channels of the optimized pulse (blue lines). The optimal pulse increases the yield up to six orders of magnitude and extends the cutoff energy by over 100 eV, and as in the two-channel case, the optimal pulse wins over the single channel results.

The optimal three-channel pulse [black line in Fig. 2(b)] mixes the 0.8 μm, 1.6 μm, and 1.9 μm channels in (intensity) proportions of around 5-1-11. This lowers the intensity requirement for the long-wavelength channels as in the two-channel setup described above. It is of interest to note that the changes in the PES are due to mixing lower-wavelength channels, channels which alone give spectra with much lower energy cutoffs.

One of the advantages of the 1D models is the possibility to scrutinize the time and spatial electron dynamics in a direct way. To this end in Fig. 3(a) we show the electron density $|\Psi(x,t)|^2$, where $\Psi(x,t)$ is the spatio-temporal electron wavefunction, for the optimal three-channel laser pulse used in Fig. 3(b). The reason why such a simple pulse optimizes the spectrum is that the last dominant cycle in the laser pulse packs as

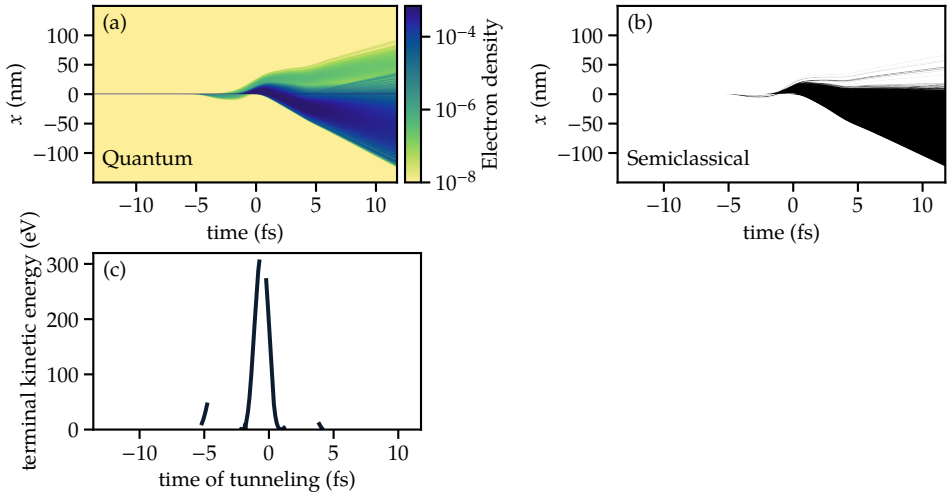

Figure 3: (a) Electron density corresponding to the optimized 3-channel pulse in Fig. 3, (b) 10^6 corresponding (semi)classical trajectories, and (c) the terminal kinetic energy as a function of the time of tunneling.

much energy in the ejected electron wavepacket as possible. To better illustrate this idea, we employ a semiclassical two-step model similar to the three-step model used in Ref. [53].

An ensemble 10^6 trajectories is simulated as follows:

1. The tunneling times (start times of the trajectories) t_0 are randomized following the exponential tunneling rate [81–85]

$$w\left(t_0\right) \sim \exp\left\{-\left[2\left(2I_p\right)^{3/2}\right] / \left[3|\epsilon(t_0)|\right]\right\}, \tag{5}$$

   where $I_p = 0.669$ a.u. is the ionization potential of our system.

2. The trajectories start with zero velocity at the tunnel exit, which is located at the classical turning point on the farther side of the tunneling barrier.

3. After tunneling, the trajectories are propagated classically, i.e., following Newton's equations, using the 8th order Dormand & Prince algorithm with adaptive step size control (see e.g. [86]).

Figure 3(b) shows all the 10^6 trajectories calculated using the semiclassical model. The trajectories start around peak field strenghts [see the black line in Fig. 2(b)], and most of them end up at $x < 0$ at the end of the simulation (the uniform black area). We

see a clear correspondence to the QM simulation in Fig. 3(a): quantum mechanically high-density areas are filled with semiclassical trajectories whereas QM low-density areas have only few trajectories. By increasing the ensemble size by a few orders of magnitude, better agreement with the QM low-density region could be obtained.

In the semiclassical model, the maximum kinetic energy is obtained for tunneling events between the two dominant subcycles of the pulse i.e., slightly before $t_0 = 0$ as shown in Fig. 3(c) illustrating the terminal kinetic energy as a function of the tunneling time of the trajectory. For the trajectories tunneling out near $t_0 = 0$, the semiclassical model yields the maximal terminal kinetic energy of 315 eV, i.e., at the beginning of the cutoff of the optimized QM spectrum of Fig. 2(a). The electron trajectories that tunnel out near the field minimum at $t_0 \approx 0$ feel only the full effect of the later dominant half cycle of the pulse, thus contributing to the cutoff region of the PES. An electron tunneling out earlier would be slowed down by the previous half-cycle, and an electron tunneling out later would not obtain the maximum energy from the latter half-cycle.

4. Summary

We have presented a computational optimal control scheme that composes experimentally feasible multicolor waveforms from analytical pulse components (channels). As a case study we apply the scheme to the optimization of photoelectron spectra in a one-dimensional hydrogen-like system. The scheme provides substantial yield enhancement and cutoff extension compared to single 800 nm pulses with the same peak intensity and fluence or the component channels of the optimized pulse. By mixing a few different spectral channels, the proposed method decreases the need for high intensities in single spectral channels. Simultaneously, the scheme provides significant enhancements in the photoelectron spectrum yield and cutoff. In addition, we have shown that the physical working mechanisms behind the optimal pulses can be inspected with simple semiclassical models.

With the chosen channel configurations and target energies the scheme already provides photoelectrons with ~ 0.5 keV energies. By suitable modifications in the channel configuration and pulse constraints, the scheme could provide a way to generate ultrashort electron pulses with sufficient yield even in the keV regime. Such electron pulses can be used for diffraction experiments, and could, e.g., provide improvements to the celebrated laser-induced electron diffraction (LIED) technique (see, e.g., Refs. [87, 88]) by increasing its spatial resolution.

In addition, an extension of our optimal control scheme with realistic waveforms to 3D and many-electron systems is straightforward. The scheme can be modified to use most of the existing optimization algorithms to account for different search space landscapes in other systems, and it can be readily be implemented in existing optimal control software or as an external module to all state-of-the-art software packages for single- or many-electron simulations. This provides straightforward access to a

multitude of different applications including, e.g., optimization of high-harmonic generation, atomic transitions between states, and electron dynamics in molecular and nanoscale devices.

Acknowledgements

We thank Dr. Arne Senftleben for insightful discussions. This work was supported by the project ELI–Extreme Light Infrastructure–phase 2 (CZ.02.1.01/0.0/-0.0/15_008/0000162) from European Regional Development Fund and by the Academy of Finland (project no. 126205) and COST Action CM1204 (XLIC). We also acknowledge CSC the Finnish IT Center for Science for computational resources. Several Python-extensions [72, 89–92] were used for the simulation and analysis.

[1] See, e.g., F. Krausz and M. Ivanov, *Attosecond physics*, Rev. Mod. Phys. **81**, 163 (2009) and the references therein.

[2] D. B. Milosević, G. G. Paulus, D. Bauer, and W. Becker, *Above-threshold ionization by few-cycle pulses*, J. Phys. B: At. Mol. Opt. Phys. **39**, R203 (2006).

[3] P. Agostini, F. Fabre, G. Mainfray, G. Petite, and N. K. Rahman, *Free-Free Transitions Following Six-Photon Ionization of Xenon Atoms*, Phys. Rev. Lett. **42**, 1127 (1979).

[4] M. Schnürer et al., *Femtosecond X-Ray Fluorescence*, Phys. Rev. Lett. **85**, 3392 (2000).

[5] P. von den Hoff, I. Znakovskaya, M. Kling, and R. de Vivie-Riedle, *Attosecond control of the dissociative ionization via electron localization: A comparison between D_2 and CO*, Chem. Phys. **366**, 139 (2009).

[6] F. Ferrari et al., *High-energy isolated attosecond pulses generated by above-saturation few-cycle fields*, Nat. Phot. **4**, 975 (2010).

[7] M. Schultze et al., *Powerful 170-attosecond XUV pulses generated with few-cycle laser pulses and broadband multilayer optics*, New J. Phys. **9**, 243 (2007).

[8] T. Wittmann et al., *Single-shot carrier–envelope phase measurement of few-cycle laser pulses*, Nat. Phys. **5**, 357 EP (2009).

[9] M. F. Kling et al., *Imaging of carrier-envelope phase effects in above-threshold ionization with intense few-cycle laser fields*, New J. Phys. **10**, 025024 (2008).

[10] M. Nisoli et al., *Effects of Carrier-Envelope Phase Differences of Few-Optical-Cycle Light Pulses in Single-Shot High-Order-Harmonic Spectra*, Phys. Rev. Lett. **91**, 213905 (2003).

[11] G. G. Paulus et al., *Absolute-phase phenomena in photoionization with few-cycle laser pulses*, Nature **414**, 182 (2001).

[12] X. Liu et al., *Nonsequential Double Ionization at the Single-Optical-Cycle Limit*, Phys. Rev. Lett. **93**, 263001 (2004).

[13] A. Sayler et al., *Waveform Characterization of Few-Cycle Laser Pulses in Real-Time using Above-Threshold Ionization*, in CLEO/Europe and EQEC 2011 (2011), p. 1.

[14] A. M. Sayler, T. Rathje, W. Müller, K. Rühle, R. Kienberger, and G. G. Paulus, *Precise, real-time, every-single-shot, carrier-envelope phase measurement of ultrashort laser pulses*, Opt. Lett. **36**, 1 (2011).

[15] G. G. Paulus et al., *Measurement of the Phase of Few-Cycle Laser Pulses*, Phys. Rev. Lett. **91**, 253004 (2003).

[16] S. Kim, J. Jin, Y.-J. Kim, I.-Y. Park, Y. Kim, and S.-W. Kim, *High-harmonic generation by resonant plasmon field enhancement*, Nature **453**, 757 (2008).

[17] S. Zherebtsov et al., *Controlled near-field enhanced electron acceleration from dielectric nanospheres with intense few-cycle laser fields*, Nat. Phys. **7**, 656 (2011).

[18] M. Sivis, M. Duwe, B. Abel, and C. Ropers, *Nanostructure-enhanced atomic line emission*, Nature **485**, E1 (2012).

[19] S. Kim, J. Jin, Y.-J. Kim, I.-Y. Park, Y. Kim, and S.-W. Kim, *Kim et al. reply*, Nature **485**, E1 (2012).

[20] M. Sivis, M. Duwe, B. Abel, and C. Ropers, *Extreme-ultraviolet light generation in plasmonic nanostructures*, Nat. Phys. **9**, 304 (2013).

[21] I.-Y. Park et al., *Plasmonic generation of ultrashort extreme-ultraviolet light pulses*, Nat. Phot. **5**, 677 (2011).

[22] A. Husakou, S.-J. Im, and J. Herrmann, *Theory of plasmon-enhanced high-order harmonic generation in the vicinity of metal nanostructures in noble gases*, Phys. Rev. A **83**, 043839 (2011).

[23] I. Yavuz, E. Bleda, Z. Altun, and T. Topcu, *Generation of a broadband xuv continuum in high-order-harmonic generation by spatially inhomogeneous fields*, Phys. Rev. A **85**, 013416 (2012).

[24] M. Ciappina, J. Biegert, R. Quidant, and M. Lewenstein, *High-order-harmonic generation from inhomogeneous fields*, Phys. Rev. A **85**, 033828 (2012).

[25] I. Yavuz, *Gas population effects in harmonic emission by plasmonic fields*, Phys. Rev. A **87**, 053815 (2013).

[26] I. Yavuz, Y. Tikman, and A. Z., *High-order-harmonic generation from H_2^+ molecular ions near plasmon-enhanced laser fields*, Phys. Rev. A **92**, 023413 (2015).

[27] M. F. Ciappina, S. S. Aćimović, T. Shaaran, J. Biegert, R. Quidant, and M. Lewenstein, *Enhancement of high harmonic generation by confining electron motion in plasmonic nanostrutures*, Opt. Exp. **20**, 26261 (2012).

[28] T. Shaaran, M. F. Ciappina, and M. Lewenstein, *Quantum-orbit analysis of high-order-harmonic generation by resonant plasmon field enhancement*, Phys. Rev. A **86**, 023408 (2012).

[29] M. F. Ciappina, J. A. Pérez-Hernández, T. Shaaran, J. Biegert, R. Quidant, and M. Lewenstein, *Above-threshold ionization by few-cycle spatially inhomogeneous fields*, Phys. Rev. A **86**, 023413 (2012).

[30] T. Shaaran, M. F. Ciappina, and M. Lewenstein, *Estimating the plasmonic field enhancement using high-order harmonic generation: the role of the field inhomogeneity*, J. Mod. Opt. **86**, 1634 (2012).

[31] J. A. Pérez-Hernández, M. F. Ciappina, M. Lewenstein, L. Roso, and A. Zaïr, *Beyond Carbon K-Edge Harmonic Emission Using a Spatial and Temporal Synthesized Laser Field*, Phys. Rev. Lett. **110**, 053001 (2013).

[32] M. F. Ciappina, J. A. Pérez-Hernández, T. Shaaran, L. Roso, and M. Lewenstein, *Electron-momentum distributions and photoelectron spectra of atoms driven by an intense spatially inhomogeneous field*, Phys. Rev. A **87**, 063833 (2013).

[33] T. Shaaran et al., *High-order-harmonic generation by enhanced plasmonic near-fields in metal nanoparticles*, Phys. Rev. A **87**, 041402(R) (2013).

[34] M. F. Ciappina, T. Shaaran, and M. Lewenstein, *High order harmonic generation in noble gases using plasmonic field enhancement*, Ann. Phys. **525**, 97 (2013).

[35] T. Shaaran, M. F. Ciappina, and M. Lewenstein, *Quantum-orbit analysis of above-threshold ionization driven by an intense spatially inhomogeneous field*, Phys. Rev. A **87**, 053415 (2013).

[36] M. F. Ciappina et al., *High energy photoelectron emission from gases using plasmonic enhanced near-fields*, Las. Phys. Lett. **10**, 105302 (2013).

[37] M. F. Ciappina, J. A. Pérez-Hernández, T. Shaaran, M. Lewenstein, M. Krüger, and P. Hommelhoff, *High-order harmonic generation driven by metal nanotip photoemission: theory and simulations*, Phys. Rev. A **89**, 013409 (2014).

[38] M. Ciappina, J. A. Pérez-Hernández, T. Shaaran, and M. Lewenstein, *Coherent XUV generation driven by sharp metal tips photoemission*, Eur. Phys. J. D **68**, 172 (2014).

[39] M. F. Ciappina, J. A. Pérez-Hernández, and M. Lewenstein, *ClassSTRONG: Classical simulations of strong field processes*, Comp. Phys. Comm. **185**, 398 (2015).

[40] M. F. Ciappina, J. A. Pérez-Hernández, L. Roso, A. Zaïr, and M. Lewenstein, *High-order harmonic generation driven by plasmonic fields: a new route towards the generation of UV and XUV photons?*, J. Phys.: Conf. Ser. **601**, 012001 (2015).

[41] A. Husakou, F. Kelkensberg, J. Herrmann, and M. J. J. Vrakking, *Polarization gating and circularly-polarized high harmonic generation using plasmonic enhancement in metal nanostructures*, Opt. Express **19**, 25346 (2011).

[42] A. Husakou and J. Herrmann, *Quasi-phase-matched high-harmonic generation in composites of metal nanoparticles and a noble gas*, Phys. Rev. A **90**, 023831 (2014).

[43] Y. Tikman, I. Yavuz, M. F. Ciappina, A. Chacón, Z. Altun, and M. Lewenstein, *High-order-harmonic generation from Rydberg atoms driven by plasmon-enhanced laser fields*, Phys. Rev. A **93**, 023410 (2016).

[44] I. Yavuz, M. F. Ciappina, A. Chacón, Z. Altun, M. F. Kling, and M. Lewenstein, *Controlling electron localization in H_2^+ by intense plasmon-enhanced laser fields*, Phys. Rev. A **93**, 033404 (2016).

[45] R. E. Goetz, A. Karamatskou, R. Santra, and C. P. Koch, *Quantum optimal control of photoelectron spectra and angular distributions*, Phys. Rev. A **93**, 013413 (2016).

[46] E. Goulielmakis et al., *Single-cycle nonlinear optics*, Science **320**, 1614 (2008).

[47] A. Wirth et al., *Synthesized Light Transients*, Science **334**, 195 (2011).

[48] H. Fattahi et al., *Third-generation femtosecond technology*, Optica **1**, 45 (2014).

[49] C. Brif, R. Chakrabarti, and H. Rabitz, *Control of quantum phenomena: past, present and future*, New J. Phys. **12**, 075008 (2010).

[50] A. P. Peirce, M. A. Dahleh, and H. Rabitz, *Optimal control of quantum-mechanical systems: Existence, numerical approximation, and applications*, Phys. Rev. A **37**, 4950 (1988).

[51] R. Kosloff, S. Rice, P. Gaspard, S. Tersigni, and D. Tannor, *Wavepacket dancing: Achieving chemical selectivity by shaping light pulses*, Chem. Phys. **139**, 201 (1989).

[52] J. Werschnik and E. K. U. Gross, *Quantum optimal control theory*, J. Phys. B **40**, R175 (2007).

[53] J. Solanpää, J. A. Budagosky, N. I. Shvetsov-Shilovski, A. Castro, A. Rubio, and E. Räsänen, *Optimal control of high-harmonic generation by intense few-cycle pulses*, Phys. Rev. A **90**, 053402 (2014).

[54] A. Castro, A. Rubio, and E. K. U. Gross, *Enhancing and controlling single-atom high-harmonic generation spectra: a time-dependent density-functional scheme*, Eur. Phys. J B **88**, 191 (2015).

[55] Y. Chou, P.-C. Li, T.-S. Ho, and S.-I. Chu, *Optimal control of high-order harmonics for the generation of an isolated ultrashort attosecond pulse with two-color midinfrared laser fields*, Phys. Rev. A **91**, 063408 (2015).

[56] A. Castro, E. Räsänen, A. Rubio, and E. K. U. Gross, *Femtosecond laser pulse shaping for enhanced ionization*, Europhys. Lett. **87**, 53001 (2009).

[57] M. Hellgren, E. Räsänen, and E. K. U. Gross, *Optimal control of strong-field ionization with time-dependent density-functional theory*, Phys. Rev. A **88**, 013414 (2013).

[58] E. Räsänen and L. B. Madsen, *Strong-field-ionization suppression by light-field control*, Phys. Rev. A **86**, 033426 (2012).

[59] N. I. Shvetsov-Shilovski, L. B. Madsen, and E. Räsänen, *Suppression of strong-field ionization by optimal pulse shaping: Application to hydrogen and the hydrogen molecular ion*, Phys. Rev. A **91**, 023425 (2015).

[60] See, e.g., S. J. Glaser et al., *Training Schrödinger's cat: quantum optimal control*, Eur. Phys. J. D **69**, 279 (2015) and the references therein.

[61] D. Sugny, S. Vranckx, M. Ndong, O. Atabek, and M. Desouter-Lecomte, *External constraints on optimal control strategies in molecular orientation and photofragmentation: role of zero-area fields*, J. Mod. Opt. **61**, 816 (2014).

[62] E. Balogh, B. Bódi, V. Tosa, E. Goulielmakis, K. Varjú, and P. Dombi, *Genetic optimization of attosecond-pulse generation in light-field synthesizers*, Phys. Rev. A **90**, 023855 (2014).

[63] R. D. Guerrero, C. A. Arango, and A. Reyes, *Analytical optimal pulse shapes obtained with the aid of genetic algorithms*, J. Chem. Phys. **143**, 124108 (2015).

[64] K. Kormann, S. Holmgren, and H. O. Karlsson, *A Fourier-Coefficient Based Solution of an Optimal Control Problem in Quantum Chemistry*, J. Optimiz. Theory. App. **147**, 491 (2010).

[65] T. Caneva, T. Calarco, and S. Montangero, *Chopped random-basis quantum optimization*, Phys. Rev. A **84**, 022326 (2011).

[66] N. Rach, M. M. Müller, T. Calarco, and S. Montangero, *Dressing the chopped-random-basis optimization: A bandwidth-limited access to the trap-free landscape*, Phys. Rev. A **92**, 062343 (2015).

[67] T. E. Skinner and N. I. Gershenzon, *Optimal control design of pulse shapes as analytic functions*, Journal of Magnetic Resonance **204**, 248 (2010).

[68] B. Bartels and F. Mintert, *Smooth optimal control with Floquet theory*, Phys. Rev. A **88**, 052315 (2013).

[69] H. Fattahi et al., *Third-generation femtosecond technology*, Optica **1**, 45 (2014).

[70] M. T. Hassan et al., *Optical attosecond pulses and tracking the nonlinear response of bound electrons*, Nature **530**, 66 (2016).

[71] A. H. Al-Mohy and N. J. Higham, *Computing the Action of the Matrix Exponential, with an Application to Exponential Integrators*, SIAM J. Sci. Comput. **33**, 488 (2011).

[72] E. Jones, T. Oliphant, P. Peterson, et al., *SciPy: Open source scientific tools for Python*, (2001) `http://www.scipy.org/` (visited on 11/19/2018).

[73] K. J. Schafer and K. C. Kulander, *Energy analysis of time-dependent wave functions: Application to above-threshold ionization*, Phys. Rev. A **42**, 5794 (1990).

[74] A. H. G. R. Kan and G. T. Timmer, *Stochastic global optimization methods*, Math. Prog. **39**, 27 (1987).

[75] S. G. Johnson, *The NLopt nonlinear-optimization package*, `http://ab-initio.mit.edu/nlopt` (visited on 03/21/2019).

[76] Z. Zhang, *Software by Professor M. J. D. Powell*, `http://mat.uc.pt/~zhang/software.html` (visited on 2016).

[77] M. J. D. Powell, *BOBYQA source code*, `http://mat.uc.pt/~zhang/software.html` (visited on 2016).

[78] M. J. D. Powell, *The BOBYQA algorithm for bound constrained optimization without derivatives*, tech. rep. (Univ. of Cambridge, Dept. of Appl. Math. and Theor. Phys., 2009).

[79] A. R. Conn, N. I. M. Gould, and P. L. Toint, *A globally convergent augmented Lagrangian algorithm for optimization with general constraints and simple bounds*, SIAM J. Numer. Anal. **28**, 545 (1991).

[80] E. G. Birgin and J. M. Martínez, *Improving ultimate convergence of an augmented Lagrangian method*, Optim. Method. Softw. **23**, 177 (2008).

[81] A. Perelomov, V. Popov, and M. Terent'ev, *Ionization of Atoms in an Alternating Electric Field*, Zh. Eksp. Teor. Fiz. **50**, 1393 (1966).

[82] A. M. Perelomov and V. S. Popov, *IONIZATION OF ATOMS IN AN ALTERNATING ELECTRICAL FIELD. III*, J. Exptl. Theoret. Phys. **52**, 512 (1967).

[83] M. Ammosov, N. Delone, and V. Krainov, *Tunnel ionization of complex atoms and of atomic ions in an alternating electromagnetic field*, Zh. Eksp. Teor. Fiz. **91**, 2008 (1986).

[84] M. Ammosov, N. Delone, and V. Krainov, *Tunnel ionization of complex atoms and of atomic ions in an alternating electromagnetic field*, J. Exptl. Theoret. Phys. **91**, 2008 (1986).

[85] N. B. Delone and V. P. Krainov, *Energy and angular electron spectra for the tunnel ionization of atoms by strong low-frequency radiation*, J. Opt. Soc. Am. B **8**, 1207 (1991).

[86] E. Hairer, S. Nørsett, and G. Wanner, *Solving Ordinary Differential Equations I Nonstiff problems*, 2nd ed. (Springer, Berlin, DE, 1993).

[87] M. Meckel et al., *Laser-Induced Electron Tunneling and Diffraction*, Science **320**, 1478 (2008).

[88] M. G. Pullen et al., *Imaging an aligned polyatomic molecule with laser-induced electron diffraction*, Nat. Commun. **6**, 7262 (2015).

[89] F. Pérez and B. E. Granger, *IPython: A System for Interactive Scientific Computing*, Comput. Sci. Eng. **9**, 21 (2007).

[90] J. D. Hunter, *`Matplotlib`: A 2D Graphics Environment*, Computing in Science & Engineering **9**, 90 (2007).

[91] T. E. Oliphant, *Python for Scientific Computing*, Comput. Sci. Eng. **9**, 10 (2007).

[92] K. Thyng, *cmocean*, `https://github.com/matplotlib/cmocean` (visited on 2016).

Control of Rydberg state population with realistic femtosecond laser pulses

J. Solanpää, and E. Räsänen

Control of Rydberg state population with realistic femtosecond laser pulses
Phys. Rev. A **98**, 053422 (2018)

Control of Rydberg-state population with realistic femtosecond laser pulses

Janne Solanpää* and Esa Räsänen†
Laboratory of Physics, Tampere University of Technology, Tampere FI-33101, Finland

(Received 27 August 2018; published 15 November 2018)

We investigate computationally a method for ultrafast preparation of alkali-metal atoms in their Rydberg states using a three-dimensional model potential in the single active electron approximation. By optimizing laser pulse shapes that can be generated with modern waveform synthesizers, we propose pulses for controlling the population transfer from the ground state to a preselected set of Rydberg states. Dynamical processes under the optimized pulses are shown to be much more complicated than in the traditional optical two-photon preparation of Rydberg states.

DOI: 10.1103/PhysRevA.98.053422

I. INTRODUCTION

Rydberg states have been observed in numerous systems including, e.g., alkali-metal atoms [1] and larger systems such as water [2] and NO molecules [3]. Their features include long lifetimes [1], macroscopic extent of the electron wave function, and large dipole moments [4]. These features make them prime candidates for applications in, e.g., quantum information and quantum computing [5]. They are also of fundamental interest in the study of quantum chaos [6].

Experimental preparation of isolated alkali-metal atoms in Rydberg states can be achieved with two-photon absorption [4]. In rubidium, the successive absorption of 480- and 780-nm photons can excite the valence electron to a high-n Rydberg state with up to 80 % probability [7]. However, the two-photon absorption technique requires (i) tuning of the laser frequencies to the desired resonances and (ii) long irradiation durations to achieve reasonable yields [7].

Addressing these drawbacks may be achieved by using laser pulses with tailored temporal profiles. Standard techniques exist for the production of tailored femtosecond laser pulses [8], and their applicability has been demonstrated for controlling various dynamical phenomena in atoms such as above-threshold ionization [9,10] and high-order-harmonic generation [11–16,17(a),18]. Population and excitation control of atoms with femtosecond pulses has been studied to some extent both experimentally [17(b),19–21] and computationally [19,20]. However, control of the excitation to high-n Rydberg states using multicolor fields from modern light-field synthesizers has yet to be demonstrated.

In this work, we investigate the applicability of tailored femtosecond laser pulses to ultrafast excitation of alkali atoms to their Rydberg states. Using a computational optimization scheme similar to Ref. [10], we optimize a set of experimentally feasible pulse parameters and find optimal laser pulses that can achieve up to 20% population transfer to the targeted states. The pulse durations are typically less than a few dozen femtoseconds—demonstrating the possibility of ultrafast Rydberg state preparation.

This paper is organized as follows. In Sec. II, we introduce the numerical methods and the optimization scheme. In Sec. III, we discuss the optimal pulse shapes for ultrafast Rydberg state preparation and investigate the underlying dynamical processes. Finally, in Sec. IV we summarize our findings.

II. NUMERICAL METHODS

As a prototype atom for optimization simulations, we use lithium within the single active electron (SAE) approximation with the static potential $V_0(r)$ introduced in Ref. [22]. The optimization scheme is independent of the precise atomic model, and the scheme is readily applicable to other models of alkali-metal atoms. The laser-electron interaction is included in the dipole approximation, yielding the velocity gauge Hamiltonian (in Hartree atomic units [23])

$$\hat{H}(t) = \frac{\hat{\mathbf{p}}^2}{2} + V_0(\hat{\mathbf{r}}) + A_z(t)\hat{p}_z, \tag{1}$$

where we have restricted ourselves to linearly polarized laser fields, and the diamagnetic $\frac{A(t)^2}{2}$ term has been gauge transformed away.

Our goal is to transfer the maximum amount of population from the initial state, $2s$, (with zero azimuthal quantum number, $m = 0$) to a certain set $\mathcal{I}$ of Rydberg states $|\phi_{n,l}\rangle$ (preserving $m = 0$). This can be achieved by maximizing the target functional

$$G[\mathbf{u}] = \sum_{|\phi_{n,l}\rangle \in \mathcal{I}} |\langle \phi_{n,l} | \psi(T_{\max})\rangle|^2, \tag{2}$$

where $\mathbf{u}$ is the set of optimizable parameters and $|\psi(T_{\max})\rangle$ is the electron state at the end of the laser pulse.

The optimizable parameters $\mathbf{u}$ define the temporal shape of the laser vector potential $A_z[\mathbf{u}](t)$. Similarly to the approaches in Refs. [10,24], the pulse is constructed as a superposition of

*janne@solanpaa.fi
†esa.rasanen@tut.fi

multiple *channels*, each with a single central wavelength, i.e.,

$$A_z(t) = \sum_{i=1}^{N} \frac{A_i}{\omega_i} \mathrm{env}(t-\tau_i, \sigma_i) \cos\left[\omega_i (t-\tau_i) + \phi_i\right], \quad (3)$$

where A_i, ω_i, τ_i, ϕ_i, and σ_i are the amplitude, frequency, time of envelope maximum, carrier-envelope phase, and envelope full width at half maximum (FWHM) of each channel. The channel envelopes are given by

$$\mathrm{env}(t-\tau, \sigma) = \begin{cases} \exp\left[-\frac{\log(2)}{1-(\frac{t-\tau}{2\sigma})^2}\left(\frac{t-\tau}{\sigma}\right)^2\right], & |t-\tau| < 2\sigma \\ 0, & \text{otherwise} \end{cases}. \quad (4)$$

This is a modified Gaussian which goes to zero at twice the FWHM, and it is infinitely times differentiable everywhere. This pulse parametrization allows us to model realistic pulse shapes that can be generated with modern light field synthesizers [8].

Calculation of the target functional in Eq. (2) for each pulse shape requires us to (i) compute stationary states $|\phi_{n,l}\rangle$ of the system and (ii) propagate the initial state of the system under the laser vector potential. The stationary states are obtained by solving the effective radial equation for each angular quantum number l with first-order finite differences. Time propagation of the electron wave function is carried out with the QPROP software, version 2.0 [25] using the Crank-Nicolson scheme [26]. For simulation parameters, we have used the radial grid spacing 0.1 a.u. (0.005 nm), radial grid length 300 a.u. (16 nm), l quantum numbers up to 50, imaginary absorbing potential of width 50 a.u. (2.6 nm), and time step 0.02 a.u. (0.5 as) for the simulations. Convergence of a few selected results was checked with higher accuracy.

The QPROP software was modified and wrapped for use within PYTHON 3 [27] for interfacing with the optimization library NLOPT [28]. Optimization is performed with a two-step scheme: Global optimization is carried out with *multi-level single-linkage* (MLSL) algorithm [29], which essentially restarts local optimization while avoiding previously found local extrema [28], and for local optimization we use the derivative-free, trust-region-based algorithm called the *constrained optimization by linear approximations* (COBYLA) method [28,30]. This derivative-free optimization scheme does not require the computation of the gradient of Eq. (2).

The optimization routine is provided with one to six different channels with fixed central wavelengths 300 nm, 400 nm, 700.2243 nm, 800 nm, 1.6 μm, and 2 μm. The value close to 700 nm is in resonance with the $2s \rightarrow 2p$ transition. Furthermore, each channel is constrained to maximum electric field amplitude of $A_i \leqslant 67$ GV/m. The time of the envelope maximum is allowed to vary ± 6 fs, and the field FWHM of each channel can have values between 2.4 and 15 fs.

III. OPTIMIZATION RESULTS

A typical optimization process is shown in Fig. 1. It begins with a random initial pulse within the constrained search space, and local optimizer looks for a local maximum of the target functional. After a local maximum has been found, approximately at iteration number 102, the global optimization routine takes over and provides the local optimizer a new initial guess, causing a sharp drop in the target value. A typical optimization simulation runs approximately 100 to 200 optimization steps, providing up to a few local maxima. Optimization of the pulse parameters is indeed crucial for reaching reasonable target populations. In the example of Fig. 1, the optimization starts with a random pulse combination reaching barely 1% target population, but the optimization shapes the pulse to provide up to 5% target population (at iteration number 149).

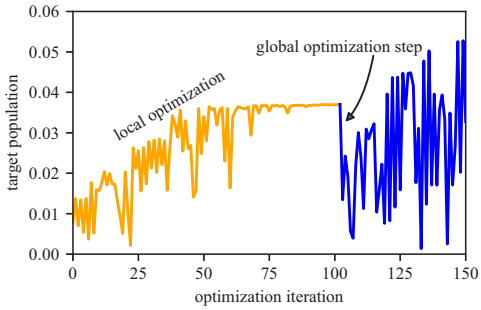

FIG. 1. Total population of the target states as a function of the optimization iterations demonstrating the working principle of the two-step optimization scheme. After convergence of the first local optimization [orange (gray) curve], the global optimizer restarts the local optimizer in a different region of the search space [at iteration number 102, blue (black) curve]. Here we have targeted the states $n = 7, l = 0 \ldots 2$.

The best results for each set of target states are collected in Table I. We only show the best one or two channel combinations for each target, but all possible channel combinations were tested. The optimized target populations range from 90% for the simplest target down to 3% for more difficult to reach target states such as $n = 7$, $l = 4 \ldots 6$. We have also investigated the excitation of the system to a single target state: For $7f$, we have reached up to 2.5% population and for $8i$ up to 1.7%. These moderate populations of single-target states suggest the scheme lacks the finesse to target single Rydberg states. However, due to finding only a few local extrema per target for each channel combination, it may

TABLE I. Summary of maximum achieved target populations for different pulse channel combinations.

Target	Channels (μm)	Max. population
$2p$	0.7	91%
$n = 7, l = 0 \ldots 2$	0.8, 0.7, 0.4, 0.3	14%
	0.8, 0.7, 0.4	5%
$n = 7, l = 4 \ldots 6$	2, 0.8, 0.7, 0.4	6%
	2, 0.8, 0.4	3%
$n = 7 \ldots 10, l = 4$	2, 0.7	6%
$n = 7 \ldots 10$	2, 0.8, 0.7, 0.3	23%
	2, 1.6, 0.8, 0.7, 0.3	21%

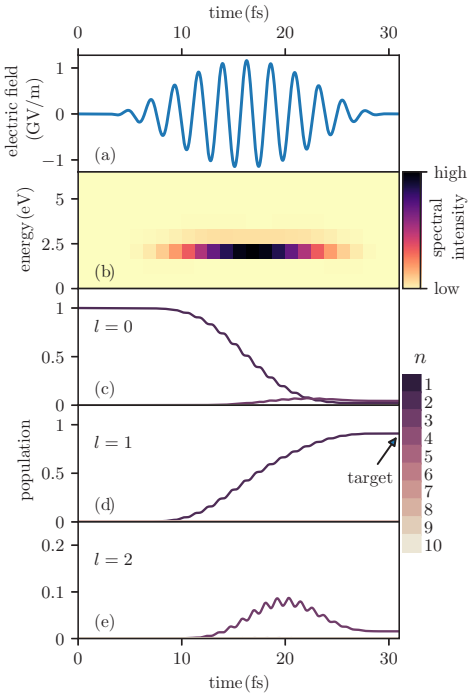

FIG. 2. (a) The optimized laser pulse for populating the $2p$ state, (b) the power spectral density of the laser electric field, and (c)–(e) the populations of the stationary states.

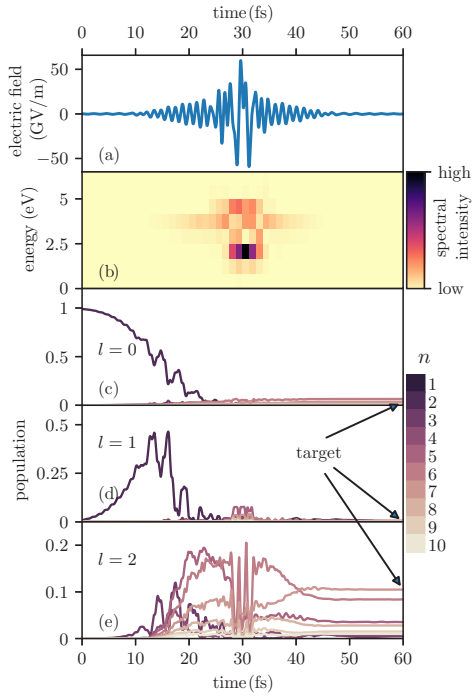

FIG. 3. (a) The optimized laser pulse for populating the set of states $n = 7$, $l = 0 \ldots 2$ using the channels 800, 700, 400, and 300 nm, (b) the power spectral density of the electric field, and (c)–(e) the populations of the stationary states.

be possible to improve these results with more optimization simulations and/or gradient-based algorithms.

The maximum populations in Table I are less than those achieved in previous works on optimal control of population transfer in atoms and molecules, e.g., in Refs. [31,32]. However, one must take into account the extremely constrained pulse combinations required by modern waveform synthesizers. In particular, the pulses with fixed channel wavelengths lack the ability to play with the resonances of the system. Moreover, the Gaussian envelope of each channel forbids any sudden changes in the temporal profiles of the pulses, and shortness of the resulting pulses forces the control scheme to consider multiple complex transitions between the states.

Next we will inspect the population transfer mechanisms behind the optimal pulses for a few select examples from Table I. The simplest transition to consider is $2s \to 2p$. This is forbidden for hydrogen, but for Li the transition is allowed. This transition also serves as the first step in the optical preparation of Rydberg states through a two-step excitation [4]. We find the optimal population transfer to be achieved with a pulse consisting only of the 700-nm channel—not surprising since the channel is in resonance with the transition. The pulse and the populations of the few lowest states are show in Fig. 2. The optimal pulse has a small peak electric field to avoid ionization, and a 90% population transfer is achieved with a pulse duration (intensity FWHM) less than 10 fs. Merely increasing the pulse duration would not improve the result since the initial state, $2s$, is already depleted with the current pulse shape. At first, the population transfer $2s \to 2p$ seems like a simple few-level process. Indeed, a two-level model with the states $2s$ and $2p$ under the laser pulse of Fig. 2 already yields an 80% population transfer. However, even a bound-state model with all states up to $n = 10$ fails to reach the 90% yield of the full model. This suggests either the involvement of very high Rydberg states or perhaps even the continuum in the full population transfer.

Let us turn our attention to ultrafast population of Rydberg states. Targeting the states $n = 7$, $l = 0 \ldots 2$, our scheme yields a solid 14% final population using the channels 800, 700, 400, and 300 nm (see Fig. 3). These channels are mixed with peak electric field ratios of $35 : 1 : 13 : 16$. While the 700-nm channel is relatively weak compared to others, it is of utmost importance and without it the final target population would drop to 0.2%. The optimized population transfer is somewhat akin to the traditional two-step excitation: First the

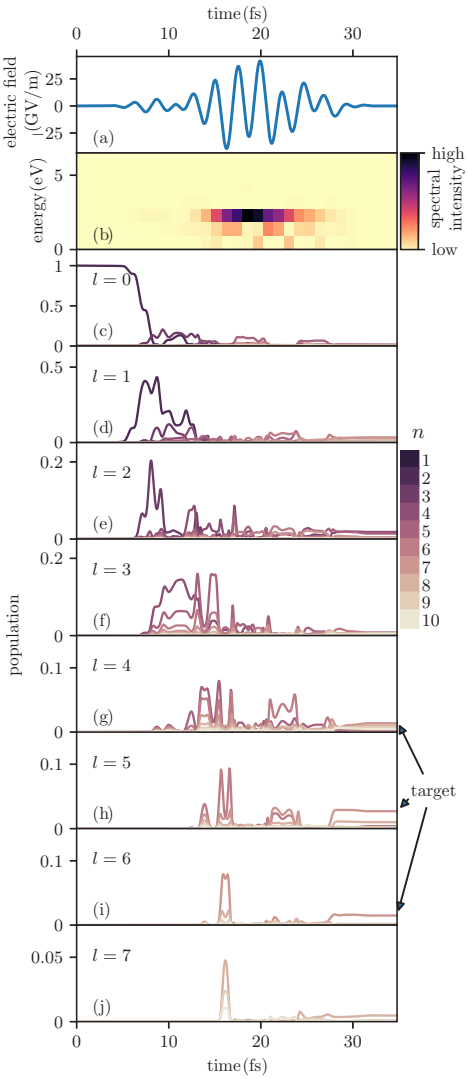

FIG. 4. (a) The optimized laser pulse for populating the set of states $n = 7$, $l = 4 \ldots 6$ using the channels 2 μm, 800 nm, 700 nm, and 400 nm, (b) the power spectral density of the electric field, and (c)–(j) the populations of the stationary states.

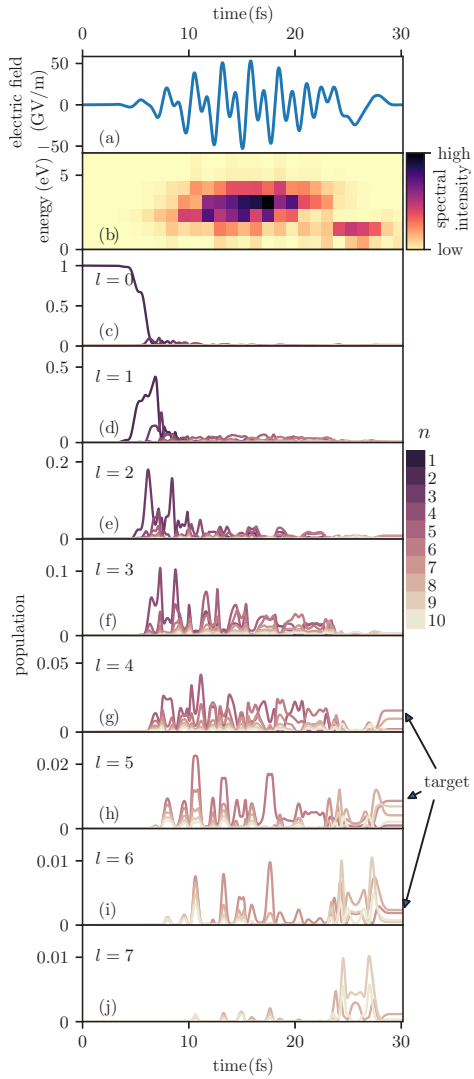

FIG. 5. Same as Fig. 4, but without the 700-nm channel.

electron is excited from $2s$ to $2p$ by the weak 700-nm component; however, the second step is a much more complicated process involving multiple transitions resulting in most of the final target population in the $7d$ state.

Next, we will focus our attention on a more complicated target, $n = 7$, $l = 4 \ldots 6$, which cannot be reached with two-photon absorption, in contrast with the previous example. An optimized pulse of duration less than 30 fs can transfer up to 6% of the electron population to the target states. The pulse, shown in Fig. 4(a), mixes the channels 2 μm, 800 nm, 700 nm, and 400 nm in ratios of electric field peak amplitude as 1 : 1.8 : 2.25 : 0.04. The 800- and 700-nm channels activate

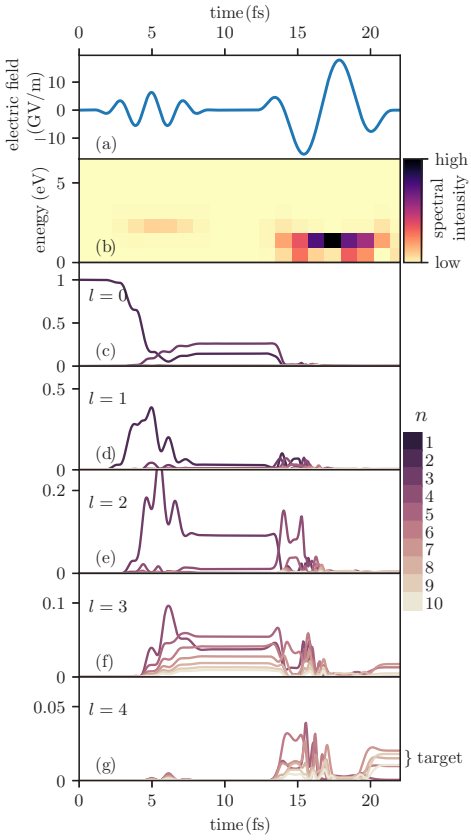

FIG. 6. (a) The optimized laser pulse for populating the set of $l = 4$ states with principal quantum numbers $n = 7 \ldots 10$ consists of first a few-cycle 700-nm primer followed by single-cycle 2-μm pulse, (b) the power spectral density of the electric field, and (c)–(g) the populations of the stationary states.

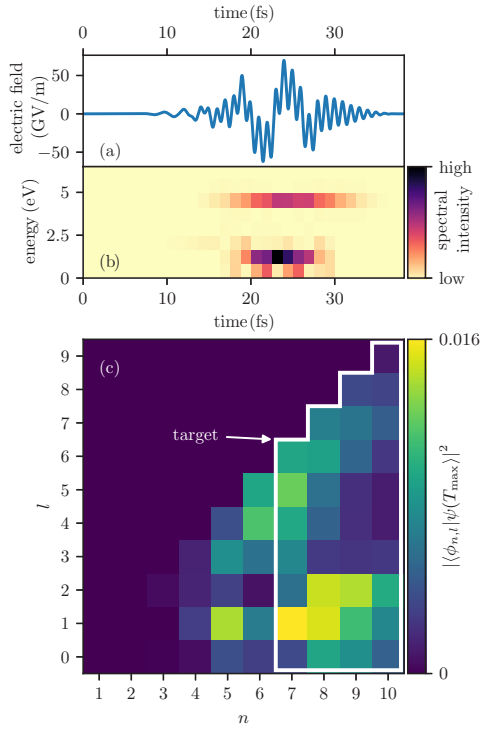

FIG. 7. (a) The optimized laser pulse for populating the set of states $n = 7 \ldots 10$ using the channels 2 μm, 800 nm, 700 nm, and 300 nm, (b) the power spectral density of the electric field, and (c) the final populations of the stationary states.

simultaneously, while the 2-μm channel activates 6 fs later than the previous ones. The channels overlap significantly in time, yielding a complicated process for the population transfer. The first few femtoseconds, up to approximately $t = 12$ fs, transfer the population from $2s$ to higher states with $l \approx 1 \ldots 3$, whereas the rest of the pulse makes the electron population oscillate between multiple states and partly ionize.

A question arises of whether the 700-nm pulse is an essential primer to achieve the initial $2s \rightarrow 2p$ excitation. This is not the case, as demonstrated in Fig. 5 where we optimize the same target as previously but *without* the 700-nm channel. A good initial population transfer to the $2p$ state can still be found; however, rest of the population transfer process is naturally different due to different pulse temporal shape.

We will now turn our attention to targeting the population of a single angular quantum number, e.g., $l = 4$ with $n = 7 \ldots 10$. The optimal pulse, shown in Fig. 6(a), is a sequence of 700-nm and 2-μm channels providing us final target population of 6%. To analyze the population transfer process via pairwise transfer rates, notice first that the state populations $|c_{n,l}|^2 = |\langle\phi_{n,l}|\psi(t)\rangle|^2$ are equivalent in the Schrödinger and interaction pictures of quantum mechanics. In the interaction picture, the expansion coefficients obey the system of ordinary differential equations [33]

$$\frac{d}{dt}c^I_{(n,l)}(t) = -iA_z(t)\sum_{(n',l')} W_{(n,l),(n',l')} \times \exp\{i[E_{(n',l')} - E_{(n,l)}]t\}c^I_{(n',l')}(t), \quad (5)$$

where $W_{(n,l),(n',l')}$ is the z component of the $(n,l),(n',l')$ momentum matrix element in the Schrödinger picture. Now, the pairwise transfer rates are given by

$$T_{(n,l),(n',l')}(t) = A_z(t)^2|W_{(n,l),(n',l')}|\langle\phi^S_{n,l}|\psi^S(t)\rangle|^2. \quad (6)$$

The transfer rates T for the optimized population transfer to $l = 4$, $n = 7 \ldots 10$ are shown as a function of time in the animation that can be found in Supplementary Material [34]. The first, 700-nm pulse excites the system from the initial $2s$ state to a set of $l = 3$ states ($n = 4 \ldots 10$) via $2p$. Some population is left in the $2p$ and $3d$ states. The second, 2-μm pulse first transfers population leftovers from the $2p$ state via $4d$ state to the f states, and after its first optical cycle, the second pulse transfers the population from the f states to the targeted g states. Because of weak pulses, the system is essentially not ionized, but the rest of the population escapes to higher bound states. Transfer rates seem the obvious choice for interpreting the optimal population transfer processes for each target, but they turn out to be significantly more complicated for most of the other targets.

As a final demonstration, we target the states with principal quantum numbers $n = 7 \ldots 10$ without restrictions to the angular quantum number. Because of the larger number of targeted states, the total target population reaches over 20% with the optimal pulses with the highest yield achieved with the channels 2 μm, 800 nm, 700 nm, and 400 nm, shown in Fig. 7. Most of the final target population is in low-l states, peaking at $7p$ and $8p$ followed by their neighbours by coupling, $8d$ and $9d$.

IV. SUMMARY

We have demonstrated the applicability of a few-color femtosecond pulses realizable by modern waveform synthesis [8] to optimal control of population transfer from ground state to a set of Rydberg states. Our control scheme was found to achieve up to 23% Rydberg-state populations when transferring population to a few selected states, but when targeting a single state these experimentally restricted pulse combinations do not seem to allow sufficient control over the excitation process.

Typical simulations with such realistic multicolor waveforms yield complicated dynamical processes which usually cannot be easily interpreted with clear few-step excitation paths. In this respect, our results also demonstrate a very different optimized dynamical process compared to having longer and less constrained pulses, which allows the exploitation of the resonances.

We expect that with refinements to the available pulse configurations and more powerful, gradient-based optimization algorithms one can further increase the total achieved target population. These enhancements could also allow us to target smaller sets of states while still retaining compatibility with experimentally feasible wave forms. In addition, further investigation would be warranted to study the applicability of our scheme to, e.g., the preparation of circular Rydberg states, including field polarization as an additional control knob, and to full multielectron models with possibly even more complicated optimization landscapes.

ACKNOWLEDGMENTS

The authors are grateful to Prof. Hossein Sadeghpour for insightful discussions and Mika Sarvilahti for the idea regarding the modified Gaussian function. This work was supported by the Academy of Finland (Grants No. 267686 and No. 304458). We also acknowledge CSC—the Finnish IT Center for Science—for computational resources.

[1] See, e.g., C. E. Theodosiou, Phys. Rev. A **30**, 2881 (1984).
[2] H. T. Wang, W. S. Felps, and S. P. McGlynn, J. Chem. Phys. **67**, 2614 (1977).
[3] A. Lagerqvist and E. Miescher, Can. J. Phys. **44**, 1525 (1966).
[4] T. F. Gallagher, *Rydberg Atoms* (Cambridge University Press, Cambridge, UK, 1994).
[5] M. Saffman, T. G. Walker, and K. Mølmer, Rev. Mod. Phys. **82**, 2313 (2010).
[6] P. J. J. Luukko and J.-M. Rost, Phys. Rev. Lett. **119**, 203001 (2017).
[7] T. A. Johnson, E. Urban, T. Henage, L. Isenhower, D. D. Yavuz, T. G. Walker, and M. Saffman, Phys. Rev. Lett. **100**, 113003 (2008).
[8] See, e.g., M. T. Hassan, A. Wirth, I. Grguraš, A. Moulet, T. T. Luu, J. Gagnon, V. Pervak, and E. Goulielmakis, Rev. Sci. Instrum. **83**, 111301 (2012), and references therein.
[9] R. E. Goetz, A. Karamatskou, R. Santra, and C. P. Koch, Phys. Rev. A **93**, 013413 (2016).
[10] J. Solanpää, M. F. Ciappina, and E. Räsänen, J. Mod. Opt. **64**, 1784 (2017).
[11] J. Solanpää, J. A. Budagosky, N. I. Shvetsov-Shilovski, A. Castro, A. Rubio, and E. Räsänen, Phys. Rev. A **90**, 053402 (2014).
[12] A. Castro, A. Rubio, and E. K. U. Gross, Eur. Phys. J. B **88**, 191 (2015).
[13] C. Jin and C. D. Lin, Chin. Phys. B **25**, 094213 (2016).
[14] G.-L. Wang, L.-H. Zhou, S.-F. Zhao, and X.-X. Zhou, Commun. Theor. Phys. **65**, 601 (2016).
[15] D. Peng, M. V. Frolov, L.-W. Pi, and A. F. Starace, Phys. Rev. A **97**, 053414 (2018).
[16] C. Winterfeldt, C. Spielmann, and G. Gerber, Rev. Mod. Phys. **80**, 117 (2008).
[17] (a) Y. Chou, P.-C. Li, T.-S. Ho, and S.-I. Chu, Phys. Rev. A **91**, 063408 (2015); (b) See, e.g., T. Hornung, R. Meier, D. Zeidler, K.-L. Kompa, D. Proch, and M. Motzkus, Appl. Phys. B **71**, 277 (2000), and references therein.
[18] S. Haessler *et al.*, Phys Rev. X **4**, 021028 (2014).
[19] R. Netz, T. Feurer, G. Roberts, and R. Sauerbrey, Phys. Rev. A **65**, 043406 (2002).
[20] B. Chatel, J. Degert, S. Stock, and B. Girard, Phys. Rev. A **68**, 041402 (2003).
[21] A. Präkelt, M. Wollenhaupt, C. Sarpe-Tudoran, and T. Baumert, Phys. Rev. A **70**, 063407 (2004).
[22] W. Schweizer, P. Faßbinder, and R. González-Férez, At. Data Nucl. Data Tables **72**, 33 (1999).
[23] D. R. Hartree, Math. Proc. Camb. Philos. Soc. **24**, 89 (1928).
[24] B. Bódi, E. Balogh, V. Tosa, E. Goulielmakis, K. Varjú, and P. Dombi, Opt. Express **24**, 21957 (2016).

[25] D. Bauer and P. Koval, Comput. Phys. Commun. **174**, 396 (2006).

[26] J. Crank and P. Nicolson, Math. Proc. Cambridge Philos. Soc. **43**, 50 (1947).

[27] Python Software Foundation, PYTHON language reference, version 3.6, https://www.python.org.

[28] S. G. Johnson, The NLOPT nonlinear-optimization package, https://nlopt.readthedocs.io.

[29] A. H. G. R. Kan and G. T. Timmer, Math. Prog. **39**, 27 (1987).

[30] M. J. D. Powell, A Direct Search Optimization Method That Models the Objective and Constraint Functions by Linear Interpolation, in *Advances in Optimization and Numerical Analysis*, edited by S. Gomez and J.-P. Hennart (Kluwer Academic, Dordrecht, 1994), pp. 51–67.

[31] W. Zhu, J. Botina, and H. Rabitz, J. Chem. Phys. **108**, 1953 (1998).

[32] M. Sugawara, Chem. Phys. Lett. **358**, 290 (2002).

[33] See, e.g., J. J. Sakurai and J. Napolitano, *Modern Quantum Mechanics*, 2nd ed. (Cambridge University Press, Cambridge, UK, 2017), or any other standard book on elementary quantum mechanics.

[34] See Supplemental Material at http://link.aps.org/supplemental/10.1103/PhysRevA.98.053422 for these videos visualize the transition rates, excited state populations, and the laser electric field of the electron dynamics in Figs. 3-7.

`Fiend` – Finite Element Quantum Dynamics

The following article has been re-typeset from

J. Solanpää, and E. Räsänen
`Fiend` – Finite Element Quantum Dynamics
arXiv:1812.05943

`Fiend` – Finite Element Quantum Dynamics

J. Solanpää,[1,*] and E. Räsänen[1]

[1]*Computational Physics Laboratory, Tampere University, Tampere FI-33101, Finland*

(Received XXX; Accepted XXX)

We present `Fiend` – a simulation package for three-dimensional single-particle time-dependent Schrödinger equation for cylindrically symmetric systems. `Fiend` has been designed for the simulation of electron dynamics under *inhomogeneous* vector potentials such as in nanostructures, but it can also be used to study, e.g., nonlinear light-matter interaction in atoms and linear molecules. The light-matter interaction can be included via the minimal coupling principle in its full rigour, beyond the conventional dipole approximation. The underlying spatial discretization is based on the FEM, and time-stepping is provided either via the generalized-α or Crank-Nicolson methods. The software is written in Python 3.6, and it utilizes state-of-the-art linear algebra and FEM backends for performance-critical tasks. `Fiend` comes along with an extensive API documentation, a user guide, simulation examples, and allows for easy installation via `Docker` or the Python Package Index. Keywords: Time-dependent

Schrödinger equation, finite element method, atoms, nanostructures, light-matter interaction, strong field physics

PROGRAM SUMMARY

Program Title: Fiend
Licensing provisions: MIT License
Programming language: Python 3.6
Computer: Tested on x86_64 architecture.
Operating system: Tested on Linux and macOS.
RAM: Simulation dependent: from megabytes to hundreds of gigabytes.
Parallelization: MPI-based parallelization. Thread-based parallelization via BLAS and LAPACK backends.
External routines/libraries:
PETSc, SLEPc, FEniCS, HDF5
petsc4py, slepc4py, mpi4py, h5py, numpy, scipy, matplotlib, psutil, mypy, progressbar2
Nature of problem:
Solution of time independent and time dependent single active electron Schrödinger equations in cylindrically symmetric systems including interactions with spatially inhomogeneous vector potentials.
Solution method:
Finite element discretization of the Schrödinger equation. Time evolution via the generalized-α or Crank-Nicolson methods.
Restrictions:
Cylindrically symmetric single active electron systems.
Unusual features:
Finite element discretization of the equations allowing *inhomogeneous spatial dependence of the vector potential* (e.g., plasmon-enhanced fields). Integration with the FEniCS finite element suite. Installable from the Python Package Index. Pre-installed Docker images available.
Additional comments:
The source code is also available at https://fiend.solanpaa.fi.
Python package available at https://pypi.org/project/fiend/.
Docker images are available at https://hub.docker.com/r/solanpaa/fiend/.
Running time:
From minutes to weeks, depending on the simulation.

1. Introduction

Simulation of three-dimensional (3D) single particle quantum mechanics (QM) is still one of the most used computational approaches in the strong field and attosecond communities. In these fields, the nonlinear interaction of the atomic or molecular electron with the driving laser field requires fast and accurate integration of the 3D time dependent Schrödinger equation (TDSE). Recent applications include, e.g., benchmarking of approximate models [1–6], study of high-order harmonic generation [7–9], and the study of photoionization [10–14].

Recently the strong-field and attosecond communities have turned their attention to related phenomena in nanostructures. There the nanostructure geometry and plasmonic effects cause the electromagnetic (EM) field to become extremely inhomogeneous [15] which, in turn, causes significant differences to the traditional ultrafast and strong-field phenomena in atoms and molecules. Recent studies include, e.g., nanostructure-enhanced photoionization of gases [16–18] and electron emission from nanostructures such as tips [19–28] and rods [29–33].

There are already multiple software designed for integrating the three-dimensional time-dependent Schrödinger equation (TDSE). Open-source software include, e.g., Qprop [34], Octopus [35, 36], QnDynCUDA [37], and WavePacket [38], but there are also plenty of other options such as SCID-TDSE [39], tRecX [40, 41], and ALTDSE [42]. Qprop, SCID-TDSE, and QnDynCUDA solve the TDSE using a grid-based representation of the radial coordinates and spherical harmonics for the angular dependence; TRecX and WavePacket support multiple basis sets; Octopus relies on a real-space grid; and ALTDSE requires end-user to provide the matrices in an appropriate eigenbasis.

However, efficient and accurate simulation of ultrafast and strong-field phenomena in nanostructures and nanostructure-enhanced gases requires specialized TDSE-solvers. Most importantly, since the laser electric field has strong spatial inhomogeneity, it is imperative to have position-dependent control of simulation accuracy. In addition, it would be beneficial to have the TDSE-solver directly interface with a solver for the EM problem.

To this end, we have developed `Fiend`, a QM simulator based on the FEM. `Fiend` provides solvers for the time independent and time-dependent single active electron Schrödinger equations in cylindrically symmetric systems[1] for solving time-independent and time-dependent Schrödinger equations in cylindrically symmetric systems. We have designed `Fiend` to integrate with the open source `FEniCS` finite element (FE) suite [43–49] allowing for easy description of complicated system geometries. Being FEM-based, `Fiend` also allows the use of potentials with integrable singularities.

`Fiend` is written in `Python 3.6`, but much of the heavy number-crunching is delegated to well-tested and efficient external libraries. The software is modular and easy to extend. We also provide a comprehensive unit- and integration-test suite to ensure reliability. Moreover, we provide straightforward installation methods either via the Python Package Index [50] or as Docker images [51].

This paper is organized as follows. In Sec. 6 we describe the FE discretization of the

[1] Although the restriction to cylindrically symmetric systems can be lifted relatively easily if needed.

Schrödinger equations and the time-propagation schemes. Section 6 focuses on the design and implementation of Fiend. Section 6 provides a few example simulation, and finally, in Sec. 6 we summarize this paper and possible extensions of the presented software suite.

2. Finite element quantum mechanics

2.1. Systems

Fiend is designed for simulating cylindrically symmetric single (active) electron systems interacting with time and (optionally) position dependent vector potentials. The Hamiltonian operator of these systems can be written as

$$\hat{H} = \hat{T_\rho} + \frac{\hat{p}_z^2}{2} + V(\hat{\rho}, \hat{z}) + W(\hat{\rho}, \hat{z}, \hat{p}_\rho, \hat{p}_z, t), \tag{6}$$

where $\hat{\rho}$ is the planar radial coordinate operator, $\hat{z}$ the z-coordinate operator, $\hat{T}_\rho$ the kinetic energy operator with respect to planar radial motion[2], $\hat{p}_z$ the z-component of the momentum operator, V the static potential, and W the light-matter interaction operator.

Fiend readily supports three types of interaction operators W. First, for linearly polarized vector potentials $\mathbf{A} = f(t)\mathbf{e}_z$ in the length gauge the interaction operator is given by

$$W_{\mathrm{LG}} = -\frac{\partial f(t)}{\partial t}\hat{z}, \tag{8}$$

secondly, in the velocity gauge the interaction operator reads

$$W_{\mathrm{VG}} = f(t)\hat{p}_z, \tag{9}$$

and finally for more general cylindrically symmetric inhomogeneous vector potentials $\mathbf{A} = \mathbf{A}_s(\rho, z)f(t)$ we provide the interaction operator

$$\begin{aligned} W_{\mathrm{inhomogeneous}} = &\frac{1}{2}f(t)\mathbf{A}_s \cdot \mathbf{p} + \frac{1}{2}f(t)\mathbf{p} \cdot \mathbf{A}_s \\ &+ \frac{1}{2}f(t)^2\|\mathbf{A}_s(\hat{\rho}, \hat{z})\|^2. \end{aligned} \tag{10}$$

Moreover, Fiend supports all interaction operators of the form $\hat{W} = W(\hat{\rho}, \hat{z}, \hat{p}_\rho, \hat{p}_z, t)$.

[2]Note that $\hat{T}_\rho$ is not proportional to the square of the planar radial momentum operator, i.e.,

$$\begin{aligned} \hat{T}_\rho &= -\frac{1}{2}\left(\frac{\partial^2}{\partial_\rho^2} + \frac{1}{2}\frac{\partial}{\partial_\rho}\right) \\ &\neq \frac{1}{2}\left[-\mathrm{i}\left(\frac{\partial}{\partial_\rho} + \frac{1}{2\rho}\right)\right]^2 = \frac{\hat{p}_\rho^2}{2}. \end{aligned} \tag{7}$$

This is a peculiarity of quantum mechanics in cylindrical coordinates [52].

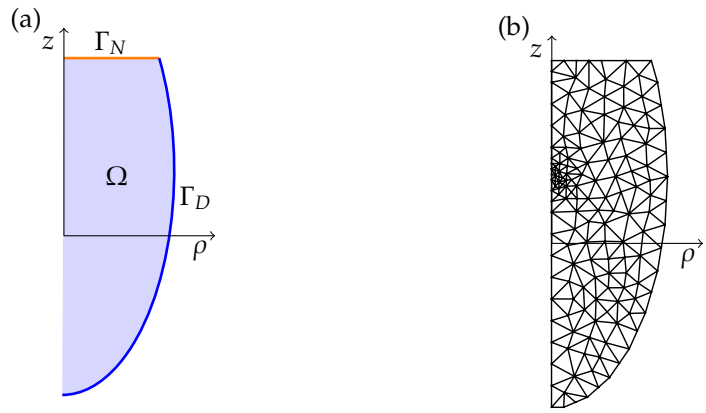

Figure 1: (a) Simulation domain Ω is a truncation of the full $\rho \geq 0$ half-plane. We can impose both Dirichlet and Neumann boundary conditions at will on different sections (Γ_D, Γ_N) of the domain boundary $\partial\Omega$. (b) Triangular mesh of the domain Ω supports arbitrary spatial refinement.

The above interaction operators conserve the magnetic quantum number m, and by default, we simulate only the $m = 0$ subspace. Correspondingly, the coordinate space domain is a two-dimensional slice of the cylindrical coordinates, $\Omega_\infty = \{\rho \geq 0, z \in \mathbb{R}\}$, which we truncate for numerical simulations to a *finite* domain Ω [see Fig. 1(a)].

2.2. Time independent Schrödinger equation

On the domain Ω_{TI} the time-independent Schrödinger equation (TISE) can be written as

$$-\frac{1}{2\rho}\frac{\partial}{\partial\rho}\left(\rho\frac{\partial\psi_k}{\partial\rho}\right) - \frac{1}{2}\frac{\partial^2\psi_k}{\partial z^2} + V(\rho, z)\psi_k = E_k\psi_k, \tag{11}$$

where E_k, ψ_k is the kth eigenpair. This equation is accompanied by continuity boundary condition at $\rho = 0$,

$$\lim_{\rho\to 0+}\left(\rho\frac{\partial\psi}{\partial\rho}\right) = 0. \tag{12}$$

Elsewhere on the boundary $\partial\Omega_{\text{TI}}$ we can choose freely between zero Neumann boundary conditions (ZNBCs) and zero Dirichlet boundary conditions (ZDBCs) – depending on the requirements of our model. For example, in Fig. 1(a) where we have imposed ZNBC on the upper boundary of the simulation domain, Γ_N, and ZDBC on the arc Γ_D.

To discretize TISE, we begin by looking for eigenpairs $E_k \in \mathbb{R}$, $\psi_k \in F$ of the weak form corresponding to Eq. (11) and the boundary conditions described above. The

weak form is given by

$$\begin{aligned} &-\frac{1}{2}\int_{\Omega_{\mathrm{TI}}} \sum_{\alpha=\rho,z} \frac{\partial\chi}{\partial\alpha}\frac{\partial\psi_k}{\partial\alpha}\rho\,\mathrm{d}\rho\,\mathrm{d}z \\ &+\int_{\Omega_{\mathrm{TI}}} \chi V(\rho,z)\psi_k\rho\,\mathrm{d}\rho\,\mathrm{d}z \\ &=E_k\int_{\Omega_{\mathrm{TI}}} \chi\psi_k\rho\,\mathrm{d}\rho\,\mathrm{d}z\ \forall\chi\in F, \end{aligned} \tag{13}$$

where $F = \left\{\psi \in H^1(\Omega_{\mathrm{TI}}) \,|\, \psi(\Gamma_D) = 0\right\}$ is the standard Sobolev space on Ω_{TI} of real-valued L^2-integrable functions with L^2 integrable first derivatives. Notice also that F includes ZDBCs, and the natural inner product is

$$\left\langle\chi\middle|\psi\right\rangle = \int_{\Omega_{\mathrm{TI}}} \chi(\rho,z)^*\psi(\rho,z)\,\rho\,\mathrm{d}\rho\,\mathrm{d}z. \tag{14}$$

Furthermore, we must restrict ourselves to a finite dimensional approximation of F. First, the simulation domain Ω_{TI} is described using an unstructured triangular mesh which supports arbitrary refinement [see, e.g., Fig. 1(b)]. Next, we construct a basis of continuous low-order Lagrange polynomials ϕ_i, each with compact support on the mesh elements. This basis spans a finite dimensional function space

$$F_h = \mathrm{span}\left\{\phi_i\right\}_{i=0}^{N-1} \subset F \tag{15}$$

where the TISE weak form [Eq. (13)] can be written as a finite dimensional generalized Hermitian eigenvalue equation

$$(\mathbf{T}+\mathbf{V})\psi_k = \mathbf{S}E_k\psi_k. \tag{16}$$

Here ψ_k is a vector of the real-valued expansion coefficients of the kth eigenstate, E_k the corresponding eigenvalue, and

$$S_{ij} = \left\langle\phi_i\middle|\phi_j\right\rangle, \tag{17}$$

$$T_{ij} = -\frac{1}{2}\sum_{\alpha=\rho,z}\left\langle\frac{\partial\phi_i}{\partial\alpha}\middle|\frac{\partial\phi_j}{\partial\alpha}\right\rangle, \text{ and} \tag{18}$$

$$V_{ij} = \left\langle\phi\middle|V(\rho,z)\phi_j\right\rangle \tag{19}$$

are the overlap, kinetic energy, and potential energy matrices, respectively. Note that since the static potential of the system is implemented only via Eq. (19) which involves integration, we can use any static potential for which Eq. (19) is finite, e.g., the Coulomb potential.

2.3. Time dependent Schrödinger equation

In a similar manner as with TISE, TDSE can be discretized as

$$\mathrm{i}\mathbf{S}\dot{\psi}(t) = (\mathbf{T} + \mathbf{V} + \mathbf{W})\,\psi(t), \tag{20}$$

where $\psi(t)$ is a vector of the *complex-valued* expansion coefficients $c_i(t)$ of the wave function $\psi(\rho, z, t) = \sum c_i(t)\phi_i(\rho, z)$. **S**, **T**, and **V** are constructed the same way as for TISE (except we add an imaginary absorbing potential to **V**), and the light-matter interaction matrix is given by

$$W_{ij} = \left\langle \phi_i \middle| W_s\left(\rho, z, \frac{\partial}{\partial\rho}, \frac{\partial}{\partial z}, t\right) \middle| \phi_j \right\rangle \tag{21}$$

The basis of the discrete function space for TDSE can, in general, be different from the one used for TISE. This is useful in practice since often the stationary states can be computed in a much smaller simulation domain than needed for an accurate description of the TDSE. We can change the function space by three methods: (1) using a larger simulation domain for the TDSE, (2) refining the mesh according to the requirements of the TDSE simulation, and (3) change the degree of our basis functions according to the required accuracy.

For evolving the discretized state, i.e., the expansion coefficients $\psi(t)$ according to Eq. (20), `Fiend` implements two approximations of the time evolution operator: the Crank-Nicolson (CN) method [53] and the generalized-α method [54].

The Crank-Nicolson (CN) method can be written as

$$\begin{aligned}\psi(t + \Delta t) = &\left[\mathbf{S} + \frac{\mathrm{i}\Delta t}{2}\mathbf{H}\left(t + \frac{\Delta t}{2}\right)\right]^{-1} \\ &\left[\mathbf{S} - \frac{\mathrm{i}\Delta t}{2}\mathbf{H}\left(t + \frac{\Delta t}{2}\right)\right]\psi(t) + O(\Delta t^2),\end{aligned} \tag{22}$$

and it is a unitary time-reversible transformation [53] as long as the matrix inversion is performed to a sufficient accuracy.

The generalized-α method was originally developed for integrating the equations of motion arising from fluid dynamics [54], but we have successfully applied it to the TDSE integration. To the best of our knowledge, the α-method has not been proven to be unitary nor is it exactly time-reversible. Nevertheless, we have achieved accuracies comparable to the CN method – and in the case of extremely inhomogeneous vector potentials, the generalized-α method seems to be significantly more stable than CN.

2.4. Incorporation of boundary conditions

The continuity boundary condition at $\rho = 0$ and ZNBCs are automatically included by dropping the boundary integrals when deriving Eqs. (13) and (18). However, the ZDBCs must be included in the system matrices via the following modifications: the rows and columns of **S**, **T**, **V**, and **W** corresponding to the degrees of freedom (DOFs) on the boundary Γ_D with ZDBCs set to zero. Only for **S** we must set the corresponding

diagonal elements to one to ensure invertibility. Note that it's crucial to zero out not only the rows but also the corresponding columns of the matrices to retain hermiticity.

Embedding ZNBCs via the vanishing boundary terms when deriving Eqs. (13) and (18) causes a practical issue: Some operators such as $\hat{p}_z = -\mathrm{i}\partial_z$, $\hat{p}_\rho = -\mathrm{i}\left(\partial_\rho + \frac{1}{2\rho}\right)$, and $\mathbf{A}\cdot\mathbf{p} + \mathbf{p}\cdot\mathbf{A}$ become *non-Hermitian*. Minor adjustments at the boundaries can remedy this, namely,

$$\hat{p}_\rho \to -\mathrm{i}\left[\partial_\rho + \frac{1}{2\rho} - \frac{1}{2}\delta(\mathbf{r}-\Gamma_N)n_\rho(\mathbf{r})\right], \tag{23}$$

$$\hat{p}_z \to -\mathrm{i}\left[\partial_z - \frac{1}{2}\delta(\mathbf{r}-\Gamma_N)n_z(\mathbf{r})\right], \text{ and} \tag{24}$$

$$\frac{1}{2}(\mathbf{A}\cdot\mathbf{p}+\mathbf{p}\cdot\mathbf{A}) \to \frac{1}{2}(\mathbf{A}\cdot\mathbf{p}+\mathbf{p}\cdot\mathbf{A}) - \frac{\mathrm{i}}{2}\mathbf{A}\cdot\mathbf{n}(\mathbf{r})\delta(\mathbf{r}-\Gamma_N), \tag{25}$$

where $\mathbf{n}(\mathbf{r}) = [n_\rho(\mathbf{r}), n_z(\mathbf{r})]^T$ is the outwards facing unit normal on the simulation domain boundary at point $\mathbf{r}$. This trick has been previously used to obtain the correct Hermitian operators in hyperspherical coordinates [52].

Another aspect to consider is the weak enforcement of ZNBCs compared to ZDBCs. If there was significant electron density on the Neumann boundary Γ_N, it will start to oscillate and eventually violate the ZNBC. This can be remedied when operating with matrix inverses as in the second step of the CN-propagator. We can add an extra error term, e.g., of the form

$$\gamma \sum_i \left| \int_{\Gamma_N} \chi_i^*(\rho,z)\nabla\psi(\rho,z,t)\cdot\mathrm{d}\mathbf{S} \right|^2, \gamma \in \mathbb{R} \tag{26}$$

to the error estimator in our numerical implementation. This will remove – or at least lessen – the issue arising from the weak enforcement of ZNBCs.

3. Implementation

3.1. Overview

We have implemented FE discretization of TISE and TDSE in the Python software package `Fiend` following the recipes of Sec. 6. `Fiend` is written in Python 3.6 and it utilizes reliable libraries commonly pre-installed in high-performance clusters and supercomputers. For sparse linear algebra we use the Portable, Extensible Toolkit for Scientific Computation (`PETSc`) [55–57] and the Scalable Library for Eigenvalue Problem Computations (`SLEPc`) [58, 59]. Meshing and other standard FEM-related parts are built on top of the components of the FEniCS project [43–49], and filesystem IO is largely based on `HDF5` [60] via `h5py` [61, 62]. In postprocessing and visualization we use also `numpy` [63], `scipy` [64], and `matplotlib` [65]. `Fiend` is parallelized using `MPI` via `mpi4py` [66–68].

The `PETSc`-dependency is slightly complicated as `PETSc` needs to be compiled either with real number support (x)or with complex number support. `Fiend`, on the other

hand, needs real numbers for TISE and post-processing but complex numbers for propagation. Consequently, the user must install *both* the real and complex versions of `PETSc/SLEPc` stacks and switch between these for different simulation steps. This factitious requirement for two different installations of `PETSc` can be revisited in the future upon the completion of `DOLFIN-X` [69] and `FFC-X` [70] including the merge of complex number support in `FEniCS` [71],

To ease installation, we provide a Docker [51] container with `Fiend` and all its dependencies preinstalled, see https://hub.docker.com/r/solanpaa/fiend/ for more details. In the same spirit, `Fiend` is also available in the Python Package Index [50] and can be installed with `pip` [72].

3.2. Library usage and numerical methods

A typical usage of the `Fiend` suite is demonstrated in Fig. 2. First we solve the TISE to obtain a set of stationary states. This includes meshing the domain for the time independent simulation and assembling the system matrices (17)–(19) with appropriate boundary conditions (see Sec. 6).

The TISE eigenproblem, Eq. (16), is solved (by default) with Rayleigh Quotient Conjugate Gradient (RQCG) method combined with classical Gram-Schmidt orthogonalization of the Krylov subspace basis with adaptive iterative refinement for increased numerical stability. RQCG is a variational method which essentially minimizes the Rayleigh quotient

$$\frac{\psi_k^\dagger \mathbf{H}_0 \psi_k}{\psi_k^\dagger \mathbf{S} \psi_k} \tag{27}$$

of a desired number of orthonormal vectors with respect to the bilinear product induced by $\mathbf{S}$ [59]. Upon convergence, this corresponds to k smallest real eigenpairs of TISE.

Step 2 (see Fig. 2) is to prepare the discrete description of the TDSE. This includes meshing the domain for the time dependent problem, interpolating stationary states to the new mesh, and also assembly of the system matrices (17)–(19) and the time-independent part(s) of Eq. (21).

The propagation in Step. 3 (Fig. 2) requires the user to load the environment with complex number `PETSc`. The time-dependent Hamiltonian is constructed from the matrices computed in the previous step, and the discrete TDSE (20) is solved with `PETSc`'s propagators. We also provide code templates for easy implementation of new propagators.

Finally, we provide a set of example scripts for postprocessing. These scripts include, e.g., visualization of the integrated electron density in time and temporal shape of the laser field, but there are also scripts to compute more complex observables such as the high-harmonic and photoelectron spectra.

All the numerical methods in `Fiend` depend on efficient sparse linear algebra operations implemented in `PETSc`. By default, matrix inversions and the solution of linear equations are carried out with Generalized Minimal RESidual method (GMRES) [73], where the convergence criterion is computed with respect to the norm induced by the inner product in Eq. (14). Unfortunately, the `PETSc` linear algebra

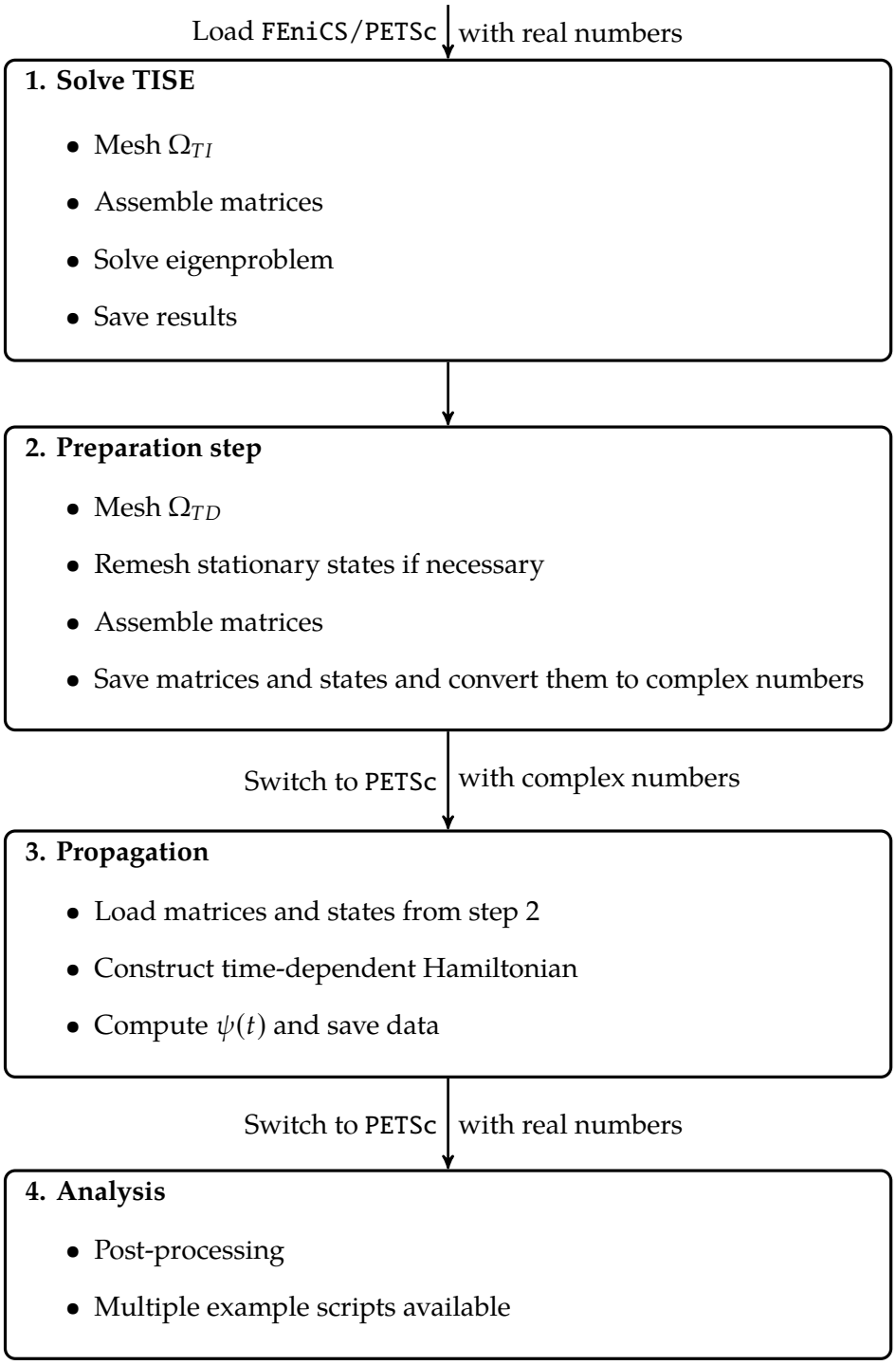

Figure 2: Typical simulation structure with `Fiend` together with the required changes to the runtime environment between the steps.

backend does not allow us to build the basis of the Krylov subspace with respect to a custom inner product. However, we have found the basis built with the standard Hermitian inner product to be sufficient performance-wise. Direct solvers such as `SuperLU_DIST` [74–76] and `MUMPS` [77, 78] are supported only with matrices that can be explicitly constructed without too high cost.

3.3. Note on meshing

We provide a way to generate meshes with arbitrary refinement in the coordinate space. The user should supply a function returning the maximum allowed cell circumradius[3] at coordinate $\mathbf{r}$, and the mesh can be refined until all cells of the mesh have circumradius below the desired one.

By default, the maximum cell circumradius is given by [79]

$$\begin{aligned}\max \mathrm{CR}(\mathbf{r}) = \mathrm{CR}_{\mathrm{asymp}} \Bigg[1 - \left(1 - \frac{\mathrm{CR}_{\mathrm{ref}}}{\mathrm{CR}_{\mathrm{asymp}}}\right) \\ \times \frac{R_{\mathrm{ref}}}{r} \tanh\left(\frac{r}{R_{\mathrm{ref}}}\right) \exp\left(-\frac{r^2}{R_{\mathrm{trans}}^2}\right)\Bigg] .\end{aligned} \tag{28}$$

For $r < R_{\mathrm{ref}}$ the cell circumradii are below $\mathrm{CR}_{\mathrm{ref}}$, and as $r \to R_{\mathrm{trans}}$, the maximum cell circumradius increases monotonically to $\mathrm{CR}_{\mathrm{asymp}}$.

4. Examples and test cases

4.1. Field-free propagation

To assess the stability and accuracy of the numerical methods implemented in `Fiend`, we compute a field-free propagation of an electron prepared in a superposition of Hydrogen 1s and 2s states,

$$\psi(t = 0) = \frac{1}{\sqrt{2}} \left(\psi_{1s} + \psi_{2s}\right) . \tag{29}$$

This state is propagated up to 100 a.u. of time. The simulation domain up to $R = 30$ a.u. is meshed using the default refinement introduced in Sec. 6 with $R_{\mathrm{ref}} = 4$ a.u., $R_{\mathrm{ref}} = 10$ a.u., $\mathrm{CR}_{\mathrm{ref}} = 0.01$ a.u. and $\mathrm{CR}_{\mathrm{asymp}} = 0.5$ a.u. We assess the accuracy of the numerical solution by comparing the simulated state to the exact result:

$$\left|1 - |\left\langle \psi_{\mathrm{exact}} \middle| \psi_{\texttt{Fiend}} \right\rangle|^2\right| . \tag{30}$$

The stability is investigated by evaluating how much the norm of the state differs from unity, i.e.,

$$\left|1 - \|\psi_{\texttt{Fiend}}\|^2\right| . \tag{31}$$

Both the α-propagator and the CN propagator reach an accuracy of 0.00524 % for the overlap with the time-step 0.05 a.u., and the norm of the simulated state deviates from unity only by $3.22 \cdot 10^{-5}$ %. This demonstrates the applicability of the propagators for the simulation of FE-discretized TDSE in cylindrical coordinates.

[3] Radius of the smallest circle enclosing the given triangular cell.

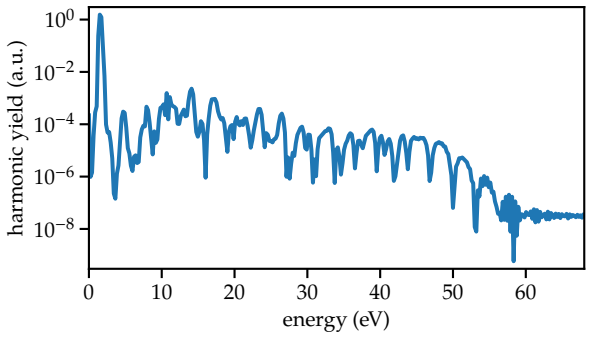

Figure 3: High-order harmonic spectrum of a hydrogen atom under a few-cycle femtosecond laser pulse.

4.2. High-harmonic generation

Next we demonstrate the applicability of `Fiend` to simulate high-order harmonic generation (HHG). According to the three-step model [80, 81], an atomic electron is excited to continuum and driven to oscillate around the atom [82]. Upon recombination with the parent ion, the excess energy is released as high-energy photons.

Full 3D simulation of HHG via TDSE is a difficult task due to the long extent of the electron wave function when driven by a short laser pulse. In order to obtain a decent description of the single-atom response for HHG, a large simulation domain is needed. We setup a simulation domain of radius 800 a.u. with a more refined mesh at the origin and gradually sparser mesh for larger radii.

The intensity spectrum of the single-atom response is proportional to the square of the Fourier transform of the dipole acceleration [83],

$$S(\omega) \propto \left| \left\langle \ddot{D}_z \right\rangle (\omega) \right|^2 , \tag{32}$$

where we compute the dipole acceleration via Ehrenfest's theorem [84], i.e.,

$$\left\langle \ddot{D}_z \right\rangle (t) = \left\langle \psi(t) \middle| -\frac{\partial V}{\partial z} \middle| \psi(t) \right\rangle . \tag{33}$$

In Fig. 3 we show the computed high-order harmonic spectrum computed for a hydrogen atom under a laser pulse with carrier frequency corresponding to 800 nm, intensity full width at half maximum 4.8 fs, and electric field peak intensity 36 GV/m. The spectrum is a typical HHG spectrum from a femtosecond laser pulse, and it ends at the cut-off energy ~ 2 a.u. in a decent agreement with the three-step model's cutoff ~ 1.7 a.u. [80, 81].

4.3. Metal nanotips and inhomogeneous fields

Metal nanotips have recently attracted attention due to their ability to enhance the laser electric field at the tip apex via plasmonic effects (see, e.g., [19–28]). `Fiend` is

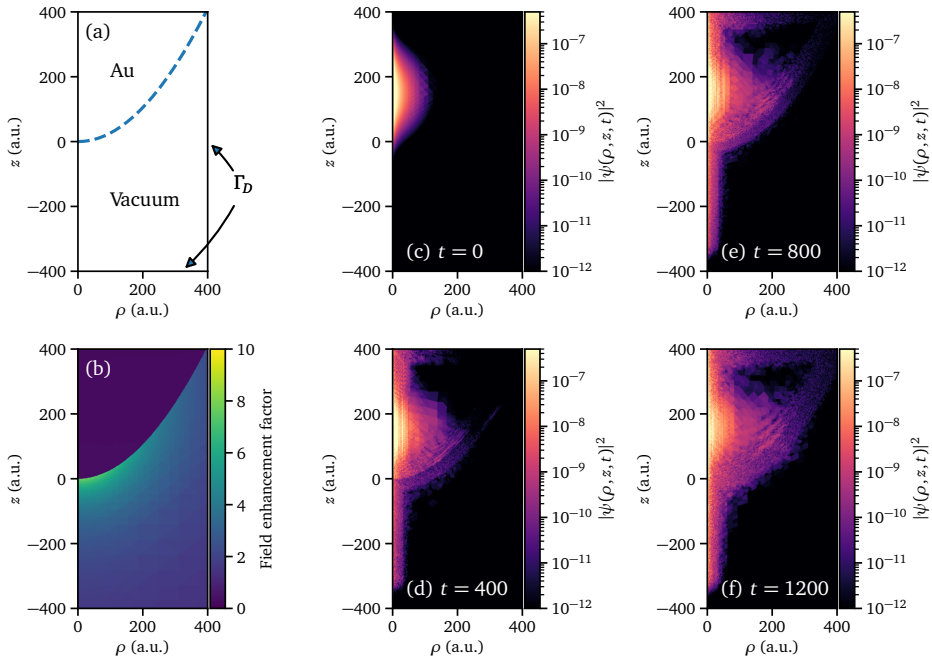

Figure 4: (a) Setup of the nanotip geometry where we have a sharp boundary between the gold nanotip and vacuum. (b) Computed spatial enhancement profile of the electric near field in a quasistatic approximation. (c)-(f) Snapshots of the electron density during time evolution.

capable of computing single-electron dynamics of these metal nanotapers including correctly the interaction with the *inhomogeneous* plasmon enhanced laser field.

The first step is to compute the plasmon enhanced near field. Here we consider a gold nanotip with apex radius 7 nm and full opening angle of 20 ° as demonstrated in Fig. 4(a). For typical laser wavelengths, such as 800 nm used here, a quasistatic description of the laser vector potential is applicable, i.e.,

$$\mathbf{A}(\mathbf{r}, t) = \mathbf{A}_s(\mathbf{r}) f(t), \tag{34}$$

where the spatial form $\mathbf{A}_s$ is the same as for the electric field

$$\mathbf{A}_s(\mathbf{r}) = \mathbf{E}(\mathbf{r}) = -\nabla U(\mathbf{r}). \tag{35}$$

The electrostatic potential $U(\mathbf{r})$ can be computed from the Poisson equation

$$-\nabla \cdot [\epsilon(\mathbf{r}) \nabla U(\mathbf{r})] = 0, \tag{36}$$

where $\epsilon(\mathbf{r})$ is the dielectric function of the material at position $\mathbf{r}$. Inside the gold nanotip the complex dielectric function (at 800 nm) is $\epsilon_{\mathrm{Au}} = -24.061 + 1.5068\,\mathrm{i}$ [85, 86] and at vacuum $\epsilon_{\mathrm{vac}} = 1$.

We can describe Eq. (38) using cylindrical coordinates. The interface condition

$$\epsilon_{\mathrm{Au}} \nabla u|_{\mathbf{r}\to\Gamma_{\text{tip-vac}}} - \epsilon_{\mathrm{vac}} \nabla u|_{\mathbf{r}\to\Gamma_{\text{vac-tip}}} = 0 \tag{37}$$

gives rise to the weak form

$$\begin{aligned} &\epsilon_{\mathrm{vac}} \int_{\text{vacuum}} \nabla v^*(\mathbf{r}) \cdot \nabla u(\mathbf{r})\, \rho \,\mathrm{d}\rho \,\mathrm{d}z \\ &+ \epsilon_{\mathrm{Au}} \int_{\text{tip}} \nabla v^*(\mathbf{r}) \cdot \nabla u(\mathbf{r})\, \rho \,\mathrm{d}\rho \,\mathrm{d}z = 0 \;\forall v \in \hat{U} \end{aligned} \tag{38}$$

with the test function space

$$\begin{aligned} \hat{U} = \big\{ v : \Omega \to \mathbb{C} \mid \mathrm{Re}(v),\, \mathrm{Im}(v) \in H^1(\Omega) : \\ v(\Gamma_D) = 0 \big\} \end{aligned} \tag{39}$$

and the trial function space

$$\begin{aligned} U = \big\{ u : \Omega \to \mathbb{C} \mid \mathrm{Re}(u),\, \mathrm{Im}(u) \in H^1(\Omega) : \\ u(\mathbf{r} \in \Gamma_D) = z \big\}. \end{aligned} \tag{40}$$

The simulation domain is a rectangular area, and the ZDBCs described above are imposed on the external boundaries denoted by Γ_D. Note that Fig. 4(a) demonstrates the domain and boundaries for the quantum simulation – for Poisson equation we employ a much larger simulation domain. The equation (38) can be solved easily with the `FEniCS` FEM-suite and we provide an example script at `demos/nanotip/1_near_field.py`

The computed spatial distribution of the field, $\|A_s(x, y, z)\|$, is demonstrated in Fig. 4(b). The field is at its maximum at the nanotip apex and decays rapidly with the distance to the tip. We note that this quasistatic solution provides field-enhancement factor of $f \approx 10$ which is comparable with experimental results [87].

In TDSE, we use a potential well for the static potential,

$$U(\mathbf{r}) = \begin{cases} 0, & \text{vacuum} \\ -\Phi, & \text{inside the tip,} \end{cases} \tag{41}$$

where $\Phi = 5.31$ eV is the work function of Au (111)-surface [88].

We prepare the electron as a Gaussian wave packet [Fig. 4(c)] and assemble the system matrices – *including the inhomogeneous field* – with `demos/nanotip/3_prepare_tdse.py`. The preparation step is slightly more complex than for linearly polarized vector potentials, but the provided example script should work as a template for further expansions.

We use a 800 nm pulse with 15 fs full width at half maximum for the Gaussian envelope. The maximum electric field amplitude without nanostructure enhancement is set to 30 GV/nm. Snapshots of the electron density during propagation are shown in Figs. 4(c)-(f). As expected, the electron emission is concentrated at the tip apex where the field enhancement is at its highest. Only a small percentage (~2 %) of the electron density is absorbed at the simulation box boundary.

5. Summary

We have presented `Fiend` – a versatile solver for single-particle quantum dynamics in cylindrically symmetric systems. This Python package provides an easy path for the study of nonlinear strong-field phenomena in atoms and nanostructures under both homogeneous and *inhomogeneous* vector potentials. Moreover, the FE discretization used by `Fiend` can adapt to complicated system geometries. The package is parallelized using `MPI`, and much of the high-performance computing is delegated to state-of-the-art numerical libraries. `Fiend` is modular and easy to extend, and we provide comprehensive documentation for the program code.

We have demonstrated the capabilities of `Fiend` by simulating two different scenarios. The simulation of high-order harmonic generation from a laser-driven hydrogen atom shows that `Fiend` can be applied to traditional strong-field phenomena in atoms. Furthermore, a simulation of the photoionization of a gold nanotip demonstrates `Fiend`'s suitability for studying plasmon-enriched strong-field phenomena in nanostructures.

6. Acknowledgements

We are grateful to Matti Molkkari and Joonas Keski-Rahkonen for insightful discussions. This work was supported by the Alfred Kordelin foundation and the Academy of Finland (grant no. 304458). We also acknowledge CSC – the Finnish IT Center for Science – for computational resources.

[1] N. Suárez, A. Chacón, J. A. Pérez-Hernández, J. Biegert, M. Lewenstein, and M. F. Ciappina, *High-order-harmonic generation in atomic and molecular systems*, Phys. Rev. A **95**, 033415 (2017).

[2] N. I. Shvetsov-Shilovski et al., *Semiclassical two-step model for strong-field ionization*, Phys. Rev. A **94**, 013415 (2016).

[3] A. Galstyan et al., *Reformulation of the strong-field approximation for light-matter interactions*, Phys. Rev. A **93**, 023422 (2016).

[4] M. Klaiber, J. Daněk, E. Yakaboylu, K. Z. Hatsagortsyan, and C. H. Keitel, *Strong-field ionization via a high-order Coulomb-corrected strong-field approximation*, Phys. Rev. A **95**, 023403 (2017).

[5] A.-T. Le, H. Wei, C. Jin, and C. D. Lin, *Strong-field approximation and its extension for high-order harmonic generation with mid-infrared lasers*, J. Phys. B **49**, 053001 (2016).

[6] S. Majorosi, M. G. Benedict, and A. Czirják, *Improved one-dimensional model potentials for strong-field simulations*, Phys. Rev. A **98**, 023401 (2018).

[7] L. Wang, G.-L. Wang, Z.-H. Jiao, S.-F. Zhao, and X.-X. Zhou, *High-order harmonic generation of Li + with combined infrared and extreme ultraviolet fields*, Chin. Phys. B **27**, 073205 (2018).

[8] Z. Abdelrahman et al., *Chirp-control of resonant high-order harmonic generation in indium ablation plumes driven by intense few-cycle laser pulses*, Opt. Express **26**, 15745 (2018).

[9] A.-T. Le, H. Wei, C. Jin, V. N. Tuoc, T. Morishita, and C. D. Lin, *Universality of Returning Electron Wave Packet in High-Order Harmonic Generation with Midinfrared Laser Pulses*, Phys. Rev. Lett. **113**, 033001 (2014).

[10] C. Hofmann et al., *Interpreting electron-momentum distributions and nonadiabaticity in strong-field ionization*, Phys. Rev. A **90**, 043406 (2014).

[11] V. P. Majety, A. Zielinski, and A. Scrinzi, *Mixed gauge in strong laser-matter interaction*, J. Phys. B **48**, 025601 (2015).

[12] A. M. Sayler et al., *Accurate determination of absolute carrier-envelope phase dependence using photo-ionization*, Opt. Lett. **40**, 3137 (2015).

[13] X. Y. Lai, W. Quan, S. G. Yu, Y. Y. Huang, and X. J. Liu, *Suppression in high-order above-threshold ionization: destructive interference from quantum orbits*, J. Phys. B **51**, 104003 (2018).

[14] D. Zille, D. Adolph, M. Möller, A. M. Sayler, and G. G. Paulus, *Chirp and carrier-envelope-phase effects in the multiphoton regime: measurements and analytical modeling of strong-field ionization of sodium*, New J. Phys. **20**, 063018 (2018).

[15] J. A. Schuller, E. S. Barnard, W. Cai, Y. C. Jun, J. S. White, and M. L. Brongersma, *Plasmonics for extreme light concentration and manipulation*, Nat. Mater. **9**, 193 (2010).

[16] L. Ortmann et al., *Emergence of a Higher Energy Structure in Strong Field Ionization with Inhomogeneous Electric Fields*, Phys. Rev. Lett. **119**, 053204 (2017).

[17] L. Ortmann and A. S. Landsman, *Analysis of the higher-energy structure in strong-field ionization with inhomogeneous electric fields*, Phys. Rev. A **97**, 023420 (2018).

[18] M. F. Ciappina et al., *Emergence of a Higher Energy Structure in Strong Field Ionization with Inhomogeneous Laser Fields*, in High-Brightness Sources and Light-driven Interactions (2018).

[19] B. Piglosiewicz et al., *Carrier-envelope phase effects on the strong-field photoemission of electrons from metallic nanostructures*, Nat. Photonics **8**, 37 (2013).

[20] M. Kruger, M. Schenk, M. Forster, and P. Hommelhoff, *Attosecond physics in photoemission from a metal nanotip*, J. Phys. B **45**, 074006 (2012).

[21] L. Wimmer, G. Herink, D. R. Solli, S. V. Yalunin, K. E. Echternkamp, and C. Ropers, *Terahertz control of nanotip photoemission*, Nat. Phys. **10**, 43 (2014).

[22] R. Bormann, S. Strauch, S. Schäfer, and C. Ropers, *An ultrafast electron microscope gun driven by two-photon photoemission from a nanotip cathode*, J. Appl. Phys. **118**, 173105 (2015).

[23] G. M. Caruso, F. Houdellier, P. Abeilhou, and A. Arbouet, *Development of an ultrafast electron source based on a cold-field emission gun for ultrafast coherent TEM*, Appl. Phys. Lett. **111**, 023101 (2017).

[24] B. Barwick, C. Corder, J. Strohaber, N. Chandler-Smith, C. Uiterwaal, and H. Batelaan, *Laser-induced ultrafast electron emission from a field emission tip*, New J. Phys. **9**, 142 (2007).

[25] G. Herink, D. R. Solli, M. Gulde, and C. Ropers, *Field-driven photoemission from nanostructures quenches the quiver motion*, Nature **483**, 190 (2012).

[26] R. Bormann, M. Gulde, A. Weismann, S. V. Yalunin, and C. Ropers, *Tip-Enhanced Strong-Field Photoemission*, Phys. Rev. Lett. **105**, 147601 (2010).

[27] B. Förg et al., *Attosecond nanoscale near-field sampling*, Nat. Commun. **7**, 11717 (2016).

[28] S. V. Yalunin et al., *Field localization and rescattering in tip-enhanced photoemission*, Ann. Phys. **525**, L12.

[29] R. G. Hobbs et al., *High-density Au nanorod optical field-emitter arrays*, Nanotechnology **25**, 465304 (2014).

[30] F. Kusa, K. E. Echternkamp, G. Herink, C. Ropers, and S. Ashihara, *Optical field emission from resonant gold nanorods driven by femtosecond mid-infrared pulses*, AIP Adv. **5**, 077138 (2015).

[31] A. Grubisic et al., *Plasmonic Near-Electric Field Enhancement Effects in Ultrafast Photoelectron Emission: Correlated Spatial and Laser Polarization Microscopy Studies of Individual Ag Nanocubes*, Nano Lett. **12**, 4823 (2012).

[32] R. G. Hobbs et al., *High-Yield, Ultrafast, Surface Plasmon-Enhanced, Au Nanorod Optical Field Electron Emitter Arrays*, ACS Nano **8**, 11474 (2014).

[33] A. Grubisic, V. Schweikhard, T. A. Baker, and D. J. Nesbitt, *Coherent Multiphoton Photoelectron Emission from Single Au Nanorods: The Critical Role of Plasmonic Electric Near-Field Enhancement*, ACS Nano **7**, 87 (2013).

[34] D. Bauer and P. Koval, *Qprop: A Schrödinger-solver for intense laser–atom interaction*, Comput. Phys. Commun. **174**, 396 (2006).

[35] M. A. Marques, A. Castro, G. F. Bertsch, and A. Rubio, *octopus: a first-principles tool for excited electron–ion dynamics*, Comput. Phys. Commun. **151**, 60 (2003).

[36] A. Castro et al., *octopus: a tool for the application of time-dependent density functional theory*, Phys. Stat. Sol. (b) **243**, 2465 (2006).

[37] C. Ó. Broin and L. Nikolopoulos, *A GPGPU based program to solve the TDSE in intense laser fields through the finite difference approach*, Comput. Phys. Commun. **185**, 1791 (2014).

[38] B. Schmidt and U. Lorenz, *WavePacket: A Matlab package for numerical quantum dynamics. I: Closed quantum systems and discrete variable representations*, Comput. Phys. Commun. **213**, 223 (2017).

[39] S. Patchkovskii and H. Muller, *Simple, accurate, and efficient implementation of 1-electron atomic time-dependent Schrödinger equation in spherical coordinates*, Comput. Phys. Commun. **199**, 153 (2016).

[40] A. Scrinzi, *Infinite-range exterior complex scaling as a perfect absorber in time-dependent problems*, Phys. Rev. A **81**, 053845 (2010).

[41] L. Tao and A. Scrinzi, *Photo-electron momentum spectra from minimal volumes: the time-dependent surface flux method*, New J. Phys. **14**, 013021 (2012).

[42] X. Guan, C. J. Noble, O. Zatsarinny, K. Bartschat, and B. I. Schneider, *ALTDSE: An Arnoldi–Lanczos program to solve the time-dependent Schrödinger equation*, Comput. Phys. Commun. **180**, 2401 (2009).

[43] *The FEniCS Project Version 1.5*, Archive of Numerical Software **3** (2015).

[44] A. Logg, K.-A. Mardal, and G. Wells, eds., *Automated Solution of Differential Equations by the Finite Element Method: The FEniCS Book*, Vol. 84, Lecture Notes in Computational Science and Engineering (Springer-Verlag Berlin Heidelberg, 2012).

[45] A. Logg and G. N. Wells, *DOLFIN: Automated Finite Element Computing*, ACM Transactions on Mathematical Software **37**, 20 (2010).

[46] R. C. Kirby and A. Logg, *A Compiler for Variational Forms*, ACM Transactions on Mathematical Software **32**, 417 (2006).

[47] K. B. Ølgaard and G. N. Wells, *DOLFIN: Automated Finite Element Computing*, ACM Transactions on Mathematical Software **37**, 8 (2010).

[48] *Unified Form Language: A domain-specific language for weak formulations of partial differential equations*, ACM Transactions on Mathematical Software **40**, 9 (2014).

[49] R. C. Kirby, *Algorithm 839: FIAT, a New Paradigm for Computing Finite Element Basis Functions*, ACM Transactions on Mathematical Software **30**, 502 (2004).

[50] J. Solanpää, *Fiend in PyPI*, (2018) https://pypi.org/project/fiend (visited on 11/19/2018).

[51] Docker Inc., *Enterprise Container Platform*, (2018) https://www.docker.com (visited on 11/19/2018).

[52] G. Paz, *On the connection between the radial momentum operator and the Hamiltonian in n dimensions*, European Journal of Physics **22**, 337 (2001).

[53] J. Crank and P. Nicolson, *A practical method for numerical evaluation of solutions of partial differential equations of the heat-conduction type*, Adv. Comput. Math. **6**, 207 (1996).

[54] K. E. Jansen, C. H. Whiting, and G. M. Hulbert, *A generalized-α method for integrating the filtered Navier–Stokes equations with a stabilized finite element method*, Computer Methods in Applied Mechanics and Engineering **190**, 305 (2000).

[55] S. Balay et al., *PETSc Users Manual*, tech. rep. ANL-95/11 - Revision 3.9 (Argonne National Laboratory, 2018).

[56] S. Balay, W. D. Gropp, L. C. McInnes, and B. F. Smith, *Efficient Management of Parallelism in Object Oriented Numerical Software Libraries*, in Modern Software Tools in Scientific Computing, edited by E. Arge, A. M. Bruaset, and H. P. Langtangen (1997), pp. 163–202.

[57] L. D. Dalcin, R. R. Paz, P. A. Kler, and A. Cosimo, *Parallel distributed computing using Python*, Advances in Water Resources **34**, New Computational Methods and Software Tools, 1124 (2011).

[58] V. Hernandez, J. E. Roman, and V. Vidal, *SLEPc: A Scalable and Flexible Toolkit for the Solution of Eigenvalue Problems*, ACM Trans. Math. Software **31**, 351 (2005).

[59] J. E. Roman, C. Campos, E. Romero, and A. Tomas, *SLEPc Users Manual*, tech. rep. DSIC-II/24/02 - Revision 3.9 (D. Sistemes Informàtics i Computació, Universitat Politècnica de València, 2018).

[60] The HDF Group, *Hierarchical Data Format, version 5*, (2018) http://www.hdfgroup.org/HDF5/.

[61] *HDF5 for Python*, http://www.h5py.org (visited on 11/19/2018).

[62] A. Collette, *Python and HDF5* (O'Reilly, 2013).

[63] T. E. Oliphant, *A guide to NumPy*, 2nd ed. (CreateSpace Independent Publishing Platform, 2015).

[64] E. Jones, T. Oliphant, P. Peterson, et al., *SciPy: Open source scientific tools for Python*, (2001) http://www.scipy.org/ (visited on 11/19/2018).

[65] J. D. Hunter, *Matplotlib: A 2D Graphics Environment*, Computing in Science & Engineering **9**, 90 (2007).

[66] L. Dalcin, P. Kler, R. Paz, and A. Cosimo, *Parallel Distributed Computing using `Python`*, Advances in Water Resources **34**, 1124 (2011).

[67] *`MPI` for `Python`: performance improvements and `MPI-2` extensions*, Journal of Parallel and Distributed Computing **68**, 655 (2008).

[68] *`MPI` for `Python`*, Journal of Parallel and Distributed Computing **65**, 1108 (2005).

[69] *FeniCS/`dolfinx`: Next generation FEniCS problem solving environment*, (2018) `https://github.com/FEniCS/dolfinx` (visited on 11/19/2018).

[70] *FeniCS/`ffcx`: Next generation FEniCS Form Compuler*, (2018) `https://github.com/FEniCS/ffcx` (visited on 11/19/2018).

[71] I. Baratta, *Complex Number support in FEniCS*, (2018) `https://gist.github.com/IgorBaratta/c7ca5252834f2c70efe0d233a3acecb4` (visited on 11/19/2018).

[72] Python Software Foundation, *Installing `Python` Modules*, (2018) `https://docs.python.org/3/installing/` (visited on 11/19/2018).

[73] Y. Saad and M. H. Schultz, *GMRES: A Generalized Minimal Residual Algorithm for Solving Nonsymmetric Linear Systems*, SIAM Journal on Scientific and Statistical Computing **7**, 856 (1983).

[74] X. S. Li, *An Overview of `SuperLU`: Algorithms, Implementation, and User Interface*, TOMS **31**, 302 (2005).

[75] X. Li, J. Demmel, J. Gilbert, iL. Grigori, M. Shao, and I. Yamazaki, *`SuperLU` Users' Guide*, tech. rep. LBNL-44289 (Lawrence Berkeley National Laboratory, 1999).

[76] X. S. Li and J. W. Demmel, *`SuperLU_DIST`: A Scalable Distributed-Memory Sparse Direct Solver for Unsymmetric Linear Systems*, ACM Trans. Mathematical Software **29**, 110 (2003).

[77] P. R. Amestoy, I. S. Duff, J. Koster, and J.-Y. L'Excellent, *A Fully Asynchronous Multifrontal Solver Using Distributed Dynamic Scheduling*, SIAM Journal on Matrix Analysis and Applications **23**, 15 (2001).

[78] P. R. Amestoy, A. Guermouche, J.-Y. L'Excellent, and S. Pralet, *Hybrid scheduling for the parallel solution of linear systems*, Parallel Computing **32**, 136 (2006).

[79] F. Gygi and G. Galli, *Real-space adaptive-coordinate electronic-structure calculations*, Phys. Rev. B **52**, R2229 (1995).

[80] J. L. Krause, K. J. Schafer, and K. C. Kulander, *High-order harmonic generation from atoms and ions in the high intensity regime*, Phys. Rev. Lett. **68**, 3535 (1992).

[81] M. Lewenstein, P. Balcou, M. Y. Ivanov, A. L'Huillier, and P. B. Corkum, *Theory of high-harmonic generation by low-frequency laser fields*, Phys. Rev. A **49**, 2117 (1994).

[82] M. Lewenstein and A. L'Huillier, *Principles of Single Atom Physics: High-Order Harmonic Generation, Above-Threshold Ionization and Non-Sequential Ionization*, in *Strong Field Laser Physics*, edited by T. Brabec (Springer, New York, USA, 2008), pp. 147–184.

[83] J. A. Pérez-Hernández and L. Plaja, *Comment on 'On the dipole, velocity and acceleration forms in high-order harmonic generation from a single atom or molecule'*, J. Phys. B **45**, 028001 (2012).

[84] A. Gordon and F. X. Kärtner, *The Ehrenfest Theorem and Quantitative Predictions of HHG based on the Three-step Model*, in *Ultrafast Optics V*, edited by S. Watanabe and K. Midorikawa (Springer New York, New York, 2007), pp. 183–186.

[85] *Optical constants of the noble metals*, Phys. Rev. B **6**, 4370 (1972).

[86] M. N. Polyanskiy, *Refractive index database*, 2018-11-19, https://refractiveindex.info.

[87] C. Ropers, D. R. Solli, C. P. Schulz, C. Lienau, and T. Elsaesser, *Localized Multiphoton Emission of Femtosecond Electron Pulses from Metal Nanotips*, Phys. Rev. Lett. **98**, 043907 (2007).

[88] H. B. Michaelson, *The work function of the elements and its periodicity*, J. Appl. Phys. **48**, 4729 (1977).